



저작자표시-비영리-변경금지 2.0 대한민국

이용자는 아래의 조건을 따르는 경우에 한하여 자유롭게

- 이 저작물을 복제, 배포, 전송, 전시, 공연 및 방송할 수 있습니다.

다음과 같은 조건을 따라야 합니다:



저작자표시. 귀하는 원저작자를 표시하여야 합니다.



비영리. 귀하는 이 저작물을 영리 목적으로 이용할 수 없습니다.



변경금지. 귀하는 이 저작물을 개작, 변형 또는 가공할 수 없습니다.

- 귀하는, 이 저작물의 재이용이나 배포의 경우, 이 저작물에 적용된 이용허락조건을 명확하게 나타내어야 합니다.
- 저작권자로부터 별도의 허가를 받으면 이러한 조건들은 적용되지 않습니다.

저작권법에 따른 이용자의 권리는 위의 내용에 의하여 영향을 받지 않습니다.

이것은 [이용허락규약\(Legal Code\)](#)을 이해하기 쉽게 요약한 것입니다.

[Disclaimer](#)

공학박사 학위논문

열전 기반 상변화 열공압 소프트 액츄에이터 연구

The thermoelectric based phase-transition soft
thermo-pneumatic actuator

2022년 8월

서울대학교 대학원

기계항공공학부

윤 여 상

열전 기반 상변화 열공압 소프트 액추에이터 연구

The thermoelectric based phase-transition soft
thermo-pneumatic actuator

지도교수 고 승 환

이 논문을 공학박사 학위논문으로 제출함
2022년 4월

서울대학교 대학원
기계항공공학부
윤 여 상

윤여상의 공학박사 학위논문을 인준함
2022년 6월

위 원 장 _____ 송 한 호 (인)

부위원장 _____ 고 승 환 (인)

위 원 _____ 한 경 원 (인)

위 원 _____ 홍 석 준 (인)

위 원 _____ 이 하 범 (인)

Abstract

Soft pneumatic actuators play an important role in the technological advancement of soft robotics, but they face intrinsic limitations due to the presence of complex and bulky peripherals, such as air compressors and tubes, that make it difficult to design completely soft robotic systems. Therefore, it is of essence to simplify soft robot control systems without bulky auxiliary peripherals that interfere with the robotic operation and its proper design. In this study, we develop a soft thermo-pneumatic actuating module (STPAM) that operates based on the thermally controlled gas-liquid phase transition with the soft thermoelectric (TE) device. The bi-directional thermal managing ability (heating and cooling) of the TE device is capable of controlling the inflation and deflation of the pneumatic chamber with the aid of the thermally conductive silicone rubber that enhances the heat transfer. Moreover, we employ phase-changing (liquid-solid) material to facilitate fast and certain deflation by preventing heat backflow. We demonstrated the active cooling of the thermoelectric device that accelerates the deflation rate by the active cooling functionality that significantly reduces the whole operating time. Additionally, to validate its practical usage in soft robotics, the soft actuating module shows different motions, such as bending and rectilinear stretching, based on the assembly design that is employed to develop the soft gripper and the entirely untethered soft earthworm robot without a complicated and bulky compressor system. Furthermore, the underwater application, Flatfishbot, which is untethered controlled and mimics the marine vertebrates' underwater gliding locomotion was developed. The STPAM successfully modulated buoyant force to control the Flatfishbot's posture and reconstruct the gliding and rotational locomotion. Furthermore, the Flatfishbot successfully conducted practical tasks such as inspecting the underwater environment through the camera or delivering cargo.

Keyword : thermo-electric, soft actuator, phase transition, soft electronics, active cooling

Student Number : 2016-20697

Table of Contents

Chapter 1. Introduction	8
1.1. Study Background	8
1.2. Research Purpose	1 2
Chapter 2. Soft thermo-pneumatic actuating module	1 3
2.1. Overview	1 3
2.1. Soft thermo-electric device.....	1 6
2.2. PCM heatsink	2 3
2.2. Double-sided Soft Thermo-pneumatic Actuating Module	2 8
2.4. Assembly of the STPAMs	3 1
2.5. Method	3 8
Chapter 3. Soft fish-bot (underwater application)	4 3
3.1. Background & Introduction.....	4 3
3.2. Underwater Soft Thermo-pneumatic Actuating Module.....	4 8
3.3. Flatfishbot.....	5 6
3.4. Method.....	7 4
Chapter 4. Conclusion	7 7
Bibliography	7 9

List of Figures

Figure 1 Environmental adaptability of soft robots a) different dynamic model of hard and soft robots b) photograph showing environmental adaptability of soft robot	8
Figure 2 Soft pneumatic actuators a) Mechanism of soft pneumatic actuators b) complicated, bulky, and necessary peripherals of conventional pneumatic power source	9
Figure 3 Previous phase changing actuators and its mechanism.....	9
Figure 4 A schematic for the mechanism of thermoelectric devices..	10
Figure 5 A schematic and photographs of soft TE devices.....	11
Figure 6 Research purpose. a) soft thermo-pneumatic actuating module b) Enhanced cooling response of the actuating module c) Diverse soft robotic applications	12
Figure 7 Structure of the Soft thermo-pneumatic actuating module ..	13
Figure 8 A schematic of the comprehensive mechanism of the soft thermo-pneumatic actuating module	14
Figure 9 Thermal images and photographs during heating (inflation) and cooling (deflation).....	15
Figure 10 Schematics for assemblies of STPAMs	15
Figure 11 Thermally conductive elastomer a) Schematic of thermal percolation network of BN micro powder b) Thermal conductivity of BN microplate/PDMS composite.....	16
Figure 12 Thermal managing performance of BN/PDMS composite a) Temperature change depending on time b) Thermal image	17
Figure 13 A schematic represents isotropic thermal management of joule heater and anisotropic thermal management of the thermoelectric device.	17
Figure 14 Heating performance of TE device compared with Joule heater. Each experiment was heated with powers of 0.5W, 1W, and 1.6W. The temperature was measured with an IR camera.....	19
Figure 15 Inflating a thermo-pneumatic chamber by TE heating and joule heating	19
Figure 16 Chamber width of TE device with different powers.	20
Figure 17 Comparison of the pneumatic chamber deflation performance between natural cooling and thermoelectric cooling. a) Width of thermo-pneumatic chamber during the deflating. b) Photographs of the pneumatic chambers during deflation by thermoelectric cooling and natural cooling.	21
Figure 18 Chamber width of TE device with different volumes of the active liquid during a) heating and b) cooling process. (The current magnitude: 2A (heating), 1.5A (cooling)).....	22
Figure 19 A schematic describing the heat dissipation of the TE device without heatsink, with commercial heatsink, and PCM heatsink during cooling.	23
Figure 20 PCM heatsink a) A schematic of the mechanism of the PCM heatsink. b) SEM images of (i) the pristine copper foam and (ii) the PCM filled copper foam and (iii) a photograph of the soft TE device	

attaching PCM heatsink.	2 4
Figure 21 a) Schematic for the experimental setup to compare the heating ability of the soft TE device depending on an applied heatsink setting. The temperature of a) the top and b) bottom sides was measured by IR thermal camera in the heating mode.	2 5
Figure 22 Characterization of the PCM heatsink a) Temperature change of the cooling surface of the soft TE device. b) Temperature of the heat dissipating(heating) surface of the soft TE device. c) Repetitive temperature changes of a TE device with heatsink.	2 6
Figure 23 Enhanced chamber deflating response by attaching the PCM heatsink. a) Comparison of the deflating performance of the STPAM without heatsink and with PCM heatsink. b) Chamber width of TE device during cooling mode with different heatsink, as attachment of the heatsink, paraffin, table, and commercial heatsink.	2 7
Figure 24 Characterization of the double-sided STPAM. a) A schematic of the single-sided STPAM and the double-sided STPAM. b-c) Profile of the chamber width of the single-sided STPAM and the double-sided STPAM during (b) Inflating and (c) deflating.	2 8
Figure 25 Force characterization a) A schematic of the measurement setting b) The measurement of the inflating force of the double-sided STPAM. c) The measurement of the inflating force of the double-sided STPAM during repetitive operating. d) Time required for the double-sided STPAM to generate the force of 5 N according to repetition. .	2 9
Figure 26 the B-mode assembly of STPAMs under various loads a) Photographs of the B-mode assembly of STPAMs (i) at the OFF state and inflated under the load of (ii) 0g, (iii) 50g, (iv) 100g, (v) 200g. b) Bending angle profile of the B-mode assembly of STPAMs inflated under the various loads.	3 1
Figure 27 Thermal images of B-mode assembly of STPAMs at heated and cooled state.	3 2
Figure 28 Comparison of the TE cooling and the natural cooling during the deflation of the B-mode assembly of STPAMs.	3 2
Figure 29 A soft gripper based on B-mode STPAM assemblies gripping an egg and an apple.	3 3
Figure 30 The R-mode STPAMs assembly a) Photographs and thermal images of the operation of the R-mode assembly of the STPAMs. b) Length profile of the R-mode assembly of the STPAMs during the heating and cooling process.	3 4
Figure 31 A schematic for the bio-inspired untethered soft robot based on the R-mode assembly of STPAMs.	3 4
Figure 32 A flowchart of bio-inspired untethered soft robot based on R-mode STPAM assembly.	3 5
Figure 33 Operation of the bio-inspired untethered soft robot a) (i) The collected temperature and humidity data by the soft robot and (ii) the traveled distance of the soft robot during demonstrating autonomous stop and go depending on environmental temperature. In (ii), Lines colored red and blue on the background indicate cooling and heating	

modes, respectively. (E) Snapshots of the moving, autonomously stopped, and re-operated soft robot.	3 5
Figure 34 A schematic for detail fabrication process of the soft TE device	3 8
Figure 35 The Design of the top and bottom electrode and substrate. (Unit: mm)	3 8
Figure 36 A schematic of the pneumatic chamber structure.....	3 9
Figure 37 Schematic of a bending part of B-mode STPAM assembly	4 0
Figure 38 Algorithm diagram for the autonomous operation process of the bio-inspired untethered soft robot based on R-mode STPAM assembly.....	4 2
Figure 39 Gliding locomotion from nature	4 3
Figure 40 Classification of swimming modes of biomimetic underwater robots ⁴³	4 4
Figure 41 A schematic for soft Flatfishbot controlled by wireless module and thermally inflatable localized buoyancy control units	4 5
Figure 42 The air bladder of teleost fishes	4 6
Figure 43 Schematic for an uSTPAM that acts like air bladders of fish	4 6
Figure 44 Photographs of the reversible deflation and inflation of thermoelectric pneumatic actuator by liquid-vapor phase transition.	4 7
Figure 45 Internal structure of the soft TPA unit that is comprised of a soft substrate, copper interconnecting film, thermoelectric legs, and elastic chamber.....	4 8
Figure 46 Transient photographs and thermal imaging snapshots of the single TPA unit as it inflates and deflated by switching from the heating to cooling mode due to phase transition.	4 9
Figure 47 Relationship between electrical current input into thermoelectric device and response time it takes to reach the neutral buoyancy.	5 0
Figure 48 Examining the difference between thermoelectric active cooling and natural convection to induce phase change from vapor to liquid and thus return to the original deflated state.	5 1
Figure 49 Comparison between thermoelectric and Joule heating performance by applying the identical amount of electrical power. The inset figures describe the heat transfer direction during thermoelectric and Joule heating modes. The large discrepancy of the performances originates from the isotropic heat flow of the Joule heater in which an enormous amount of heat is dissipated into the underwater reservoir.	5 2
Figure 50 Thermoelectric cooling performance difference between operating in the air and underwater. The cooling difference arises from the thermal conductivity of air and water, in which water functions as an effective heatsink to absorb heat energy from the opposite heating side of the thermoelectric device whereas air cannot be due to its thermal properties. The inset figure demonstrates the thermoelectric cooling performance at the same thermal condition for the extended	

time period	5 3
Figure 51 Response rate to reach the neutral buoyancy and start floating at different surrounding water temperatures. Please note that fluids inside the chamber have different boiling temperatures to enhance response time.....	5 4
Figure 52 Relationship between depth underwater and response time of uSTPAM.	5 5
Figure 53 Graphical illustration of Flatfishbot integrated with its functional components.....	5 6
Figure 54 Free-body diagram of the forward ascending, forward gliding and turning modes of the Flatfishbot. a) Forward ascending. b) Forward gliding. c) Making a (left) turn.	5 7
Figure 55 Design consideration. a) Designing of the soft robotic fish architecture by comparing numerically computed lift/drag ratio in a function of angle of attack b) Design optimization by examining lift/drag values with varying a/b ratio. c) Actual photograph of olive flounder. The photograph of olive flounder was obtained and reproduced under permission of Irina K.	5 9
Figure 56 Wireless flowchart of Flatfishbot by which the command inputs to the uSTPAM units of the robotic fish are delivered, and physical spatial data of the robotic fish from pressure and gyro-sensors is transmitted	6 0
Figure 57 Flatfishbot. a) Photographs of Assembled/disassembled Flatfishbot. b) Top view of Flatfishbot integrated with its functional components	6 1
Figure 58 Snapshots of the moving path that Flatfishbot went through to simulate the forward gliding locomotion of the marine vertebrates and corresponding pressure, gyro data during the locomotion.	6 2
Figure 59 Flatfishbot demonstration of changing direction to make a turn (top- and side-view) and corresponding sensor data.....	6 4
Figure 60 Vertically rising locomotion of Flatfishbot. (a) Snapshots of Flatfishbot moving up by turning all uSTPAM units. (b) Transient pitch and (b) water pressure values as the soft robotic fish moves up to the water surface	6 5
Figure 61 Flatfishbot is capable of picking up and delivering a cargo as a submersible miniaturized cargo ship.	6 6
Figure 62 Photographed moving route of the water-proof camera-attached Flatfishbot and corresponding recorded video snapshots during the locomotion to examine its potential to operate as an underwater inspection robot. The experimental setup and recording direction of the water-proof camera.....	6 7
Figure 63 Modified free-body diagram of Flatfishbot	6 8
Figure 64 Free-body diagram for moment calculation of Flatfishbot in the coordinate based on the external flow	6 8
Figure 65 Flatfishbot's 3D rendered image	7 0
Figure 66 Flatfishbot's calculated lift and drag coefficient depending on the angle of attack	7 0
Figure 67 Numerically calculated perpendicular distances of the lift force	

and the drag force	7 1
Figure 68 Comparison between the experimental data and the simulated data of the ascending gliding locomotion of the Flatfishbot. a) x-y 2D trajectory b) posture angle c) angular velocity d) angle of attack..	7 3
Figure 69 Schematic representation of the device fabrication process. Note that thermoelectric pellets in the fabrication process as shown above are connected in series within the device and thus operate as a whole.	7 4
Figure 70 Experimental setup to measure buoyant force and temperature. a) Inflation of uSTPAM causes the water level to rise, and the water level difference corresponds to the buoyant force. b) An experimental setup of active thermoelectric cooling in contact with water and suspended in the air.	7 5
Figure 71 Board circuit design and the corresponding soldered printed circuit board that consists of functional components for locomotion performance. We used two separate battery modules for constant heating and cooling modes: 7.4 V 2500 mAh LiPo battery for the heating mode (and powering microcontroller via the 3.3 V regulator) and a couple of 1.2 V 2000 mAh NiMH batteries connected in series for the cooling mode.....	7 6

Chapter 1. Introduction

1.1. Study Background

Soft Pneumatic Actuators

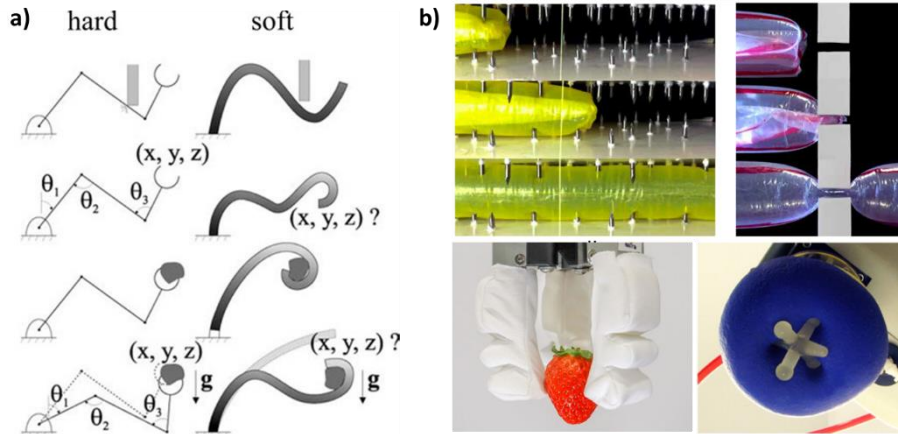


Figure 1 | Environmental adaptability of soft robots a) different dynamic model of hard and soft robots b) photograph showing environmental adaptability of soft robot

Soft robotics is an emerging technology that is predicted to replace conventional robotics in diverse fields, including surgical applications,¹ rehabilitation applications,²⁻⁵ crop harvesting^{6, 7}, and the exploration of unknown territories⁸⁻¹⁰ due to the excellent environmental adaptability of soft and flexible materials. As **Figure 1a**, soft actuators are difficult to control accurately because they have soft bodies compared to conventional robots that have a rigid and discrete drive unit that allows precise control. However, they implement the adapted motion according to the geometric and physical properties of the target according to the control direction, because of their soft body which is a continuous driving part itself. So, soft actuators have strengths when applied to complex geometric environments and delicate properties as shown in **Figure 1 b**.

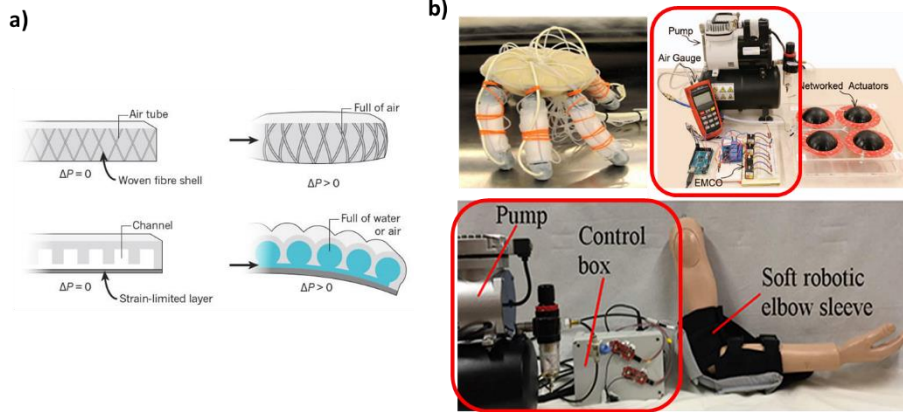


Figure 2 | Soft pneumatic actuators a) Mechanism of soft pneumatic actuators b) complicated, bulky, and necessary peripherals of conventional pneumatic power source

Among these, the soft pneumatic actuators, which inflate and deflate a chamber through the fluidic pressure as **Figure 2a**, show plenty of promise for future applications due to their high degree of design freedom, simple and low-cost fabrication, large force generation. However, despite the aforementioned advantages of soft pneumatic actuators, complex and bulky pneumatic peripherals, as shown in **Figure 2b**, have hindered their transformative development into untethered systems.

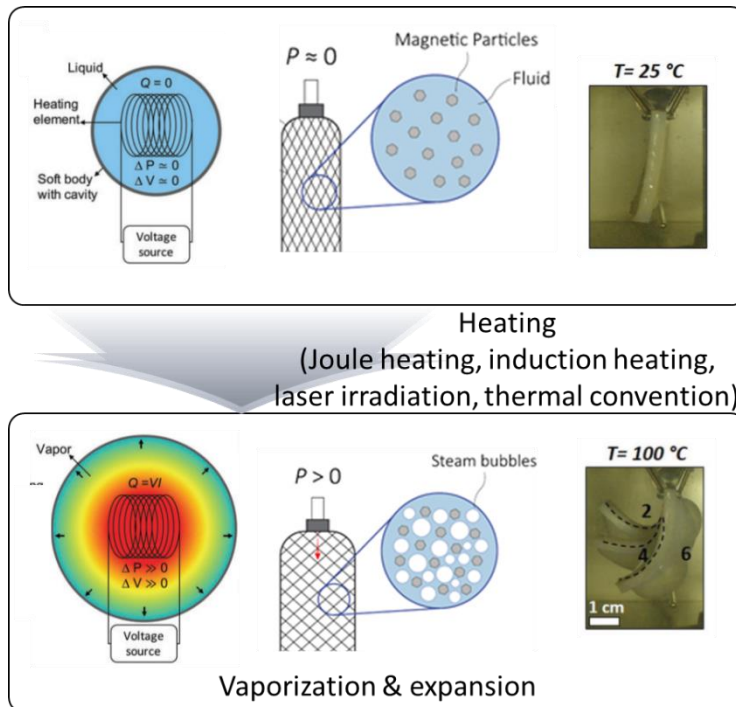


Figure 3 | Previous phase changing actuators and its mechanism

In this regard, several types of research attempted to replace bulky and rigid air compressors with soft devices. Cacucciolo et al. developed a soft electro-hydrodynamic pump for soft devices but it still requires a high-voltage power source operating actuators.¹¹ Some researchers have also studied soft thermo-pneumatic actuators which substitute the pneumatic source with vapor pressure generated from the liquid-gas phase transition in the chamber by exposing the chamber to a high-temperature environment^{12, 13} or by simply heating the liquid through several strategies including joule heating,¹⁴⁻¹⁶ laser heating,¹⁷ and induction heating¹⁸, as **Figure 3**. However, most of these approaches have only focused on the heating process to inflate the chamber and have not studied ways to improve the cooling process, which relies on the natural air convection to deflate the camber, making it unfeasible to reduce the operating time of the whole actuating cycle and thereby limiting its practical usage in soft robotics. To address this issue, Mishra et al. introduced a hydraulic soft actuator that passively cooled itself by mimicking perspiration, but there has been no work that incorporated the active cooling platform into the soft thermo-pneumatic actuator.¹⁹

Soft Thermoelectric Devices

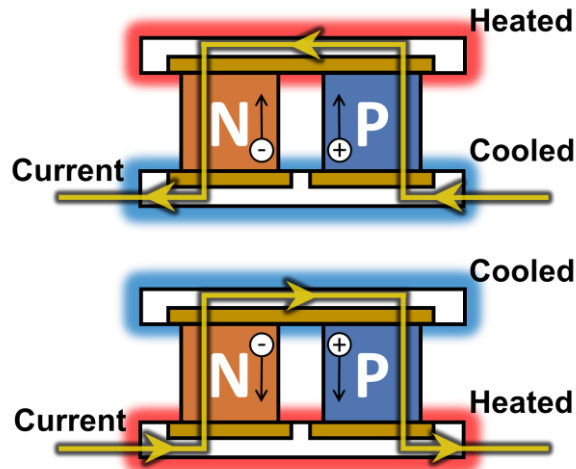


Figure 4 | A schematic for the mechanism of thermoelectric devices

The thermoelectric(TE) effect, or Peltier effect, allows the electrons (in the n-type TE leg) and holes (p-type TE leg) to diffuse toward one side of the junction in the presence of the electrical potential, causing the one side where the electrons and holes are densely populated to heat up while the other side where the charged carriers are sparsely populated to cool down as shown in **Figure 4**. This also implies that we can interchangeably switch between the heating and cooling modes just by reversing the direction of the electrical current because the surface that has been heated up due to the densely populated charged

carriers can be cooled down according to the direction of the electrical current. Indeed, the thermoelectric actuation can be operated with a semi-permanent lifespan of a minimum of 200,000 hours.²⁰ Moreover, the TE effect is already widely used for energy harvesting,²¹ calorimeter,^{22, 23} and thermal management²⁴⁻²⁶ in industrial fields. In particular, the thermoelectric effect generates a powerful cooling power that is already extensively employed in conventional systems, such as refrigerators, heat pumps, computing systems, and dehumidifiers.

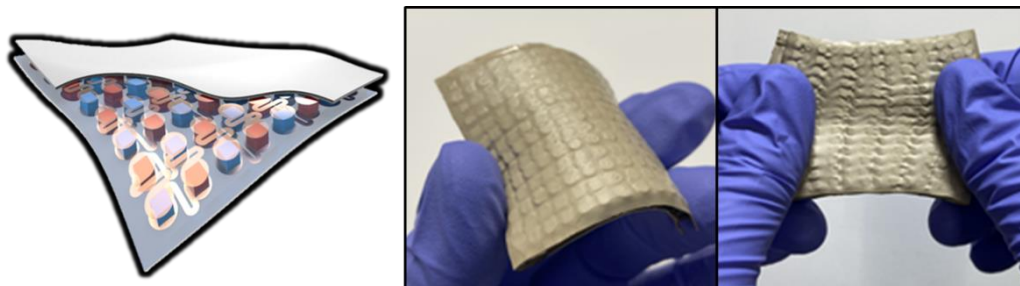


Figure 5 | A schematic and photographs of soft TE devices

Furthermore, soft TE devices comprising flexible electrodes, flexible substrates, and rigid TE legs, as shown in **Figure 5**, have been recently developed for soft and wearable electronics such as energy harvesting,²⁷⁻²⁹ thermochromic displays,³⁰ and thermal VR devices.³¹ The rapid and effective thermal management capability of TE devices to actively heat and cool has led to the high performance of wearable thermal VR^{31, 32} and thermochromic camouflaging devices.³⁰ Nevertheless, there has been no report that incorporated the soft TE device into the soft thermo-pneumatic actuator despite its notable thermal managing performance.

The soft thermo-pneumatic actuators do not require any auxiliary bulky and heavy pump or air chamber that most of the soft pneumatic actuators need to exert the force to the subject since actuators proposed herein thermally induce the reversible phase-change of the fluid. Such a pump-less configuration allows the entire system to be lightweight, minimal, and noise-free. Previously, several studies used several heating materials to fabricate pneumatic actuators¹⁴⁻¹⁸. Still, these actuators suffer from the slow response time to return to the liquid state because it solely relies on natural convective cooling to induce condensation. To address this issue, we employed the bi-modal soft TE device capable of heating and cooling the fluid inside the chamber, expediting the vapor-to-liquid transition (deflation of the chamber) by refrigerating the fluid with the active thermoelectric cooling mode.

1.2. Research Purpose

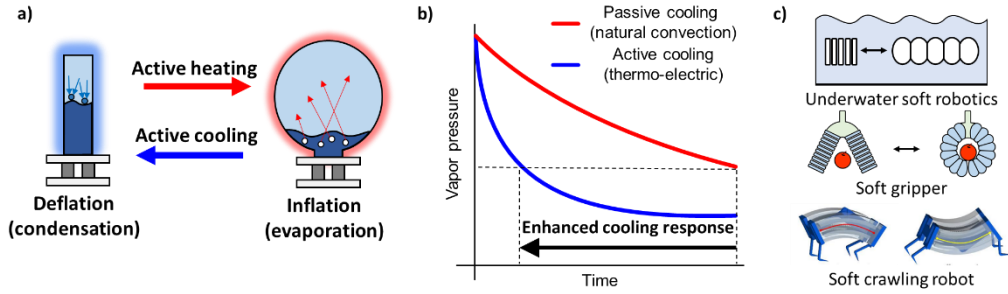


Figure 6 | Research purpose. a) soft thermo-pneumatic actuating module b) Enhanced cooling response of the actuating module c) Diverse soft robotic applications

As aforementioned, previous soft thermo-pneumatic actuators have been developed as various kind of type, but they still lack consideration of cooling strategies which can enhance response rate and usability. In this study, we developed a soft thermo-pneumatic actuating module (STPAM) employing the soft TE device which can control thermal gradient bi-directionally and liquid-gas phase transition to generate pneumatic pressure and expedite the actuating cycle in a pumpless configuration. Therefore, we successfully endowed not only active heating function but also active cooling function to soft thermo-pneumatic actuators. Also, we dealt with strategies to achieve effective heat transfer between TE device and actuating material, stable active cooling performance, and use in diverse environment and applications.

To improve the performance of the actuating module, we developed additional components such as thermally conductive substrate, copper fins, PCM heatsinks. Therefore, the developed module exhibited a faster deflation rate compared to natural convective cooling due to the effective active cooling functionality of the soft TE device, therefore shortening each actuating cycle and substantially improving the response time. Finally, in order to substantiate the customizable assembly of multiple STPAMs to achieve various motions and further verify its practical usage, we demonstrate a soft gripper and an autonomous untethered bio-inspired crawling robot based on the STPAMs. Furthermore, we exploit the module to underwater application such as buoyancy controller of the robotic fish.

Chapter 2. Soft thermo-pneumatic actuating module

2.1. Overview

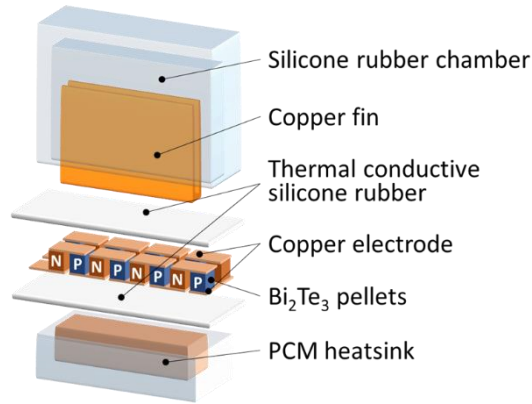


Figure 7 | Structure of the Soft thermo-pneumatic actuating module

Figure 7 shows the comprehensive structure of the developed STPAM, comprising a silicone rubber pneumatic chamber, copper fins, a soft TE device, and a PCM heatsink. The soft TE device comprises the thermally conductive silicone rubber layers and bismuth telluride (Bi_2Te_3) pellets, of which the n-type and p-type were connected alternately in series via the Cu electrodes. The TE device operated either in the cooling or heating mode depending on the direction of the current of the alternately arranged Bi_2Te_3 pellets due to the Peltier effect. Both inflation and deflation of the chamber were controlled by this bidirectional thermal control ability. The thermal conductive silicone rubber employed boron nitride (BN) micro-powder, which has high thermal conductivity ($550 \text{ Wm}^{-1}\text{K}^{-1}$) at room temperature,³³ as a filler to enhance the thermal conductivity. Copper fins were attached to moderate thermal energy exchange between the vapor and the soft TE device. To prevent the heat backflow from the soft TE device, the PCM heatsink was attached to the bottom of the device. The PCM offers an advantage for thermal management in that it stores and releases latent heat during phase transition without temperature change. Lastly, the silicone pneumatic chamber, containing the engineered fluid that accomplishes the actuating function through expansion and contraction, was attached to the top of the soft TE device.

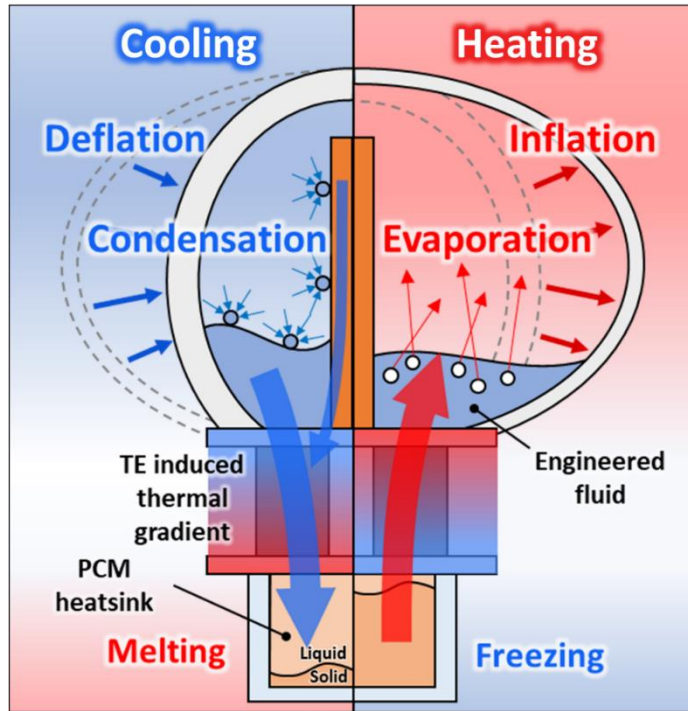


Figure 8 | A schematic of the comprehensive mechanism of the soft thermo-pneumatic actuating module

Figure 8 illustrates the working mechanism of the STPAM, where the chamber's inflation and deflation were controlled by the vaporization and condensation of the engineered fluid in the chamber. First, the soft TE device in the STPAM could heat and cool the fluid in the pneumatic chamber. In the heating mode, the fluid evaporated due to the heat generated from the soft TE device and inflated the chamber via its vapor pressure correspondingly. Meanwhile, the heat in the PCM heatsink was transported to the fluid by the thermal gradient induced by the soft TE device. On the other hand, in the cooling mode, the heat was transferred from the vapor to the heatsink via the surface of the copper fins, the fluid, and the soft TE device by the Peltier effect-induced thermal gradient in the TE pellets. Consequently, the condensation of the fluid induces a pressure drop in the chamber, which, subsequently, led to the deflation of the chamber. In this step, when the temperature of the heatsink reached the melting point, the heatsink stored the transferred heat as latent fusion heat and maintained this temperature during melting. The stored latent heat could be transferred to the engineered fluid to induce vaporization during the heating process.

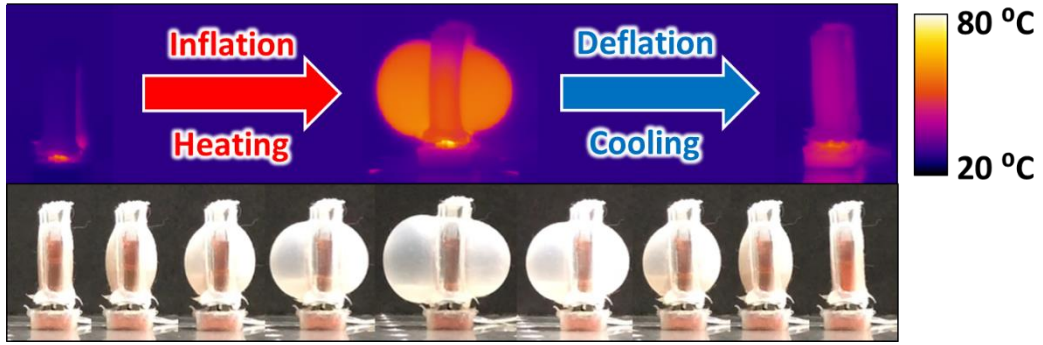


Figure 9 | Thermal images and photographs during heating (inflation) and cooling (deflation).

infrared (IR) image, the chamber inflated during the heating mode and deflated during the cooling mode. The Peltier effect-induced thermal gradient was confirmed by the difference in temperature between the chamber and PCM heatsink. The PCM heatsink of the inflated STPAM had a lower temperature than the chamber because the thermal gradient of the soft TE device was maintained during the heating process. On the contrary, since the thermal gradient was constructed in a reverse manner during the cooling process, the temperature of the PCM heatsink was higher than the deflated chamber.

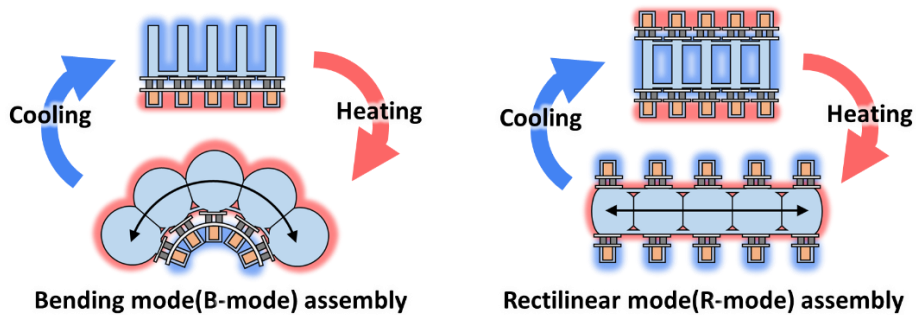


Figure 10 | Schematics for assemblies of STPAMs

For diverse robotic systems, modulization is essential so that the elements can be assembled in different designs based on their necessity. STPAMs can also be constructed in diverse structures to obtain several actuating functions. We assembled the STPAMs into the B-mode and R-mode assemblies, demonstrating bending and rectilinear motions, respectively.

2.1. Soft thermo-electric device

Characterization

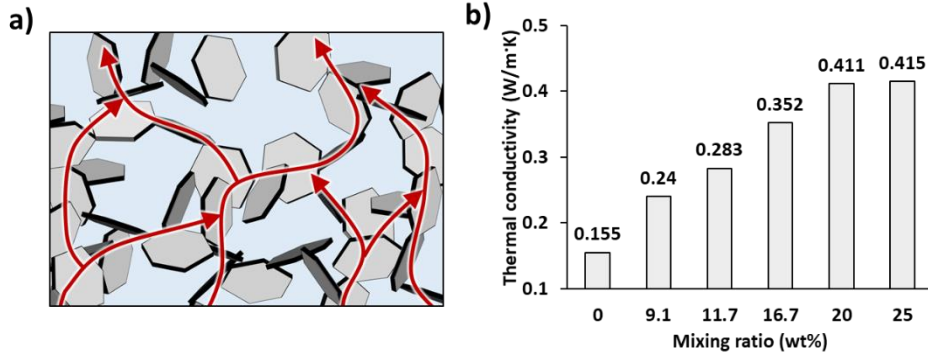


Figure 11 | Thermally conductive elastomer a) Schematic of thermal percolation network of BN micro powder b) Thermal conductivity of BN microplate/PDMS composite

Substrates of the soft TE device should exhibit high thermal conductivity to minimize parasitic heat loss during operation. However, the low thermal conductivity of common soft materials, including PDMS, hampers the performance of conventional soft TE devices. Therefore, we filled BN micro-powder, a promising thermal enhancer due to its high thermal conductivity, in the PDMS matrix to enhance the thermal conductivity of the substrate. Additionally, the thermal conductivities of the pure PDMS and BN/PDMS composites with five mixing ratios were compared to select the most appropriate mixing ratio of the BN micro-powder and PDMS. **Figure 11** shows that a higher mixing ratio guarantees higher thermal conductivity due to the effective heat transfer via the BN micro-powders percolation network. However, since the thermal conductivity of BN/PDMS composite with mixing ratios greater than 20wt% was similar and since the high concentration of the powder hindered the fabrication of the well-diffused BN/PDMS composite, the composite with 20wt% concentration, exhibiting 2.65 times the thermal conductivity of pure PDMS, was selected as the substrate material for the soft TE device.

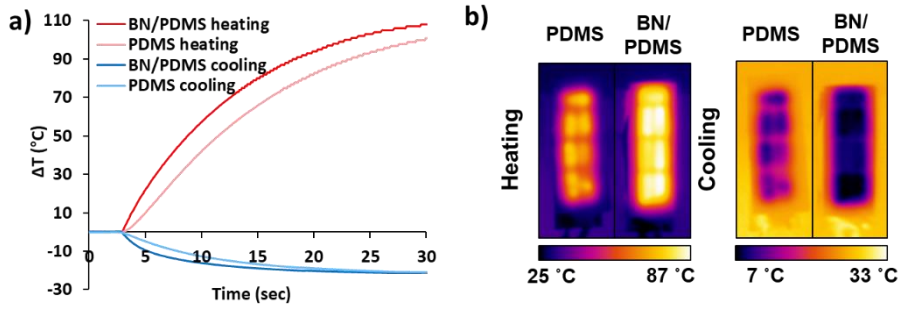


Figure 12 | Thermal managing performance of BN/PDMS composite a) Temperature change depending on time b) Thermal image

Figure 12 shows a higher TE performance of the BN/PDMS-based soft TE device compared to the pure-PDMS-based soft TE device. The temperature management of the BN/PDMS-based device occurred faster and was stronger compared to the PDMS-based device. The initial temperature change rate of the BN/PDMS-based device is significantly faster, and a difference in temperature change is even observed in the thermal image.

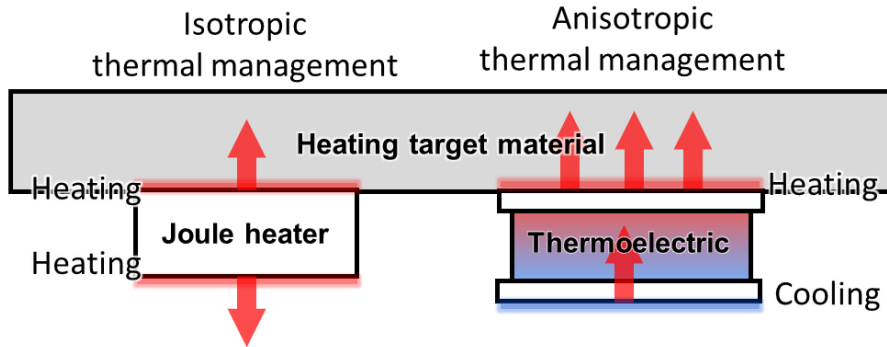


Figure 13 | A schematic represents isotropic thermal management of joule heater and anisotropic thermal management of the thermoelectric device.

Furthermore, to characterize the thermal managing capability of the fabricated soft TE device, we compare a Joule heater manufactured in the same dimension as a soft TE device using a Ni heating wire which is a common heating material, and silicone elastomer. As outlined in **Figure 13**, Joule heaters and TE devices have different thermal management strategies. In contrast to the Joule heater that transfers heat in an isotropic way, the TE device relies on anisotropic thermal management by generating a thermal gradient in the cross-plane direction. Thus, the TE device can reduce heat loss or even obtain heat on the cooling side, whereas the Joule heater heats both sides.

Heat flux of cooling and heating mode of Peltier device is known as below

$$Q_c = \alpha IT_c - k\Delta T - \frac{1}{2}R_e I^2 \text{ for the cooling mode}$$

$$Q_h = \alpha IT_h - k\Delta T + \frac{1}{2}R_e I^2 \text{ for the heating mode}$$

where the first term in the parenthesis signifies thermoelectric cooling/heating (α , I , T_c , or T_h stand for the Seebeck coefficient, electrical current, and temperature of the cold/hot junction respectively), and the second term represents heat transfer between two junctions (k , ΔT stand for thermal conductance of the thermoelectric pellets and temperature difference between two junctions respectively). Lastly, the third term indicates Joule heating and its sign convention varies according to the cooling/heating mode. Assuming that the Joule heater dissipates heat equally in both directions, the thermoelectric device can heat stronger by $\alpha IT_h - k\Delta T$ than the Joule heater.

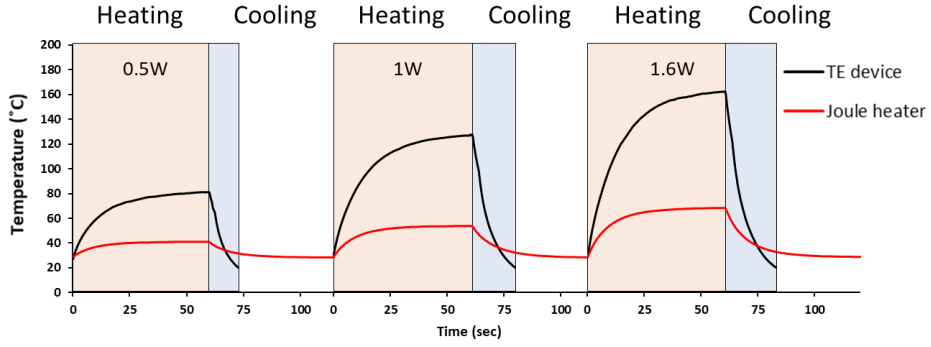


Figure 14 | Heating performance of TE device compared with Joule heater. Each experiment was heated with powers of 0.5W, 1W, and 1.6W. The temperature was measured with an IR camera.

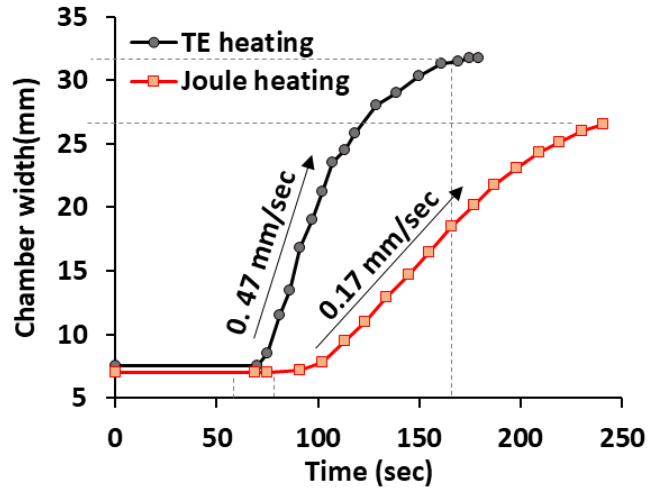


Figure 15 | Inflating a thermo-pneumatic chamber by TE heating and joule heating

Figure 14, Figure 15 depicts experimental data comparing soft TE device and joule heater which showed different performance due to the discrepancy in thermal managing strategy. **Figure 14** shows that the temperature of the TE device recovered faster during cooling, although it is much hotter than the Joule heater during heating. It implies that the TE device is not only capable of heating more efficiently, but also much more effective at cooling because of the bi-directional thermal management. Also, **Figure 15** shows the comparison between a Joule heater and TE device when the pneumatic chamber was inflated by heating. The expansion of the chamber is represented by the width of the expanded chamber. Both the soft TE device and the joule heater were operated at 1.6 W power. The chamber of the soft TE device began to expand at 70 sec, at the rate of 0.47 mm/sec. The chamber width had increased to 32 mm at 178 sec. On the other hand, the chamber of the Joule heater started to expand at 90 sec at the rate of 0.17 mm/sec. It expanded only up to the chamber width of 26.5 mm at 240 sec. This result implies that a

TE device is more suitable for the thermal management of a STPAM, even excluding the active cooling function.

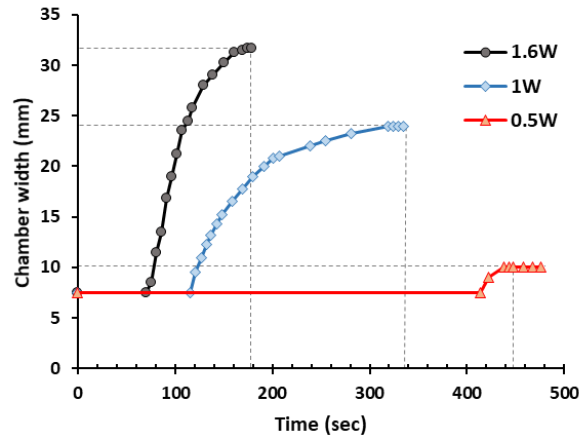


Figure 16 | Chamber width of TE device with different powers.

Additionally, the chamber expansion ability of the soft TE device depending on the applied power was measured. As shown in **Figure 16**, As the power increases, the maximum length of chamber width increases, and the time to reach it decreases. The chamber of the device operated at a power of 1.6 W, started to inflate from 70 sec, and reached the chamber thickness of 32 mm in about 200 sec. in the cases of 1 W and 0.5W, started to inflate from 115 sec and 415sec; and reached the chamber thickness of 24 mm and 10mm in about 200 sec and 450 sec, respectively. When the power exceeds 1.6W, the solder material melts and damages the device, so we were not able to test with a power higher than 1.6W.

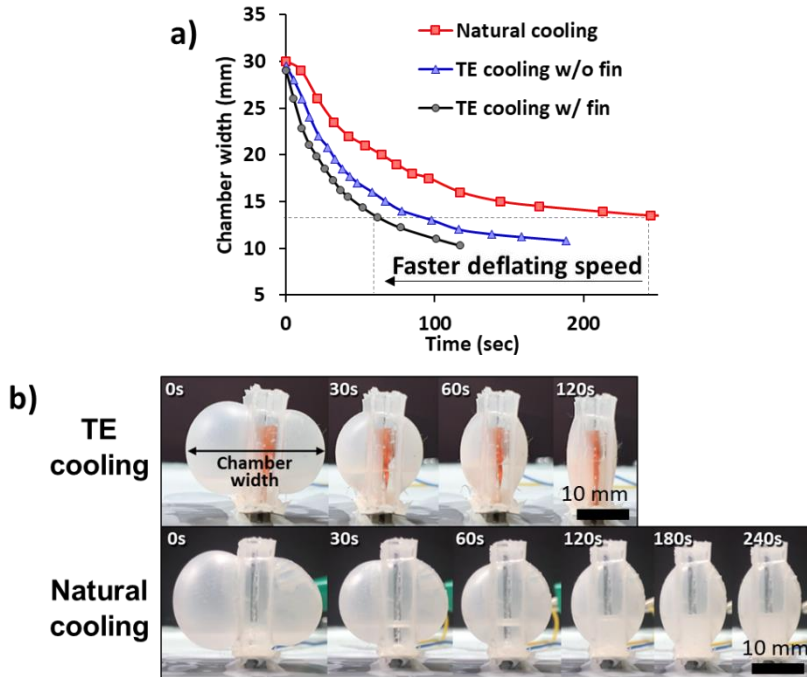


Figure 17 | Comparison of the pneumatic chamber deflation performance between natural cooling and thermoelectric cooling. a) Width of thermo-pneumatic chamber during the deflating. b) Photographs of the pneumatic chambers during deflation by thermoelectric cooling and natural cooling.

Compared to natural cooling, which employs natural convection and conduction to cool a heated and inflated chamber; the active cooling function of the soft TE device allowed for faster deflation of the chamber by compelling the condensation of the vaporized engineered fluid. Therefore, we compared natural cooling and active cooling to validate the effectiveness of the active cooling function. Please note experiments related to the cooling in this section (**2.1. Soft thermo-electric device**) were conducted with the soft TE device attached onto a metal table, which acted as a large heatsink, to derive maximum performance from the soft TE device during the comparison. Since TE device operates on the same principle as a heat pump using a Peltier-effect-induced thermal gradient, a heatsink to prevent the heat backflow is necessary. If there isn't any heatsink, the temperature would rise even more during heating, but the temperature may rise rather than descend due to the heat backflow during cooling. Therefore, in this study, a PCM-based heatsink was fabricated and applied. It will be dealt with in the next section (**2.2 PCM heatsink**). Also, the copper fins were attached to the soft TE device to accelerate condensation by extending the heat exchanging surface. As shown in **Figure 17**, active TE cooling shortened the deflation speed of the chamber. Based on the naturally cooled chamber's minimum width of 13 mm, active TE cooling deflated the chamber faster by 185

sec. In addition, the attached copper fins assisted the active cooling function. The TE device with copper fins deflated the chamber faster than the TE device without copper fins.

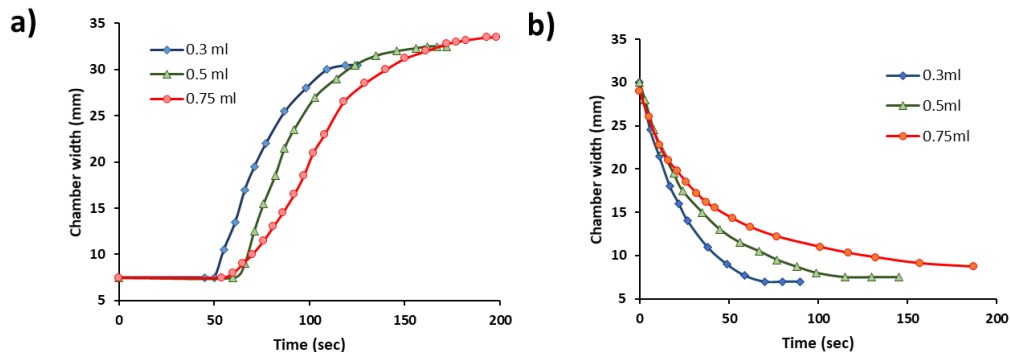


Figure 18 | Chamber width of TE device with different volumes of the active liquid during a) heating and b) cooling process. (The current magnitude: 2A (heating), 1.5A (cooling)).

Both inflation and deflation abilities of the soft TE device according to the volume of the engineered fluid in the chamber were characterized in **Figure 18**. As the amount of filled solution increased, the chamber expanded or deflated slower and the maximum/minimum chamber width increased during the heating process. A significant difference in the deflation rate was also observed depending on the amount of engineered fluid administered during the cooling process.

2.2. PCM heatsink

Background

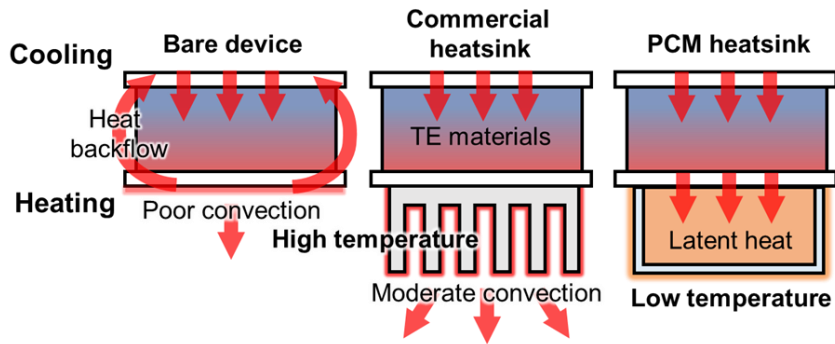


Figure 19 | A schematic describing the heat dissipation of the TE device without heatsink, with commercial heatsink, and PCM heatsink during cooling.

Employing the PCM heatsink for the STPAM offers two advantages: 1) preventing heat backflow through the dissipation of a moderate amount of heat and 2) achieving a low temperature, which has a lesser impact on the external environment compared to conventional heatsinks that dissipate more heat. If the heating surface of a TE device cannot dissipate heat successfully when operated, as shown in **Figure 19**, the backflow of the undissipated heat induces overheating of the cooling surface due to its poor convection. Therefore, a heatsink that dissipates heat from the heating surface is a vital component in the TE system. Furthermore, in the STPAM, a compact-sized heatsink is required to not hinder the actuating functions. Also, a soft interface and low operating temperature are required to easily bond to a soft substrate and not degrade the soft materials respectively. (Soft materials are relatively susceptible to high temperatures, so high temperatures may limit the application range of the actuating system.) From this point of view, commercial aluminum heatsinks, widely used due to their high convection coefficient and thermal engineered design, are not suitable because of their rigid interface and operating temperature that should be maintained too high for moderate convective heat transfer, as shown in **Figure 19**.

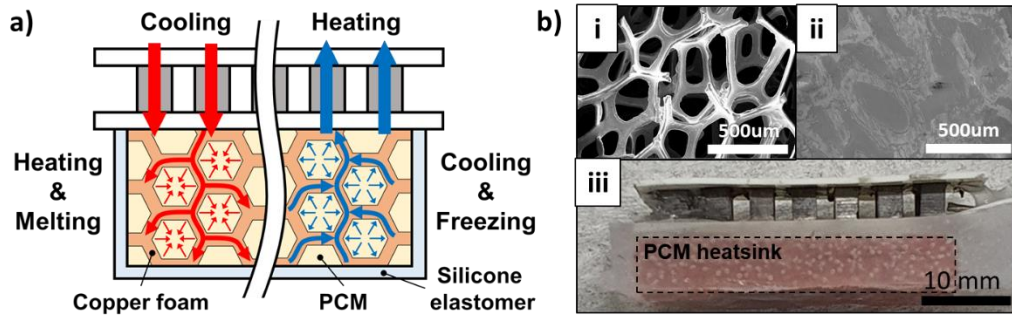


Figure 20 | PCM heatsink a) A schematic of the mechanism of the PCM heatsink. b) SEM images of (i) the pristine copper foam and (ii) the PCM filled copper foam and (iii) a photograph of the soft TE device attaching PCM heatsink.

To satisfy these requirements, we employed a PCM heatsink composed of paraffin, which has a low melting point and a large latent heat of fusion; copper foam, which has great thermal conductivity; and silicone rubber as the PCM, thermal conductivity enhancer, and packaging material respectively. **Figure 20a** shows the comprehensive operating mechanism of the PCM heatsink during both cooling and heating. The copper foam acted as a heat channel allowing uniform heat distribution, and the PCM absorbed and released the latent heat through the phase transition during the cooling and heating processes of the STPAM. The inner space of the foam structure was filled adequately with the PCM as **Figure 20b i-ii**. The PCM heatsink was attached on the bottom side of the soft TE device, as shown in **Figure 20b iii**.

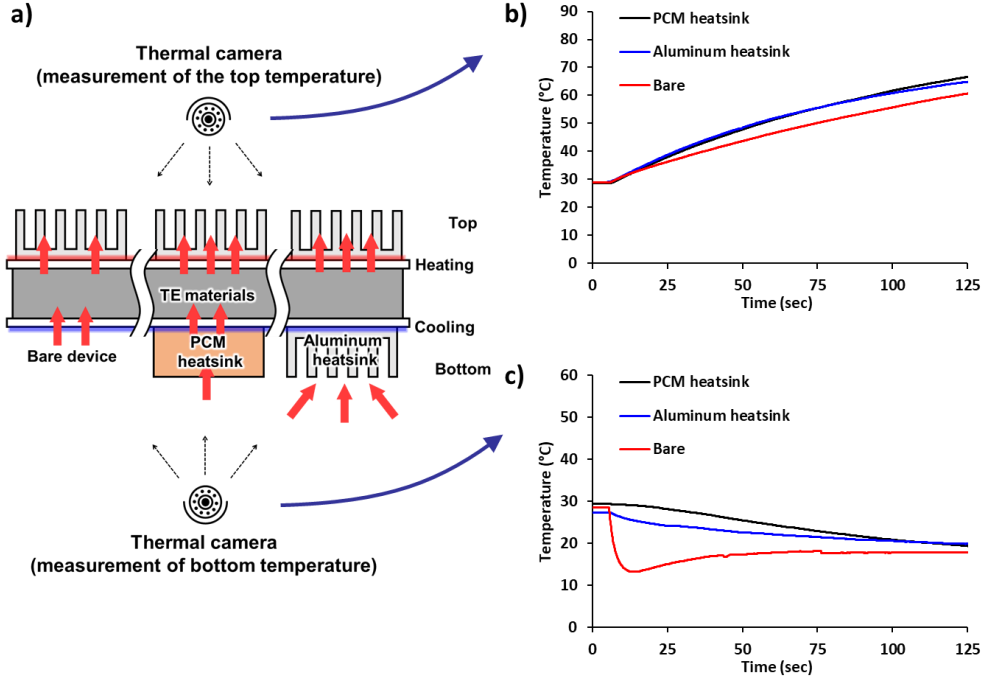


Figure 21 a) Schematic for the experimental setup to compare the heating ability of the soft TE device depending on an applied heatsink setting. The temperature of a) the top and b) bottom sides was measured by IR thermal camera in the heating mode.

We also characterized the heat supply capacity of the PCM heatsink during the heating process. The top and bottom temperatures of the TE device were measured as shown in **Figure 21a** during the heating process. The heating ability of each TE device, presented by the temperature change of the top-side (heating side) aluminum fin, would show how well each heatsink setting assists the heating mode. As shown in **Figure 21b**, soft TE devices with the aluminum and PCM heatsink attached show better heating ability than the bare TE device without a heatsink. It implies that TE devices with the heatsink absorbed heat better than the bare device at the bottom because heat absorption of the bottom side of the bare device only depends on the convective heat transfer from ambient air to the substrate and ambient air. On the other hand, in the cases with the heatsink attached, TE devices absorbed heat from the heatsink via conductive heat transfer which is much stronger than the convection from ambient air. Certainly, both aluminum and PCM heatsinks eventually absorb heat from the air by convection, but it seems more effective than absorbing heat directly from the air to the substrate like the bare device. Furthermore, there is no phase transition of the PCM during the heating process because the PCM heatsink is cooled, but it shows better performance than the bare device due to the difference in heat capacity resulting from the difference in the volume. As shown in **Figure 21c**, the bottom substrate cools rapidly due to its small heat capacity, on the other hand, the PCM heatsink cools slowly

while providing heat stably.

Characterization

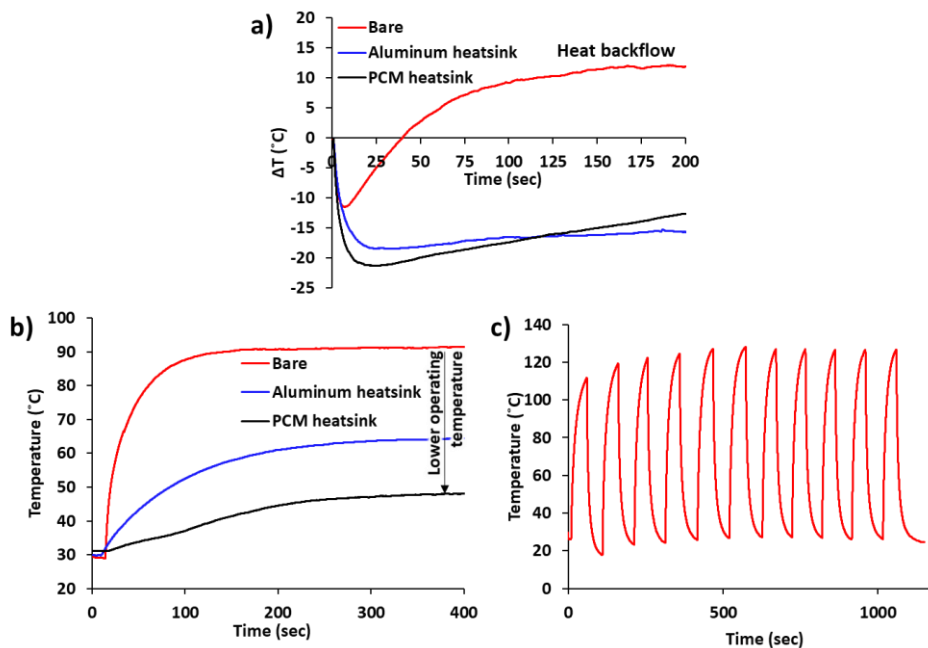


Figure 22 | Characterization of the PCM heatsink a) Temperature change of the cooling surface of the soft TE device. b) Temperature of the heat dissipating(heating) surface of the soft TE device. c) Repetitive temperature changes of a TE device with heatsink.

To verify the thermal management capability of the fabricated PCM heatsink, a soft TE device with the PCM heatsink attachment was compared to a bare soft TE device without any heatsink attachment and a TE device with an attached commercial aluminum heatsink. The temperature of the cooling side of each device was measured during operation, as **Figure 22a**. In the case of the bare TE device, the cooling side of the TE device was cooled down to 13 $^{\circ}\text{C}$ for 8 sec but eventually overheated to 35 $^{\circ}\text{C}$ due to undissipated heat. In addition, the aluminum heatsink and the PCM heatsink dissipated heat successfully. The TE device with the PCM heatsink, which cooled to a maximum of 2 $^{\circ}\text{C}$, showed better heat management performance compared to the device with the aluminum heatsink during 110 sec, which cooled to a maximum of 6 $^{\circ}\text{C}$.

The temperature of the heating surface during cooling was also an important factor because it may have degraded the soft substrates and the opposite side of the chamber that usually faces the interacting materials; thus, it was also compared as shown in **Figure 22b**. In the case of the bare TE device, the heating surface temperature soared to 90 $^{\circ}\text{C}$, but the

temperature dropped to 64°C when the conventional heatsink was attached. Furthermore, the TE device with the PCM heatsink attached showed a heating surface temperature of 48°C, 16°C less than the one shown by the conventional heatsink.

The durability and sustainability of the heatsink were also analyzed. The PCM heatsink maintained its thermal management capabilities during several cycles of heating and cooling, between 120°C and room temperature, as shown in **Figure 22c**.

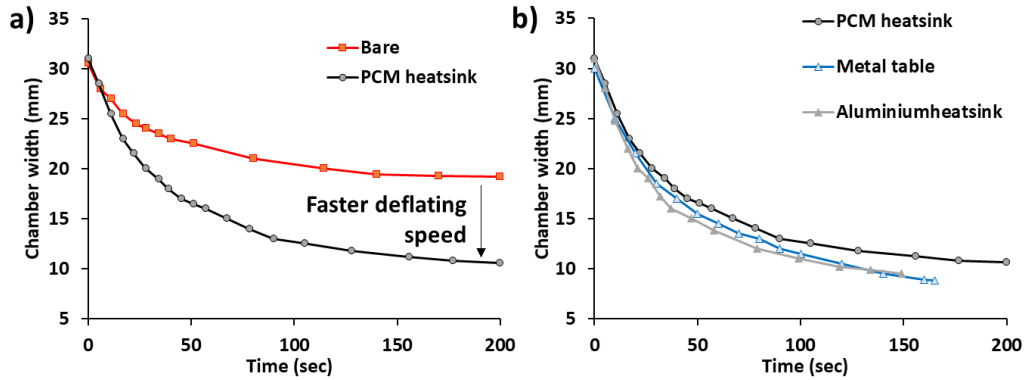


Figure 23 | Enhanced chamber deflating response by attaching the PCM heatsink. a) Comparison of the deflating performance of the STPAM without heatsink and with PCM heatsink. b) Chamber width of TE device during cooling mode with different heatsink, as attachment of the heatsink, paraffin, table, and commercial heatsink.

The chamber deflating ability of the STPAM based on the attachment and type of heatsink was also compared. As shown in **Figure 23**, each chamber started to cool by the chamber width of 31–32 mm after inflation. Compared to the bare TE device, where the chamber deflated only to 19 mm due to overheating, the TE device with the attached PCM heatsink deflated the chamber completely. **Figure 23b** shows that the deflating ability of the TE device with the attached PCM heatsink was similar to that of the TE device with the attached commercial aluminum heatsink and the TE device attached on the metal table acting as a semi-infinite sized heatsink.

2.2. Double-sided Soft Thermo-pneumatic Actuating Module

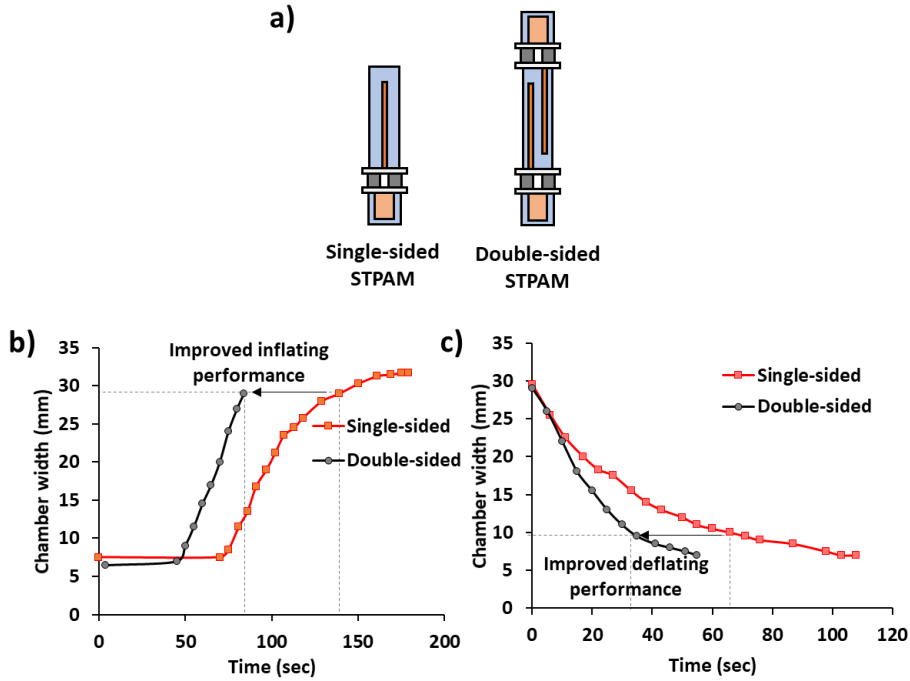


Figure 24 | Characterization of the double-sided STPAM. a) A schematic of the single-sided STPAM and the double-sided STPAM. b-c) Profile of the chamber width of the single-sided STPAM and the double-sided STPAM during (b) Inflating and (c) deflating.

The soft TE device and PCM heatsink could also be attached on both the top and bottom of the STPAM to improve the actuating performance, as shown in **Figure 24a**. Due to the doubled thermal management capability, the heating and cooling responses of the double-sided STPAM became shorter than those of the single-sided STPAM. During the heating process, the time taken to inflate the double-sided STPAM to the chamber width of 29 mm was reduced from 138 sec to 88 sec compared to the single-sided STPAM, as shown in **Figure 24b**. Moreover, the deflating time during the cooling process decreased significantly. Compared to the single-sided STPAM, which required about 70 sec for chamber deflation from 30 mm to 10 mm, the double-sided STPAM deflated the chamber in 37 sec, as shown in **Figure 24c**.

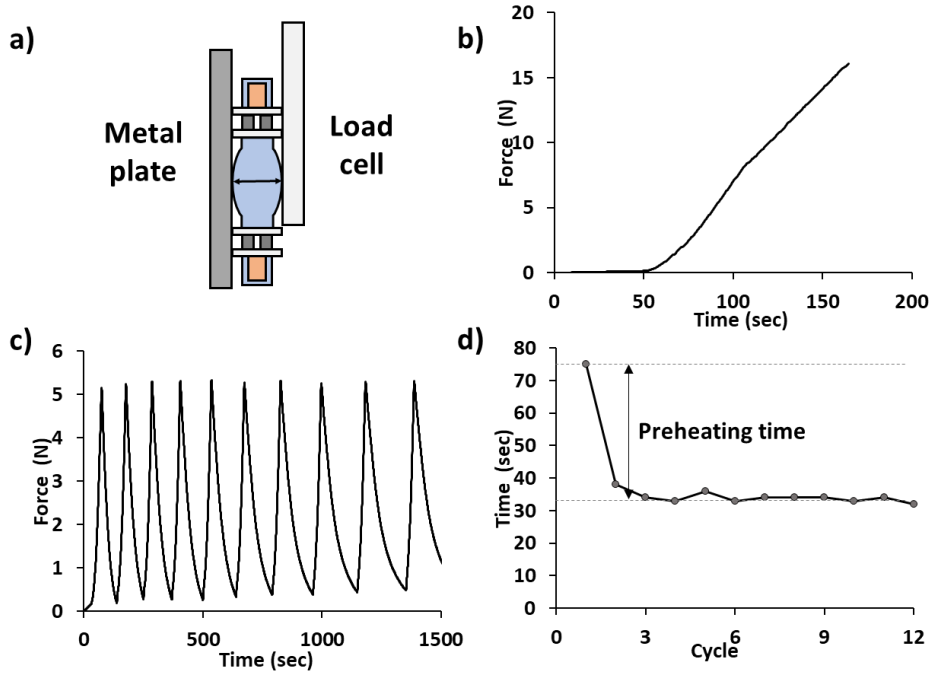


Figure 25 | Force characterization a) A schematic of the measurement setting b) The measurement of the inflating force of the double-sided STPAM. c) The measurement of the inflating force of the double-sided STPAM during repetitive operating. d) Time required for the double-sided STPAM to generate the force of 5 N according to repetition.

The inflating force measurement and repetition test were also conducted with the loadcell. The double-sided STPAM was located between the metal plate and the load cell in the deflated state, as **Figure 25a**. The load cell measured the inflating force of the STPAM. As shown in **Figure 25b**, the inflating force increased up to 16 N (1.63 kg f), 296 times the weight of the STPAM (5.5 g) over 175 sec. **Figure 25c** shows the results of the repetition test wherein the STPAM supplied the repetitive force of 5 N under stable conditions. We also measured the inflating time in each cycle, as shown in **Figure 25d**. Except for the first cycle wherein inflation took 75 sec, the STPAM revealed a constant inflation time (34–40 sec) because the STPAM needed to be preheated, involving the process of heating the engineered fluid to the boiling point during the first cycle.

Furthermore, Table 1 compares the performances of electrically driven thermo-pneumatic actuators including STPAM and shows that the STPAM produces the sufficient output force compared to the weight of the other actuators.

Table 1 | The performances of electrically driven thermo-pneumatic actuators

Reference	Weight	Power	Force	Force/weight	Mechanism
STPAM	13 g	2.1 W	15 N	1.15	thermo-electric
Chellattoan et al. ¹⁴ (2020)	42 g	45 W	1 N	0.0238	joule heating
Meder et al. ¹⁷ (2019)	1 g (except heating materials)	134 mW	0.068N	0.068	laser irradiation
Miriyev et al. ¹⁵ (2017)	6 g	15 W	60 N	10	joule heating
Miravkili Seyed et al. ¹⁸ (2020)	15 g (except heating materials)	32 W	31 N	2.067	induction heating

2.4. Assembly of the STPAMs

STPAMs facilitate not only inflation and deflation but also several practical actuating functions, such as bending and rectilinear motions, when assembled with appropriate designs. The B-mode assembly, of which the bottom silicone layer was connected, accomplished the bending motion. Furthermore, the B-mode assembly was exploited to demonstrate a soft gripper. The rectilinear motion was achieved by the R-mode assembly, comprising the double-sided STPAMs of which the soft TE device and the PCM heatsink were attached to both the top and bottom of the chamber. The bio-inspired untethered soft robot based on the R-mode assembly was then demonstrated. The untethered soft robot is inspired by earthworms, which carry out rectilinear locomotion from the repetitive elongation and contraction of body segments.

Bending mode (B-mode) assembly

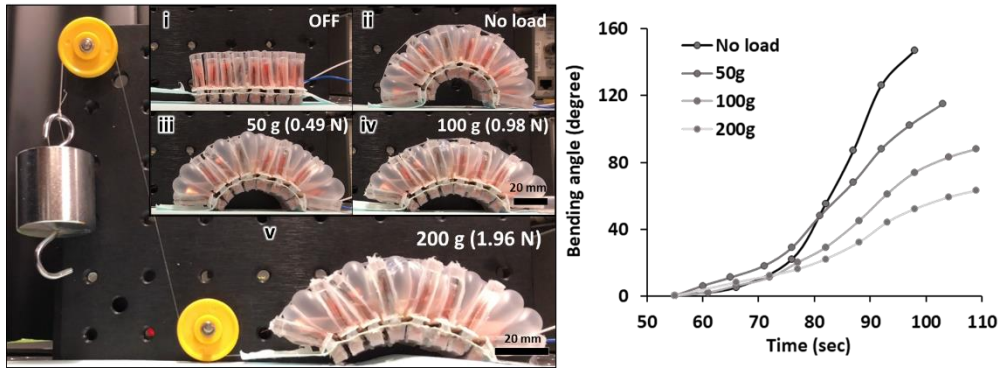


Figure 26 | the B-mode assembly of STPAMs under various loads a) Photographs of the B-mode assembly of STPAMs (i) at the OFF state and inflated under the load of (ii) 0g, (iii) 50g, (iv) 100g, (v) 200g. b) Bending angle profile of the B-mode assembly of STPAMs inflated under the various loads.

For practical use, the actuator was required to operate under the appropriate load. Therefore, we characterized the bending motion of the actuator under various pulling loads under experimental settings, as shown in **Figure 26a**. Two pulleys, various weights, and wires connecting a weight and the bending actuator were mounted on the floor, which facilitated the observance of the bending angles depending on the different weights applied. As shown in **Figure 26b**, the STPAM-based bending actuator accomplished bending under pulling loads of up to 200 g (1.96 N), 7.69 times the weight of the actuator (26 g). The actuator started bending after preheating for 55 sec and bent up to 150°, 115°, 88°, and 63° under the conditions of no-load, 50 g, 100 g, and 200g, respectively.

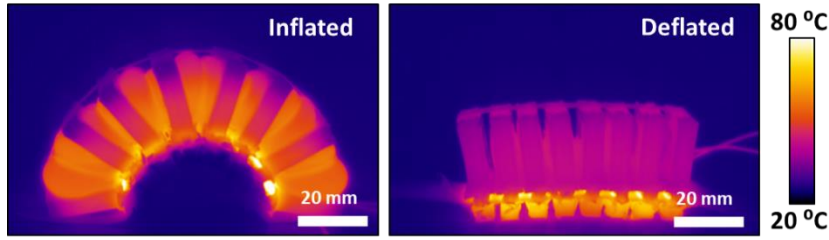


Figure 27 | Thermal images of B-mode assembly of STPAMs at heated and cooled state.

Figure 27 shows the temperature distribution of B-mode assembly of STPAM during heating and cooling mode. The PCM heatsinks of the actuator maintained lower and higher temperatures than the chamber during heating and cooling due to the Peltier effect-induced thermal gradient. Owing to these thermal gradients, the STPAMs could induce both heating and cooling by following only one principle.

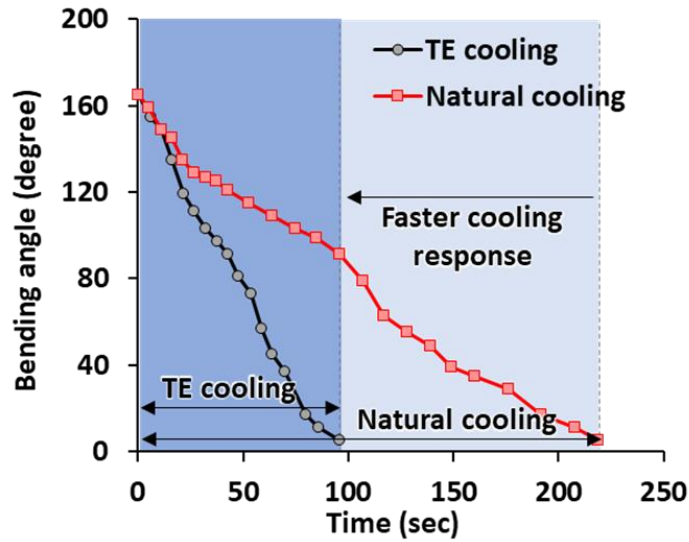
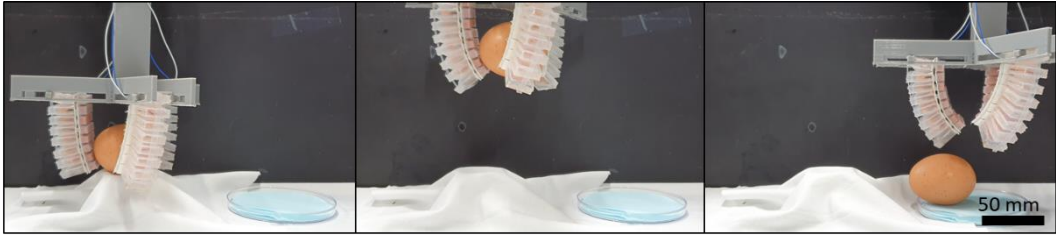
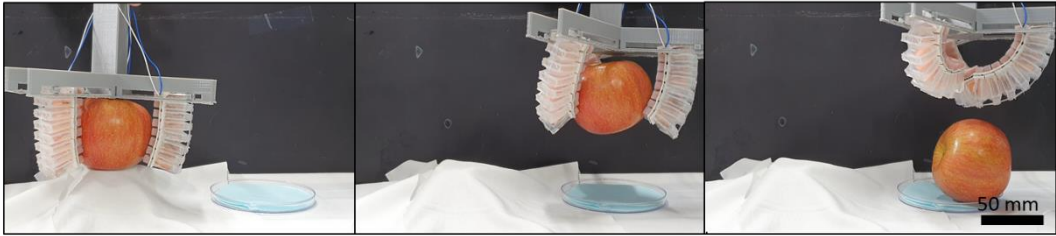


Figure 28 | Comparison of the TE cooling and the natural cooling during the deflation of the B-mode assembly of STPAMs.

The effect of the active TE cooling function for the bending actuator was validated, as shown in **Figure 28**. The active TE cooling and natural cooling of the actuator under the no-load condition were compared. In the case of active TE cooling, the actuator straightened about twice as fast compared to the case of natural cooling.



Egg: Weight: 60g, Gripping time: 9s, Releasing time: 14s



Apple: Weight: 153g, Gripping time: 26s, Releasing time: 7s

Figure 29 | A soft gripper based on B-mode STPAM assemblies gripping an egg and an apple.

We also tested the B-mode assembly's performance by designing a soft gripper for foods, as shown in **Figure 29**. The gripper comprised three STPAM-based soft bending actuators and a 3D-printed handle that fixed the actuators. Each finger weighed 26 g and consumed 15 W and 7 W during gripping and releasing, respectively. An egg, wrapped in a fragile shell, and an apple, twice as heavy as the actuators used in the gripper, were selected as the gripping targets. The soft gripper approached each target and successfully gripped and released them only using electrical power without any other peripherals, such as an air compressor.

Rectilinear mode(R-mode) assembly

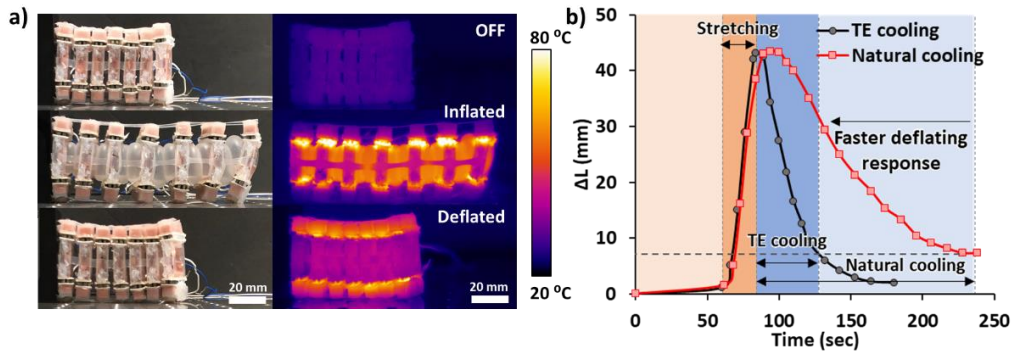


Figure 30 | The R-mode STPAMs assembly a) Photographs and thermal images of the operation of the R-mode assembly of the STPAMs. b) Length profile of the R-mode assembly of the STPAMs during the heating and cooling process.

The rectilinear motion was achieved by the R-mode assembly, comprising the double-sided STPAMs of which the soft TE device and the PCM heatsink were attached to both the top and bottom of the chamber. Additionally, a rectilinear stretching motion was achieved by the double-sided STPAM assembly, as shown in **Figure 30a**. The seven cells of the double-sided STPAM were connected with silicone rubber and comprised a rectilinear actuator of 55 mm in length. The STPAM-based rectilinear actuator stretched twice during heating and recovered its initial state via cooling. **Figure 30b** shows the actuation of the rectilinear actuator and a comparison between the active TE cooling and natural cooling during the operation. During the heating process, the preheating proceeded for an initial 35 sec, and stretching occurred fully in 23 sec. In the active TE cooling mode, the actuator spent 45 sec, 60 sec faster than natural cooling.

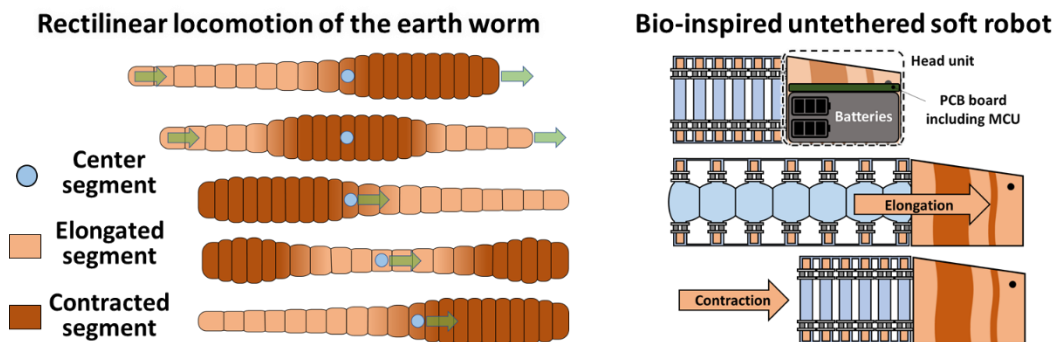


Figure 31 | A schematic for the bio-inspired untethered soft robot based on the R-mode assembly of STPAMs.

Untethered pneumatic soft robots should be big and strong enough to move with bulky

pneumatic peripherals. However, the STPAMs can be operated with compact electrical power sources, such as Li-ion batteries, without the need for any pneumatic peripherals. Therefore, we demonstrated a compact untethered soft robot, based on the R-mode STPAMs assembly, that can autonomously stop and re-operate depending on the surrounding environment, judged by the corrected temperature data. Due to the low-voltage-driven property and strong power of STPAMs, the robot containing compact Li-ion batteries and a simple MCU circuit, including wireless communication and temperature and humidity sensors, could move its body and power source by itself. As shown in **Figure 31**, the robot's locomotion is inspired by earthworms that alternately stretch and contract each body cell to move rectilinearly.

Figure 32 | A flowchart of bio-inspired untethered soft robot based on R-mode STPAM assembly

Figure 33 | Operation of the bio-inspired untethered soft robot a) (i) The collected temperature and humidity data by the soft robot and (ii) the traveled distance of the soft robot during demonstrating autonomous stop and go depending on environmental temperature. In (ii), Lines colored red and blue on the background indicate cooling and heating modes, respectively. (E) Snapshots of the moving, autonomously stopped, and re-operated soft robot.

sensing. As seen in **Figure 33**, while the robot was moving, it detected the temperature rise and humidity decline due to the turned-on IR lamp. As the detected temperature rises above 35°C, the robot stopped autonomously and then moved again when the temperature dropped because the lamp was turned off.

Table 2 shows the detailed specification of previous battery-driven untethered soft robots and actuators including our works. Recently, only a few works demonstrated under kilogram scale of untethered soft robotic systems based on dielectric elastomer actuators and shape-memory alloys. Mirvakili Seyed *et al.* developed an untethered soft thermo-pneumatic system based on remote induction heating, but the whole system, including the battery and induction heating system of unknown weight, is bulky and expected to be heavy. Besides, other untethered soft pneumatic robotic systems employing motors to supply pneumatic or hydraulic power are very heavy. However, the STPAM-based untethered soft robot achieved light-weight and appropriate outpower. Also, considering the operating cycle, the untethered robot is expected to operate for 53 minutes (20 cycles).

Table 2 | Untethered electrically-driven soft robots and actuators

Reference	Weight	Battery	Power	Force	Actuating mechanism	Application
The STPAM-based untethered soft robot	170 g	7.4 V battery (700 mAh), two 1.5 V batteries (1,250 mAh)	14.7 W	15 N	thermo pneumatic (thermo-electric)	crawler
Mirvakili Seyed <i>et al.</i> ¹⁸ (2020)	15 g (only actuating part)	two Li-ion batteries (3,000 mAh)	32 W	31 N	thermo pneumatic (remote induction heating)	gripper
Li <i>et al.</i> ³⁴ (2021)	-	3.7 V Li-ion (2,500 mAh)	3.8 W	-	Dielectric elastomer actuator	robotic fish
Huang <i>et al.</i> ³⁵ (2019)	30 g	3.7 V Li-po (200 mAh)	9.62 W	0.2 N	shape-memory alloy	crawler
Li <i>et al.</i> ³⁶ (2021)	1,500 g	11.1 V battery (800 mAh)	-	382 N	soft pneumatic (supplied by motor)	gripper
Li <i>et al.</i> ³⁷ (2018)	1,100 g	10,000mAh battery	-	25 N	soft pneumatic (supplied by motor)	crawler
Tan <i>et al.</i> ³⁸	5,750 g	12V battery	-	100 N	soft hydraulic	underwater

(2021)					(supplied by motor)	crawler
Usevitch Nathan <i>et al.</i> ³⁹ (2020)	29,000 g	14.8 V batteries (1,300 mAh) 20 EA	-	30 N	Soft pneumatic (rolling by moter)	untethered isoperimetric soft robot

2.5. Method

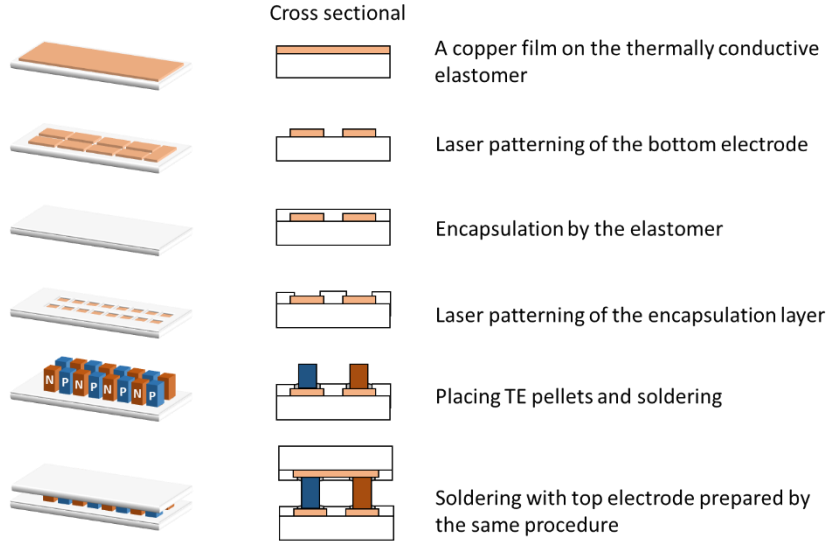


Figure 34 | A schematic for detail fabrication process of the soft TE device

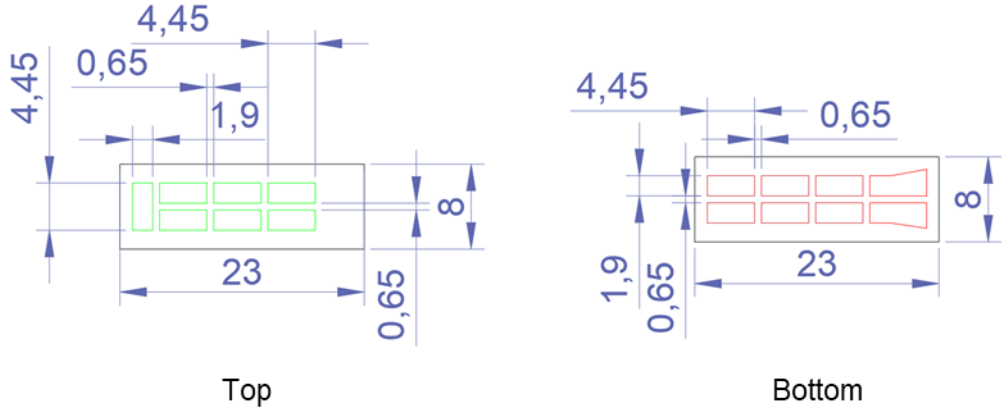


Figure 35 | The Design of the top and bottom electrode and substrate. (Unit: mm)

Soft thermo-electric device fabrication: The soft TE device was fabricated as shown in **Figure 34**. The BN micro-powder (Graphene Supermarket) was blended into polydimethylsiloxane (PDMS) (Dow Corning) in a weight ratio of 1:5 to improve the thermal conductivity of the silicone rubber. The glass sheet was covered by the mixture and spin-coated at 370 rpm for 60 sec. The mixture was then placed in an electric oven at 80°C and cured for 30 min. After curing, a 25 μm thick Cu foil (Alfa Aesar) was placed on the thermally conductive rubber substrate and ablated by UV-laser (Nanio Air 355-3-V, Innolas, $\lambda = 355 \text{ nm}$) to pattern the interconnected electrodes as the design shown in **Figure 35**. The BN/PDMS mixture was spin-coated on the electrodes at 700 rpm for 60 sec and cured in

an electric oven at 80°C for 30 min to encapsulate the copper electrode. The square holes fitted with the thermoelectric legs were laser ablated without affecting the copper electrodes and then peeled off to uncover the interconnected electrodes. The counterpart encapsulated interconnection electrode was fabricated with the same procedure. Solder paste (Koki, S3X48-M310D-3k) was applied to the exposed interconnected electrodes to mechanically solder the alternately aligned p-type and n-type Bi_2Te_3 thermoelectric legs (Wuhan XinRong New Materials Co., Ltd, 1.4 mm x 1.4 mm x 2.5 mm) with the electrodes at 310°C for 10 min on a hotplate. Following the same process, the Bi_2Te_3 thermoelectric legs were soldered to the counterpart substrate so that the p-type and n-type thermoelectric legs were connected in sequence. The dimension of the fabricated soft TE device was 23 mm x 8 mm x 3 mm.

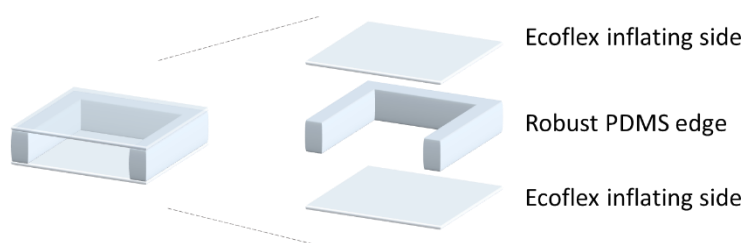


Figure 36 | A schematic of the pneumatic chamber structure.

Pneumatic chamber fabrication: The pneumatic chamber comprised the robust edge, acting as a backbone to prevent unintentional deformation, and the inflated side, as shown in **Figure 36**. The robust edge, PDMS, was cured on the 3D-printed PLA mold for 24 hours at room temperature. The inflated part, Ecoflex 00-30 (Smooth-On, Inc.) was spin-coated at 120 rpm for 90 sec and then pasted on the cured PDMS edge. Thus, a rectangular pillar-shaped pneumatic chamber was fabricated. Finally, the STPAM was fabricated by attaching the copper fins, pneumatic chamber, and PCM heatsink to the soft TE device. Copper fins, comprising 25 μm copper foil, and the pneumatic chamber were attached to the top of the soft TE device by conductive epoxy (Chemtronics) and Sil-Poxy (Smooth-On, Inc.), respectively. The outer dimension of the chamber was 5 mm x 20 mm x 20 mm, and the thickness of the inflating side was 400 μm .

PCM heatsink fabrication: For fabricating the PCM heatsink, 5 mm thick copper foam (Advanced Materials Development Expert Store) was cut to the size of the thermoelectric element. The PCM, Paraffin (Sigma Aldrich 327204), was dissolved and absorbed into the copper foam. The copper foam containing the PCM was coated by Dragonskin 10 (Smooth-On, Inc.) to prevent loss of the PCM. Finally, the PCM heatsink was attached onto the bottom of the TE device by Sil-Poxy. The dimension of the fabricated heatsink was 5 mm x 20 mm x 6 mm. The dimension of the PCM heatsink was determined

in consideration of interference between heatsinks during the bending operation of the L-mode assembly. As shown in **Figure 37**, the dimension of the heatsink assures a bending angle of 28° for a single joint of the assembly, so the B-mode assembly can bend up to 196° .

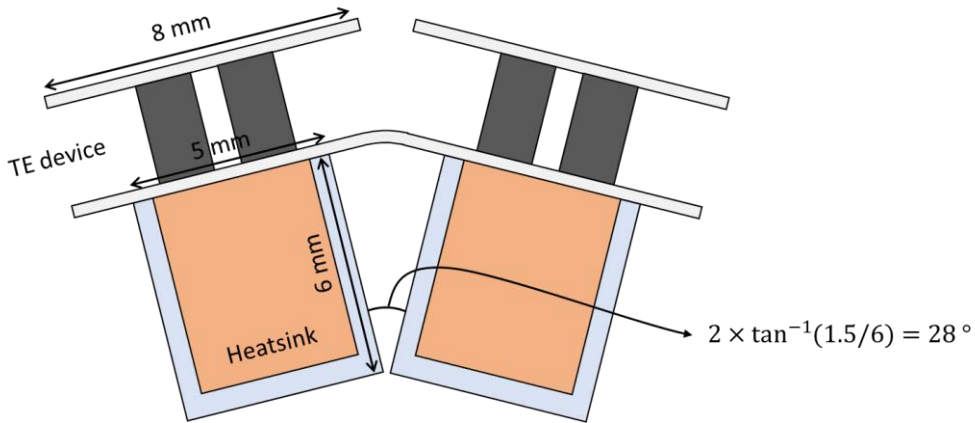


Figure 37 | Schematic of a bending part of B-mode STPAM assembly

STPAM fabrication: the STPAM was fabricated by attaching the copper fins, pneumatic chamber, and PCM heatsink to the soft TE device. Copper fins, comprising a couple of $25\ \mu\text{m}$ thick copper foil with $15\ \text{mm} \times 15\ \text{mm}$ dimension, and the pneumatic chamber were attached on the top of the soft TE device by conductive epoxy (Chemtronics) and Sil-Poxy (Smooth-On, Inc.), respectively. Finally, the STPAM fabrication was completed by attaching the PCM heatsink onto the bottom of the TE device by Sil-Poxy. The dimension of the fabricated STPAM was $23\ \text{mm} \times 8\ \text{mm} \times 28\ \text{mm}$.

Engineered fluid: Novec™ 7100 Engineered Fluid (Sigma-Aldrich, SHH0002) with a boiling point of 61°C was used as the active fluid resulting in the inflation and the deflation of the chamber by vaporization and condensation. The fluid was injected to the chamber via 26 gauge needle.

B-mode assembly of the STPAM fabrication: For the bending motion, eight single-sided STPAMs were fabricated on a larger bottom substrate. Each module was connected serially via the bottom copper electrode. The top layer of each soft TE device was separated to render flexible motion. The process of fabricating the B-mode assembly was the same as the process mentioned above, except for designing the interconnected electrodes. The interconnection of eight electrodes, encapsulated in the BN/PDMS mixture, was done in series, a process different from the unit thermoelectric device. Therefore, the bottom part of the thermoelectric device was connected with the integrated copper electrodes and cured BN/PDMS mixture. On the other hand, the top part of the thermoelectric device, cured

BN/PDMS mixture between the actuating chambers, was cut along the edges of the chambers to activate the degree of freedom upon chamber inflation. As the actuating chambers were inflated, the top part of the thermoelectric device widened, whereas the bottom part compressed. Also, the top of each chamber was connected by silicone rubber for recovery motion.

Thermoelectric pneumatic gripper fabrication and experiment: The PLA gripper support was printed using a 3D printer. The support comprised two parts: a handle part and a gripper holding part. The shape of the handle was a triangular prism. On each side of the triangular prism, three parts that could hold the thermoelectric gripper protruded. The three thermoelectric pneumatic B-mode assemblies were placed around the center of the gripper support so that the bending direction was directed toward the center of the support. The three thermoelectric pneumatic bending actuators were connected in series and held the object by inflating it with a current of 2 A. Conversely, by applying a current of 1.5 A in the opposite direction, the actuators contracted to place the object in a different place. The objects used in this experiment were a fragile egg and a relatively heavy apple. The gripper was operated after preheating it suitably for faster operation.

R-mode assembly of the STPAM fabrication: The process of fabricating the R-mode assembly was almost the same as the aforementioned process, except for the chamber design and connections between each thermoelectric device. The chamber was perforated at the top and bottom. The non-deformable corners were made of PDMS, and the expanding and contracting parts were made of Ecoflex. The thermoelectric devices with the fin were attached to the upper and lower sides of the chamber so that they could inflate and contract faster. In terms of connection, the seven independent thermoelectric devices were connected in series with the wires. The chambers at the front and rear of the thermoelectric devices that were connected in series were attached with the PDMS, which did not stretch well because it was not required to be inflated.

Thermoelectric pneumatic untethered rectilinear locomotion fabrication and experiment: To wirelessly move the thermoelectric element linearly, we designed a circuit that could control the voltage level. Sawtooth-shaped PET films were attached to the bottom of the heatsink. Regarding the STPAM circuit design, a single 7.4 V battery (700 mAh) and two 1.5 V batteries (1250 mAh) were used to power the thermoelectric pneumatic rectilinear actuators and microprocessors. Since it was necessary to alternate between the thermoelectric heating and cooling modes, double-pole, double-throw relays were used to switch between the two thermal modes. The 7.4 V battery was responsible for relaying the heating mode and powering the microprocessor at 3.3 V using a regulator. The relays assigned to the 7.4 V battery applied the appropriate output to the SPTAM via the

PWM control. The two 1.5 V batteries connected in series were employed to relay the cooling mode of the device. RF wireless communication was employed because a longer wavelength ensures communication for longer distances. The sawtooth shape PETs were designed to generate different friction according to the forward and backward directions, so that R-mode STPAMs assembly moves in a certain direction as it repeatedly contracts and expands. By attaching the sawtooth-shaped PET to the bottom of the heatsink, a linearly movable thermoelectric device was fabricated. The robot was programmed to autonomously stop and re-operate depending on the temperature sensed via the integrated sensor, as shown in **Figure 38**.

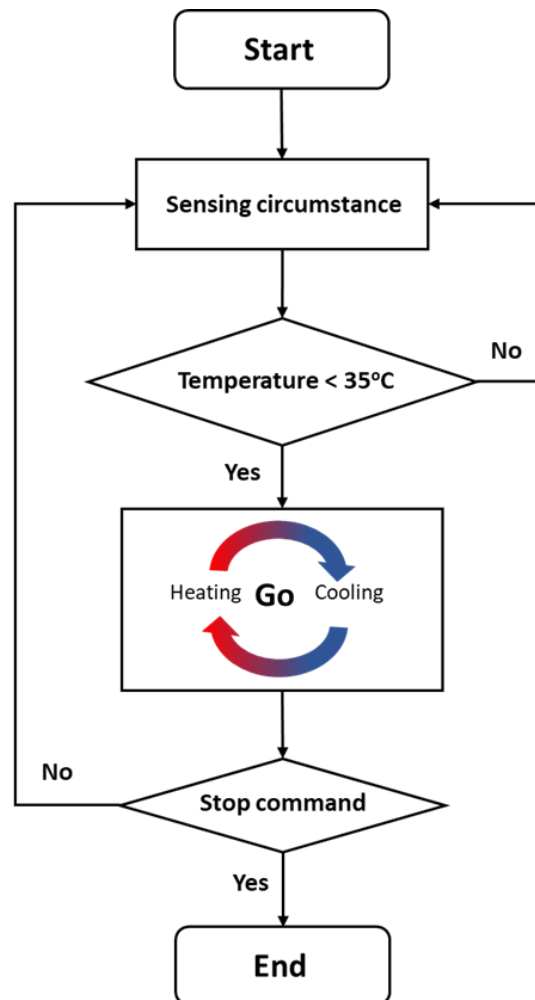


Figure 38 | Algorithm diagram for the autonomous operation process of the bio-inspired untethered soft robot based on R-mode STPAM assembly

Chapter 3. Soft fish-bot (underwater application)

3.1. Background & Introduction

Background

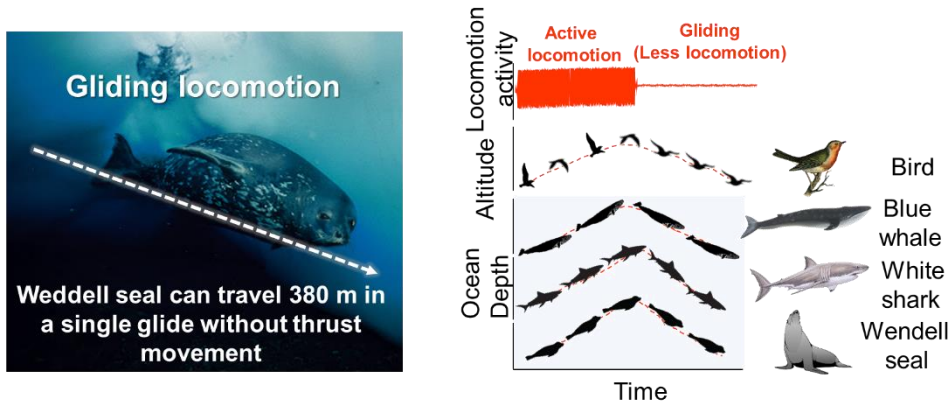


Figure 39 | Gliding locomotion from nature

Locomotion is the essential ability for the survival of animals in nature as it is required to prey on, flee from predators and even move to their microhabitats. Particularly, underwater locomotion appears to require a tremendous amount of energy because water exerts a counteractive drag force against the progressing direction. However, marine animals are reported to expend a much lower cost of transportation on locomotion than aerial and terrestrial species like birds or humans⁴⁰, largely because they utilize intermittent gliding interspersed with energetic locomotion to reduce energy. Despite their divergent evolutionary background, marine vertebrates actively sway their tails to ascend in water and perform much fewer locomotive activities as they glide downward so that they can simply translate the potential energy into the horizontal traveling distance.^{40, 41} Also birds make similar locomotive activities, although they live in the air rather than underwater, as shown in **Figure 39**. Notably, it is reported that Weddell seals (*Leptonychotes weddellii*), for instance, can travel a distance as far as 380 m as they descend 80 m downward during a prolonged underwater gliding. As evidence of convergent evolution, such a generic behavior can be observed in most marine mammals, regardless of the propulsion mechanism and body size to save the aerobic cost of energy for locomotion.⁴²

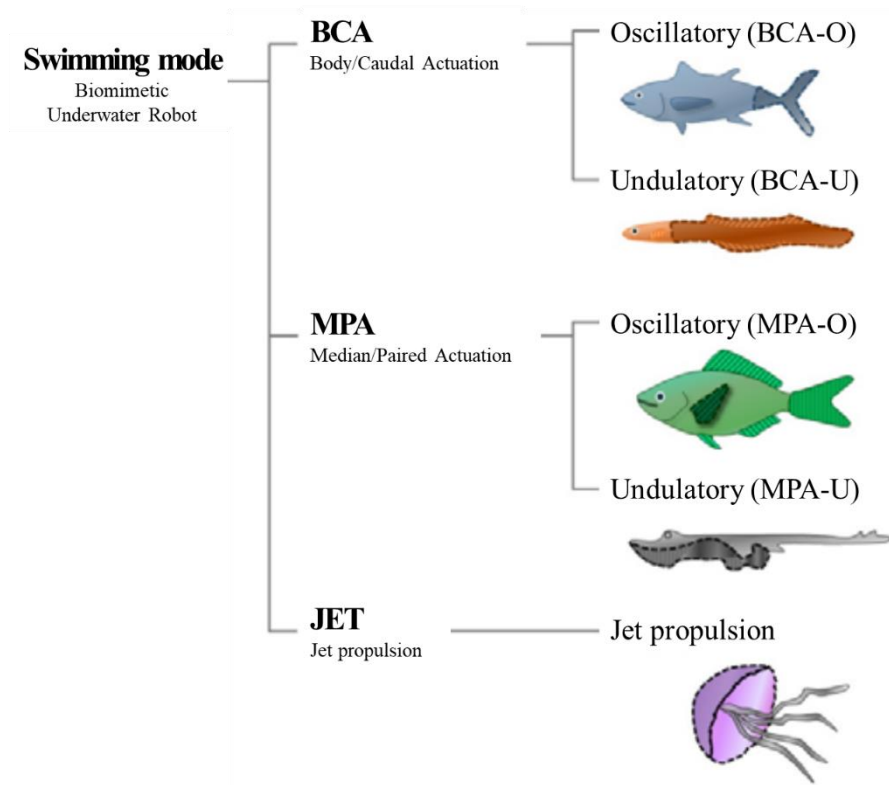


Figure 40 | Classification of swimming modes of biomimetic underwater robots⁴³

On the other hand, significant efforts have been dedicated to making soft swimming robots and even mimicking marine animals' propulsive mechanisms.^{34, 44-53} In order to freely move in the underwater environment in the presence of antagonistic drag force, the marine species resorted to different propulsive mechanisms, which can be classified into three main categories, including (i) body/caudal actuation (BCA) that employs the main body or caudal fins for locomotion, (ii) median/paired actuation (MPA) that utilizes fins other than caudal fins to locomote, and (iii) jet propulsion which fills the muscular cavity and force out water as a means of propulsion just as jellyfish and cephalopods move, as **Figure 40**. The BCA and MPA modes can be subdivided into oscillatory and undulatory modes depending on the swimming mechanisms.⁴³ The undulatory mode produces a traveling wave along the body or fins to repel water rearward, exemplified by eels and rays. In contrast, the oscillatory mode propels itself largely using a fin that oscillates periodically as tuna and sharks move.^{50, 54}

Several studies on underwater robotics successfully mimicked the propulsive movements of MPA-U⁴⁶ and -O⁵¹ while a large number of fish-like robots replicated the locomotion of BCA-O^{34, 47-50, 52, 53, 55-63}, and BCA-U.^{64, 65} Besides MPA and BCA modes, other studies attempted to imitate the locomotive motion of jellyfish⁶⁶ and scallop⁶⁷ that represents the jet propulsion mechanism, while other underwater robots included

locomotion of the crawling movement of octopus ⁶⁸, swimming of turtle⁶⁹, crawling/swimming of starfish ⁷⁰, and breaststroke movements of frogs ⁷¹ that do not fall into any of three categories of propulsive mechanisms. Most of these underwater robots that mimic MPA, BCA, and jet propulsion rely on soft components because rigid materials limit replicating natural propulsive locomotion of different marine species with soft exoskeletons. However, none of these soft robots demonstrated the strategic gliding locomotion of marine vertebrates despite their high effectiveness. Previous literature focused on realizing the horizontal movements (forward or steering) of the underwater species since underwater fish robots in most of these works lack functions move vertically in the water, even though the intermittent locomotive gliding can offer the energy-saving feature as it enables translation of the potential energy into horizontal travel distance. Besides, many of the previous works supplied a power source or gave commands to the underwater robots through rigid tethered systems, which constrain the travel distance of the underwater robots and ultimately limit the practical application of these works.

Introduction

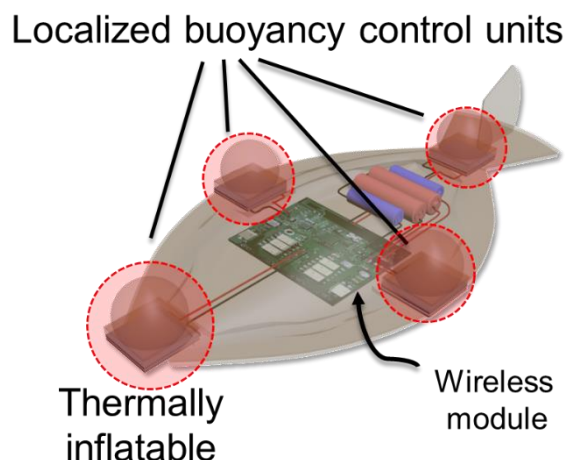


Figure 41 | A schematic for soft Flatfishbot controlled by wireless module and thermally inflatable localized buoyancy control units

Aforementioned, most marine vertebrate species perform a high level of locomotive activities only as they ascend in water and then show notably decreased locomotion as they dive into the depth. Here, inspired by the intermittent locomotive gliding of the marine vertebrates, we developed a biomimetic flat fish robot (Flatfishbot) that can realize the strategic locomotion of marine animals and further move in the three-dimensional space inside water by wirelessly controlling localized buoyancy as shown in **Figure 41**. To better reproduce the intermittent locomotive gliding, we modified STPAM and designed an underwater soft thermo-pneumatic actuating module (uSTPAM) based on the

thermoelectric effect that enables a substantial reversible volume change with a rapid response time since the movement of the marine animals involves an enormous depth change.

Transverse Section of a Teleost Fish Body

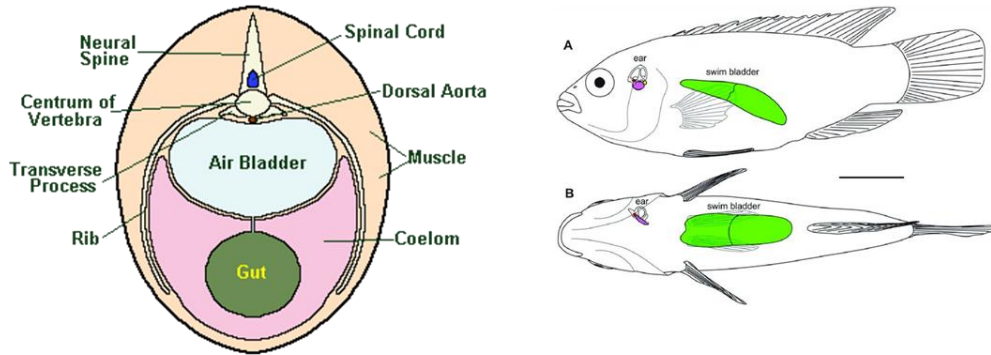


Figure 42 | The air bladder of teleost fishes

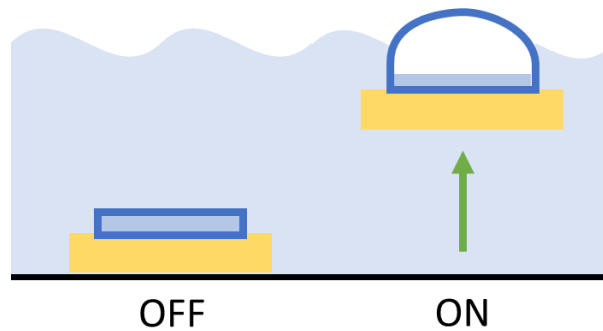


Figure 43 | Schematic for an uSTPAM that acts like air bladders of fish

In a way, the uSTPAMs resemble the air-bladder of a specific fish type in which volume can freely change by the gas exchange with the blood vessels to control buoyancy when they need to move upward or downward.⁷² Prior works report the buoyancy engines, but they could only move up and down without traveling in a 3D space. Besides, they lack the cooling mode just like other pneumatic actuators, relying solely on the natural convection for the vapor-liquid transition and slowing down the response time.^{73, 74}

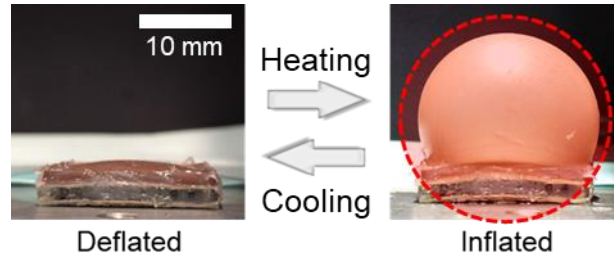


Figure 44 | Photographs of the reversible deflation and inflation of thermoelectric pneumatic actuator by liquid-vapor phase transition.

Owing to the TE device's bimodal modes to heat and cool as shown in **Figure 44**, the multiple uSTPAMs on the perimeter of the robotic fish body readily control localized buoyancy by inducing a rapid fluid phase-change and thereby facilitating its overall locomotion. Furthermore, the untethered platform embedded in the robotic fish enables self-powering of the uSTPAMs and wireless communication, which delivers instructions and transmits information from the embedded sensors on the robotic fish. Embedded pressure and gyro-sensors deliver real-time physical information such as water depth and spatial orientation of Flatfishbot, which can be useful to drive the robotic fish.

Moreover, based on the design optimizing simulation of the robotic fish framework, we mimicked the body structure of the olive flounder (*Paralichthys olivaceus*) to maximize hydrodynamic locomotive efficiency and make use of as greater torque with uSTPAMs during gliding. Despite the absence of dynamic mechanisms to generate thrust force unlike previous robotic fish works, Flatfishbot travels at the average speed of 0.515 body length per second, which is similar to or even faster than most of the previous fish robots, substantiating the highly effective mechanism of the intermittent gliding locomotion and creating a new category of underwater robotic locomotion with high efficiency. We showed that not only the soft robotic fish can imitate the intermittent locomotive gliding, but it can also make a turn to steer the direction, demonstrating that it can freely move in all three dimensions in the water by simply controlling localized buoyancy. Lastly, to further illustrate the practical applicability, we demonstrated that Flatfishbot can act as a miniature cargo-submarine that delivers the cargo underwater, and we also attached a water-proof camera to Flatfishbot for operation as an underwater spy drone or miniature inspection unit to convey valuable information about the underwater environment.

3.2. Underwater Soft Thermo-pneumatic Actuating Module

Overview

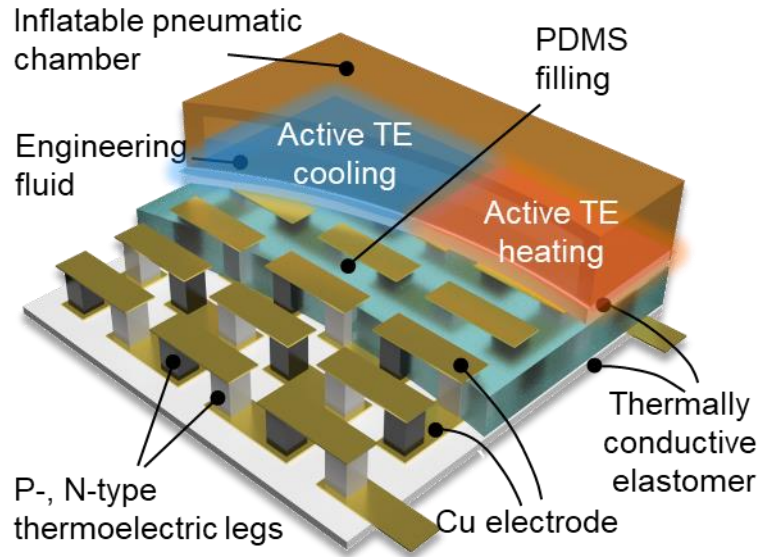


Figure 45 | Internal structure of the soft TPA unit that is comprised of a soft substrate, copper interconnecting film, thermoelectric legs, and elastic chamber.

Figure 45 shows the overall internal structure of the uSTPAM which consists of TE legs interconnected by the Cu electrode and an inflatable chamber that is filled with engineered fluid. BN micro-powder was incorporated into PDMS to improve the thermal conductivity of the elastomer so that it enhances the heat transfer between the thermoelectric device and the engineered fluid.

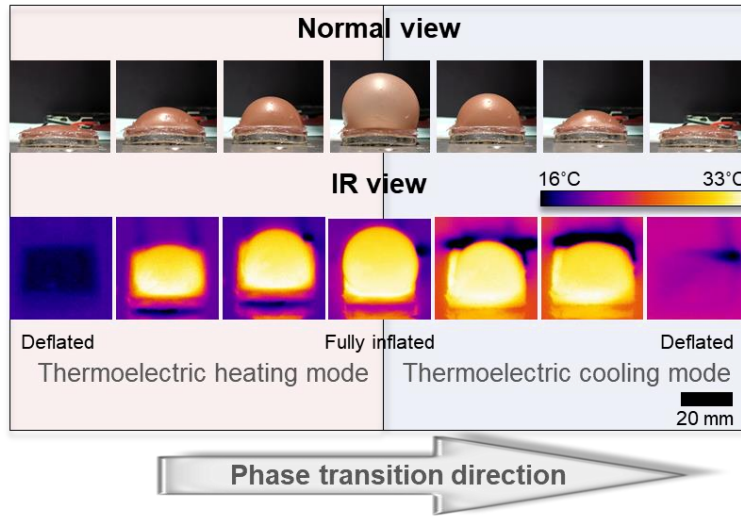


Figure 46 | Transient photographs and thermal imaging snapshots of the single TPA unit as it inflates and deflated by switching from the heating to cooling mode due to phase transition.

Taken with visible and infrared (IR) imaging cameras, **Figure 46** records transient moments of rapid inflation and deflation that a single uSTPAM module underwent in a unit cycle. We used 3M™ Novec™ 7000 engineering fluid with a boiling point of 34°C, slightly higher than room temperature. Thus, the chamber inflates if the TE device is in the heating mode to vaporize the engineering fluid and its overall buoyancy increases. The same applies to the cooling mode that induces the vapor-liquid transition and reduces buoyancy. The uSTPAM unit consists of minimal (28 mm x 28 mm x 5 mm), lightweight (6.9 g), and bi-modal hardware because the system does not require an external pump. Such characteristics fully satisfy the purpose of the research, because (i) it would be favorable to control buoyant force if the net buoyancy of the system is close to neutral buoyancy, and (ii) the capability of uSTPAM to heat and cool fulfills the shortcomings of the conventional thermal pneumatic actuators.

Characterizaion

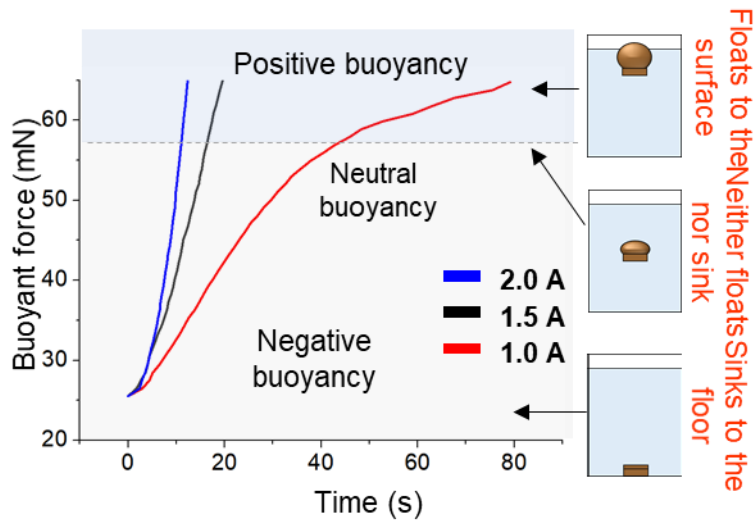


Figure 47 | Relationship between electrical current input into thermoelectric device and response time it takes to reach the neutral buoyancy.

The following thermodynamic process epitomizes the uSTPAM unit cycle of inflation and deflation. The active TE heating mode vaporizes the engineered fluid. It, therefore, leads to a swift rise in the volume of the chamber, which in turn increases buoyancy in a localized region of the underwater robot. The active TE cooling mode of uSTPAM, on the other hand, serves to condensate gas inside the chamber into a liquid, which corresponds to the deflation of uSTPAM. Besides, the rate of inflation, as well as deflation, can be fine-tuned as in **Figure 47** simply by controlling the magnitude and direction of the electrical current in the TE device.⁷⁵ Quite obviously, it indicated that the higher the electrical power is, the faster the uSTPAM module reaches and exceeds the neutral buoyancy. This implies that applying programmed electrical inputs on each uSTPAM unit would enable us to control the three-dimensional locomotion of Flatfishbot.

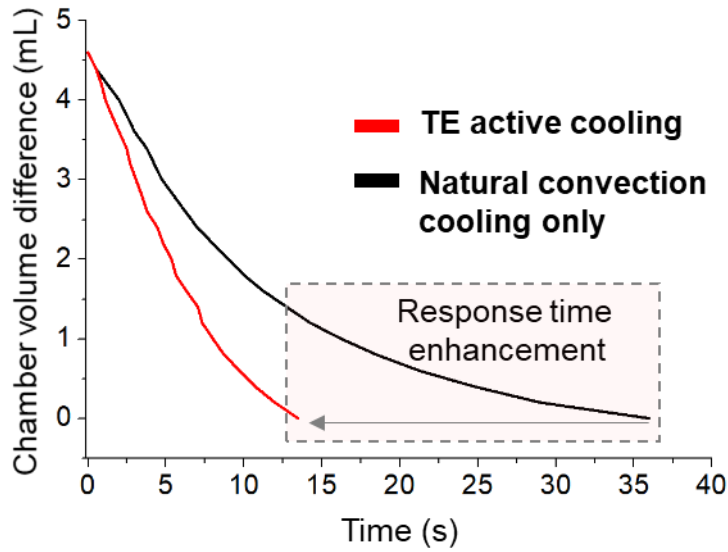


Figure 48 | Examining the difference between thermoelectric active cooling and natural convection to induce phase change from vapor to liquid and thus return to the original deflated state.

Furthermore, the thermal pneumatic actuators, despite desirable characteristics such as a pumpless and noise-free nature, suffer from a slow response rate because it relies solely on natural convection cooling for the fluid to return to the liquid state. Such a critical drawback of the thermal pneumatic actuator slows down the response time and hence increases the unintended locomotive error of the soft robots. However, the TE device can directly address the issue of the thermal pneumatic actuators, because it can interchangeably heat/cool with the single device structure depending on the direction of the electrical current.⁷⁵ Therefore, after the complete inflation of the chamber, the TE device can switch to the cooling mode to quickly deflate the chamber. **Figure 48** delineates a direct comparison between the TE cooling and natural convection to induce the phase change back to the liquid state by measuring the transient volume difference of the pneumatic chamber with both devices submerged into water. The result suggests that the TE cooling substantially accelerated the chamber deflating process by approximately 2.67 times faster than natural convection, further implying that incorporation of the TE device into the underwater robotic design architecture would shorten the response time and allow more accurate control of the final prototype.

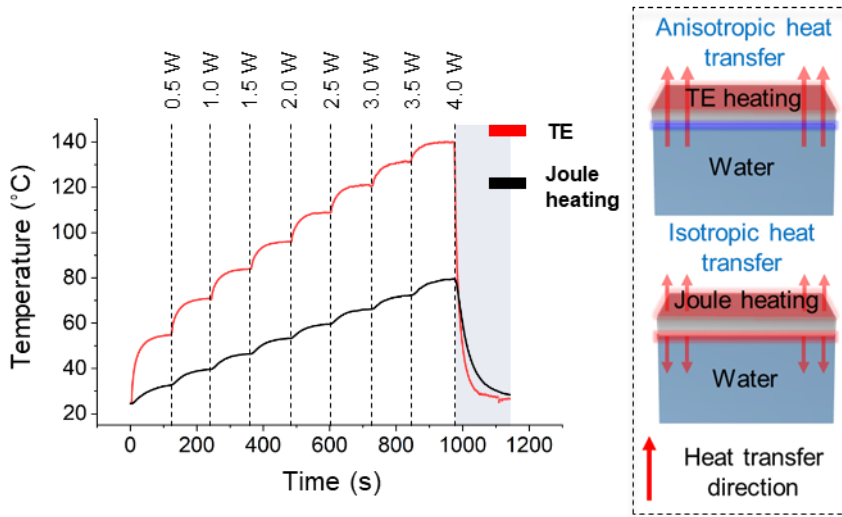


Figure 49 | Comparison between thermoelectric and Joule heating performance by applying the identical amount of electrical power. The inset figures describe the heat transfer direction during thermoelectric and Joule heating modes. The large discrepancy of the performances originates from the isotropic heat flow of the Joule heater in which an enormous amount of heat is dissipated into the underwater reservoir.

TE heat transfer in the particular underwater application also exhibits higher thermal efficiency than conventional Joule heater. We selected Joule heating as a counterpart to be compared because it is widely used to induce the liquid-vapor transition in many previous thermal pneumatic actuators.^{12, 13, 76-78} **Figure 49** compares the heating performance between the TE device and the Joule heater by applying the identical magnitude of electrical power while recording the surface temperature of both devices with the IR camera. The result indicates that the TE heating generates more than twice the higher temperature than Joule heating, and the primary reason for such a large discrepancy lies in how the heat transfer occurs in the two thermal models. For the Joule heating case, heat transfer occurs in an isotropic way, so a considerable proportion of heat dissipates into the water, which works as a semi-infinite thermal reservoir. This implies that not all heat generated by Joule heating would be used to contribute to inducing the fluidic phase change. In the TE heat transfer, on the other hand, a heat differential is formed in the cross-plane direction of the device, indicating that the heat is transferred in a highly anisotropic manner because the opposite side of the device would cool down when the heating mode is switched on to inflate the chamber. Thus, instead of dissipating a substantial amount of heat into the water reservoir, the anisotropic heat transfer of the TE device promotes the heat flow from the water to the device and further to the engineered fluid inside the chamber. Such a heat flow,

as is illustrated in the inset of **Figure 49**, explains the reason for the huge difference in thermal efficiency between two thermal devices.

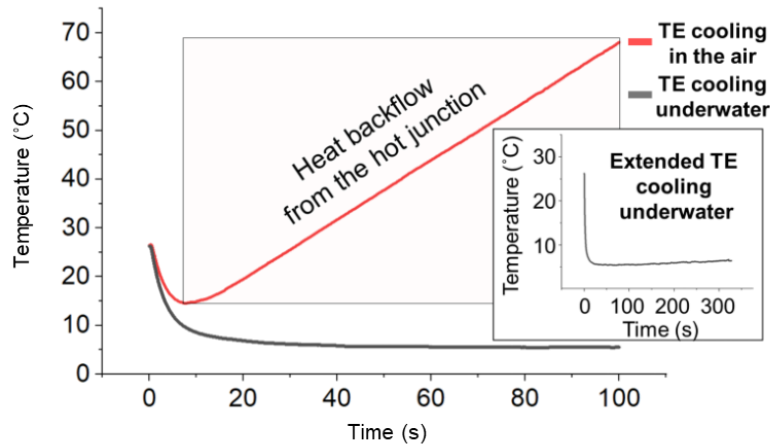


Figure 50 | Thermoelectric cooling performance difference between operating in the air and underwater. The cooling difference arises from the thermal conductivity of air and water, in which water functions as an effective heatsink to absorb heat energy from the opposite heating side of the thermoelectric device whereas air cannot be due to its thermal properties. The inset figure demonstrates the thermoelectric cooling performance at the same thermal condition for the extended time period

Moreover, the conventional TE system must include an additional heatsink to absorb heat generated on the other heated side of the TE device when it is supposed to cool the arbitrary subject. The absence of the heatsink on the TE system usually causes severe deterioration of the TE cooling performance, which even results in the temperature surge much higher than room temperature even if the original intention were to cool. Yet, operating the TE device in the underwater environment directly settles down this issue, because water possesses a much higher heat transfer coefficient than air ($h_{Hx\ water} \approx 0.01\ W\ cm^{-2}\ K$, $h_{Hx\ air} \approx 0.0005\ W\ cm^{-2}\ K$).⁷⁹ **Figure 50** substantiates that water can function as a natural heatsink under the cooling mode of the soft TE device in this work. Thus, the TE device that operates in the water exhibits a stable cooling mode ($T_{cooling} = 5^{\circ}C$) for an extended period of time, whereas the temperature of the TE device without the heatsink shoots up to $70^{\circ}C$ within 100 s after the cooling mode has been turned on, highlighting the advantage of operating the TE device underwater.

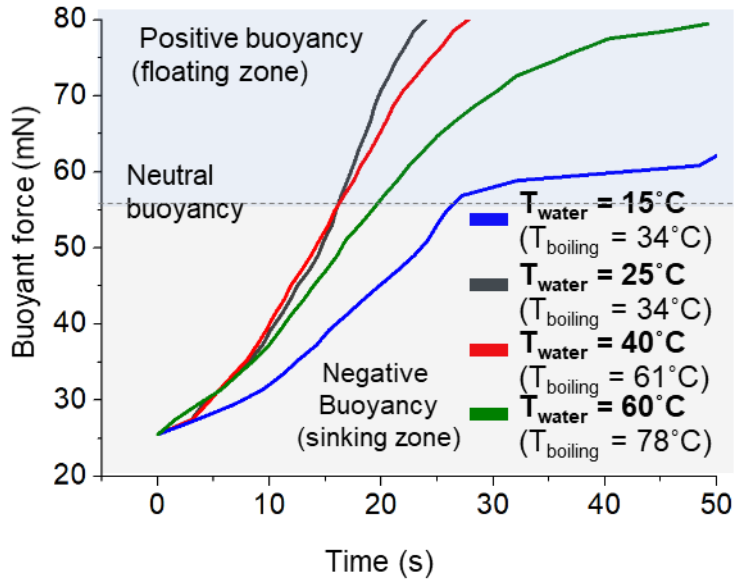


Figure 51 | Response rate to reach the neutral buoyancy and start floating at different surrounding water temperatures. Please note that fluids inside the chamber have different boiling temperatures to enhance response time.

Besides, it is often the case that, depending on the latitude, the ocean temperature varies in real-world applications, which might slow down the response time of uSTPAM or even cause malfunctioning of the entire robotic system if the phase change temperature deviates much from the surrounding water temperature. For instance, uSTPAM that contains the fluid with a boiling point of 30 °C would stay inflated if the water temperature is higher than its boiling point. On the other hand, the substantially lower water temperature would slow down the response time of uSTPAM, because it would consume more time to heat the fluid all the way up to the boiling temperature. **Figure 51** resolves the issue by practically matching the boiling points of the fluids to that of the surrounding water. To validate such an effect, we artificially set the arbitrary water temperatures at 15 °C, 25 °C, 45 °C, and 60 °C, and utilized several fluids (3M Engineered fluid 7000, 3M Engineered fluid 7100, and ethanol) that have boiling points of 34 °C, 61 °C, and 78 °C respectively. The result shows that all uSTPAMs except the sample at $T_{\text{water}}=15$ °C with different thermal conditions approached the neutral buoyancy within 16 s and started to float up to the surface right away. The sample at $T_{\text{water}}=15$ °C approached the neutral buoyancy slightly later than samples at other thermal conditions, but it still floated up within 26 s, demonstrating that the design architecture of uSTPAM is highly adaptable to various thermodynamic conditions and operates regardless of the surrounding water temperature in real-world applications.

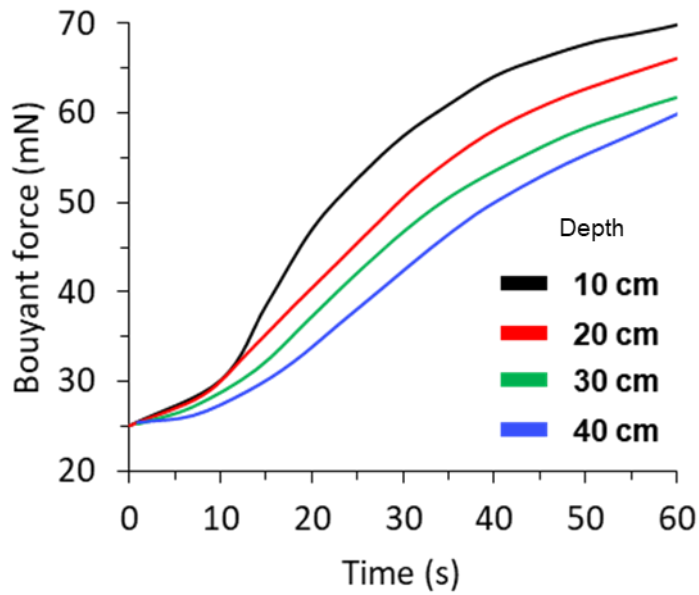
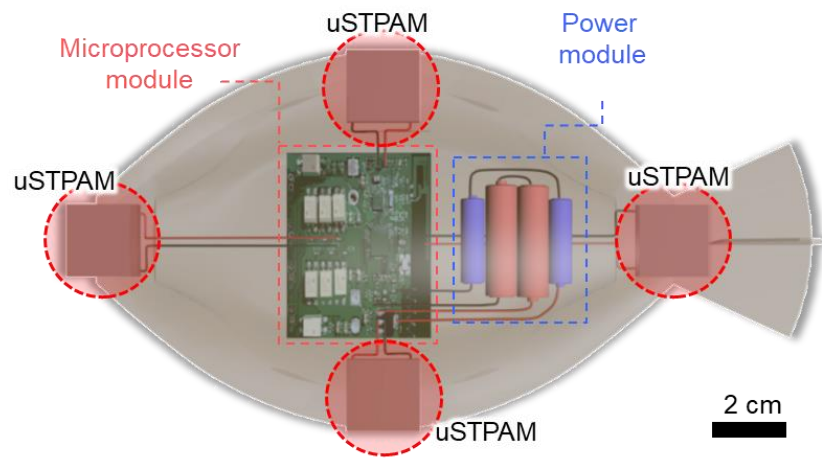


Figure 52 | Relationship between depth underwater and response time of uSTPAM.

Figure 52 shows the relationship between the buoyant force and water depth of a single TPA unit. It suggests that the deeper the water depth gets, the smaller the TPA generates with identical electrical input. The reason is that water exerts counteractive pressure against the TPA, and water pressure heightens as the water depth increases.

3.3. Flatfishbot

Overview



Underwater Soft Thermo-pneumatic actuator (uSTPAM)

Figure 53 | Graphical illustration of Flatfishbot integrated with its functional components

Figure 53 graphically illustrates the functional components (uSTPAMs, printed circuit board, and battery module) and simple architecture of the soft robotic fish that mimics the body shape of the olive flounder for efficient hydrodynamic locomotion. Four inflatable uSTPAMs are added to the front, rear, and sides of the robotic fish to manipulate the localized buoyancy for fine-tuning the spatial orientation and net buoyant force of the soft robotic fish.

Mechanics for Flatfishbot's locomotion

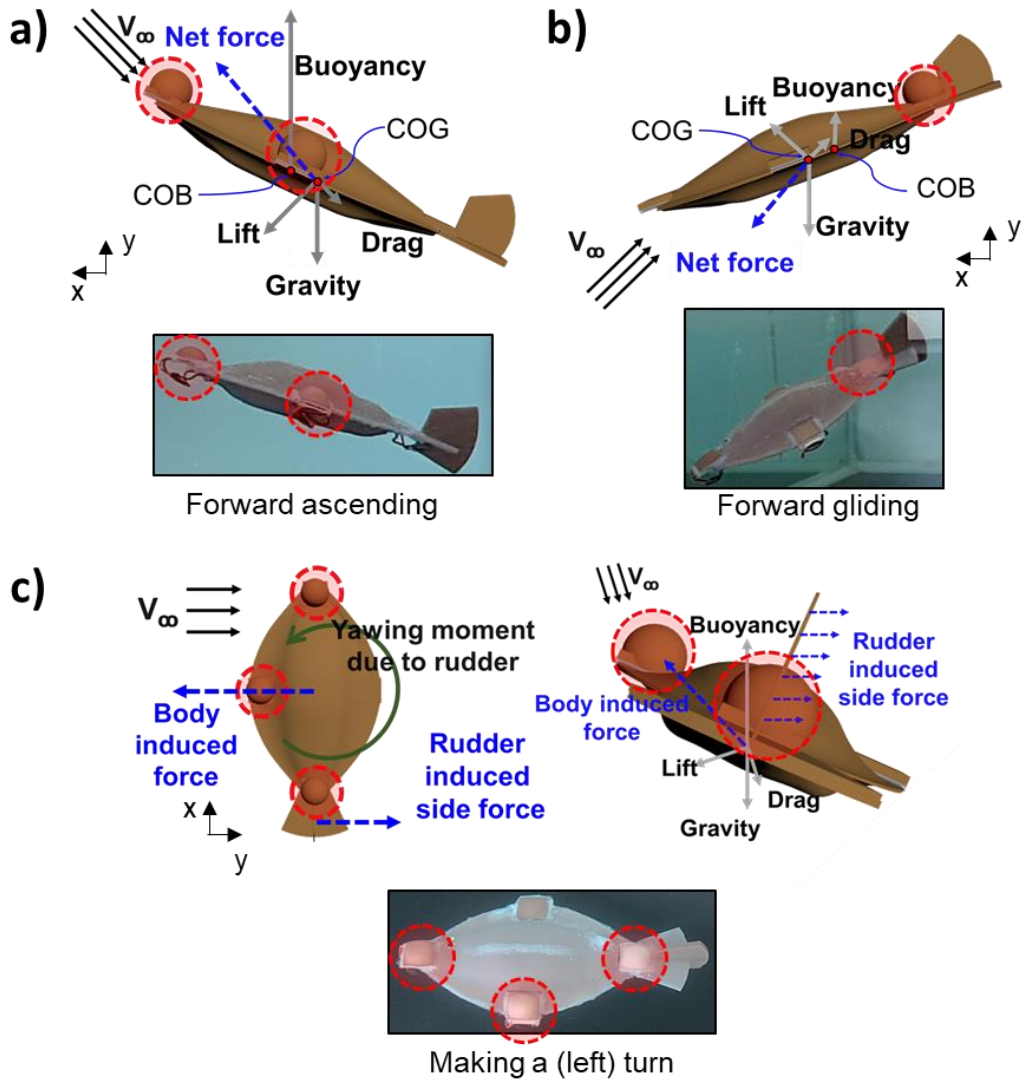


Figure 54 | Free-body diagram of the forward ascending, forward gliding and turning modes of the Flatfishbot. a) Forward ascending. b) Forward gliding. c) Making a (left) turn.

Figure 54 presents the two-dimensional free-body diagram of the cross-sectional Flatfishbot that consists of all applied forces on the system during forward ascending (**Figure 54a**), forward gliding (**Figure 54b**), and making a turn (**Figure 54c**), explaining the basic locomotive mechanics of soft robotic fish. Lift force, which is induced when the external fluids (V_∞) exert a force on the surface of the robotic fish at motion, mainly participates in the dynamic forward movement both during ascending and gliding. In the case of the forward ascending motion, the rapid TE heating mode vaporizes the engineered fluid inside the chamber and shifts the center of buoyancy (COB) toward the inflated

uSTPAMs, which creates the tilted orientation of the robotic fish. Then, as the net buoyancy of the entire robotic system becomes positive, Flatfishbot starts to float and produces a lift force that is perpendicular to the moving direction, generating +x component force in the x-axis and therefore inducing the forward movement as it ascends to the surface. When Flatfishbot glides downward, on the other hand, the front and side uSTPAMs switch to the cooling mode, and the rear uSTPAM is quickly heated with active TE heating, making the soft robot face toward the bottom. Similarly, the net negative buoyancy causes Flatfishbot to sink. But, a certain proportion of lift produces force in +x-direction as it moves down, therefore contributing to the forward movement in the course of its gliding motion. Notably, the tilted orientation of the robotic fish plays an essential role in generating forward motion both when it goes up and down because it determines the direction of the lift force.

Apart from the forward movement, the underwater robot developed herein can change the direction by utilizing the same uSTPAM mechanism. (i) Two uSTPAMs (on the side of the robotic system) and (ii) the vertical rudder on the tail plays a crucial role in conjunction to make a turn as in the graphical image of **Figure 54c**. Please note that activating one of two side uSTPAMs (a left chamber, for instance) creates a difference in buoyancy and therefore tilts its orientation in a roll axis (tilts toward the right chamber, for example). Yet, without the rudder, simply inflating a single uSTPAM on the side does not enable the robotic fish to make a turn: it rather follows a diagonal path across the fish tank. On the contrary, the vertical plane of the rudder creates a side force in the y-axis direction and generates a moment around the yaw axis. This way, the robotic fish can switch its direction depending on which side uSTPAM to activate, thus indicating that it can explore the underwater environment in all three spatial dimensions. We are fully aware that the olive flounder does not have a rudder-like structure to make a turn. The primary focus of this research was to develop a soft robotic fish based on biological inspirations from marine animals, not to replicate the complete anatomy of the marine animal. Therefore, we intentionally incorporated the vertical rudder structure into the design of the soft robotic fish for the additional locomotive functionality so that it can freely make a turn without resorting to other propulsive mechanisms such as mechanical pumps or motors.

Outer shell design

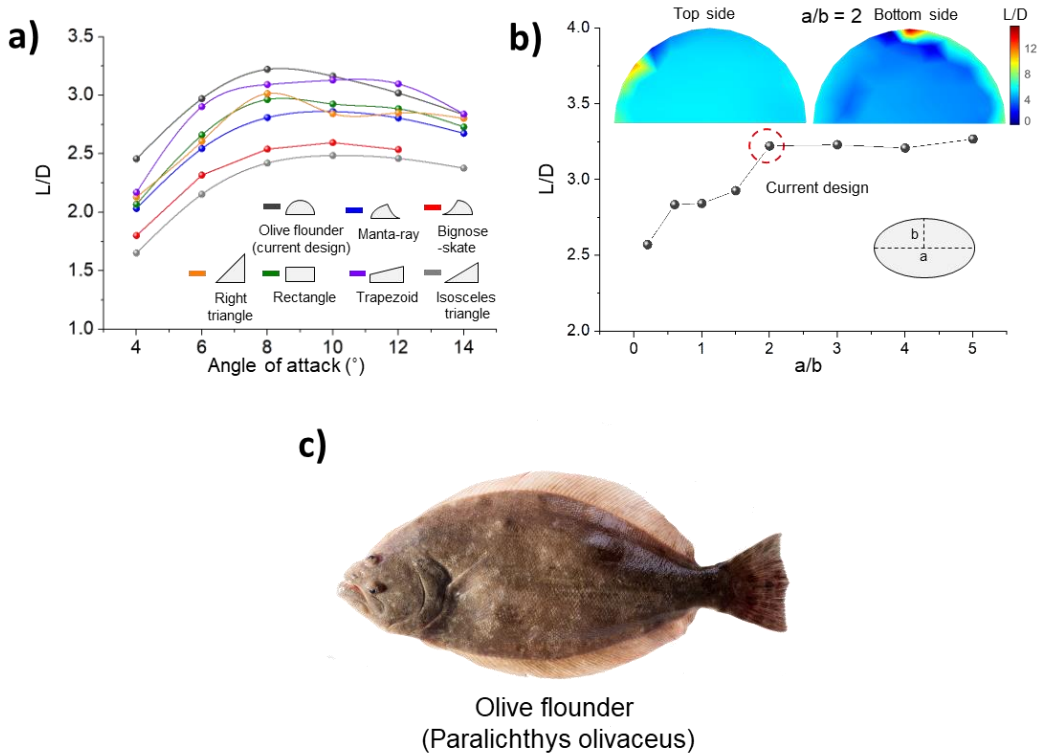


Figure 55 | Design consideration. a) Designing of the soft robotic fish architecture by comparing numerically computed lift/drag ratio in a function of angle of attack b) Design optimization by examining lift/drag values with varying a/b ratio. c) Actual photograph of olive flounder. The photograph of olive flounder was obtained and reproduced under permission of Irina K.

To enhance the hydrodynamic efficiency of the robotic fish during its locomotion, we conducted a numerical simulation to compare several soft-shell designs as in **Figure 55a-b**, since the external structure would significantly affect the lift and drag forces. To make greater use of localized buoyancy for controlling the spatial configuration of the robotic fish, we only considered relatively flat designs for the outer elastomeric shell of the robotic fish because the further away uSTPAMs are from each other, the greater magnitude of torque they would create in the presence of localized buoyancy difference among uSTPAMs. Hence, as **Figure 55a**, along with the common geometric models such as triangle (isosceles, right), trapezoid, and rectangle, we also tested the shapes that mimic those of flatfish species in nature, such as flounder and ray-fish because their exteriors would have been likely to be evolved in a way that hydrodynamically enhances their swimming effectiveness over time. Since the higher lift-drag (L/D) ratio usually results in efficient locomotion, L/D was numerically computed as a function of the angle of attack based on the assumption that water flows at a velocity of $0.2 \text{ m}\cdot\text{s}^{-1}$ against the subjects. The

result shows that the geometrical framework of the flounder exhibits the highest L/D value of 3.22, and the angle of attack between 6° and 14° yield the high L/D values, suggesting that the initial orientation of Flatfishbot during forward ascending and gliding must follow the obtained angle of attack to boost its swimming efficiency. To further optimize the outer soft-shell geometry, we calculated L/D with varying a/b ratios, and the result implied that L/D begins to plateau at the range of $a/b > 2$ (**Figure 55b**). We set the $a/b = 2$ as the optimal design because larger a/b values would unnecessarily enlarge the size of robotic fish and make it less likely to swim into the small cavities in actual strategic applications. Therefore, we applied the optimized design to the robotic fish's soft outer shell, which resembles the olive flounder as in **Figure 55c**.

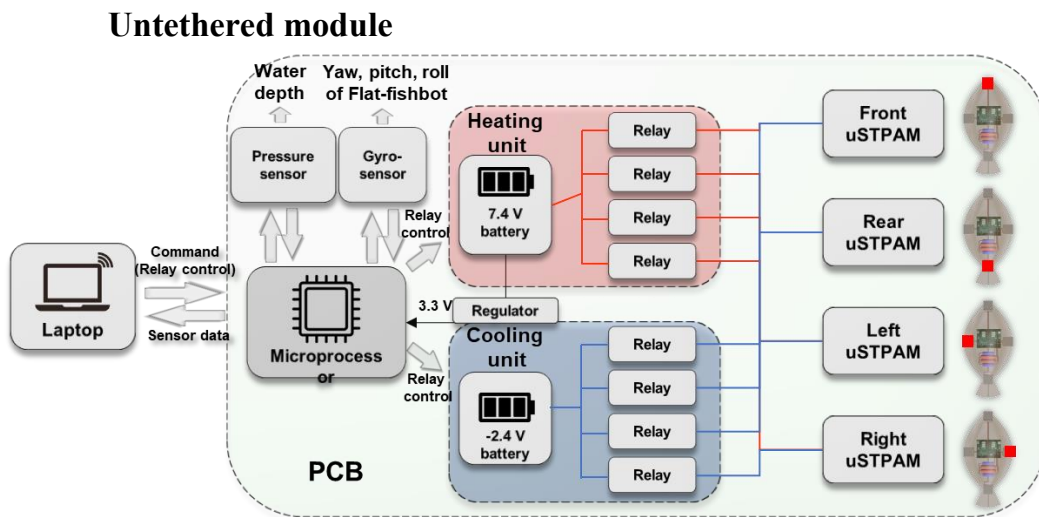


Figure 56 | Wireless flowchart of Flatfishbot by which the command inputs to the uSTPAM units of the robotic fish are delivered, and physical spatial data of the robotic fish from pressure and gyro-sensors is transmitted

Furthermore, we implemented the wireless module with multiple sensors to further develop Flatfishbot into a fully untethered robotic unit. However, tethered robotic systems suffer from several limitations that hurt the functionalities of the robotic fish, especially for underwater applications. Primarily, the tethered robots can travel only within the designated distance because it is wired to the rigid power source through the electric cable. Besides, tethering might exert tension force on the robots with relatively small mass and thus might affect their overall locomotion inside water. Lastly, supplying power through an electric cable poses a danger to the aquatic ecosystem and might harm the aquatic organisms.

In this regard, to develop the untethered platform for uSTPAMs and the overall system, we designed the board circuit that consists of (i) a microcontroller unit, (ii) a

heating/cooling relay for each bimodal uSTPAM unit, (iii) a sensor module, (iv) an antenna for wireless communication, and (v) battery modules with the flow chart in **Figure 56**. To interchangeably switch between the cooling and heating modes in the course of motion, we used relays to alternate between inflation and deflation of uSTPAMs.

Furthermore, the embedded sensor module, which consists of pressure and gyro-sensor units, performs the essential task to provide the real-time spatial information of Flatfishbot for human users to pilot the soft underwater robot. The pressure sensor unit delivers data on the water depth at which Flatfishbot is situated at the moment, and it must be noted that the soft body of Flatfishbot enables pressure sensing from the interior of the soft robot because the volume of Flatfishbot changes simultaneously, according to the water depth. Such a system allows facile pressure sensing and even prevents the sensor unit from being damaged by external force because it is situated inside the underwater robot. On the other hand, pressure sensing from the interior of the robot cannot be easily realized on the underwater robot based on rigid materials. It reflects the advantage of soft robotics in the underwater environment. The gyro-sensor also conveys meaningful information on the three-dimensional orientation of the robotic fish, such as roll, pitch, and yaw, since its orientation determines the direction of the lift force. Hence, the wirelessly transmitted information on its orientation can then be applied to adjust its position for a desirable angle of attack as it moves forward.

To power the uSTPAMs and microcontroller, we used two separate battery modules for constant heating and cooling modes: a 7.4 V 2500 mAh LiPo battery for the heating mode (and powering the microcontroller via the 3.3 V regulator) and a couple of 1.2 V 2000 mAh NiMH batteries connected in series for the cooling mode. It is calculated that a single charge would power Flatfishbot for 60 minutes (equivalent to 36 cycles of continuous forward ascending and gliding alternation) owing to the relatively economical locomotion mechanics of Flatfishbot.

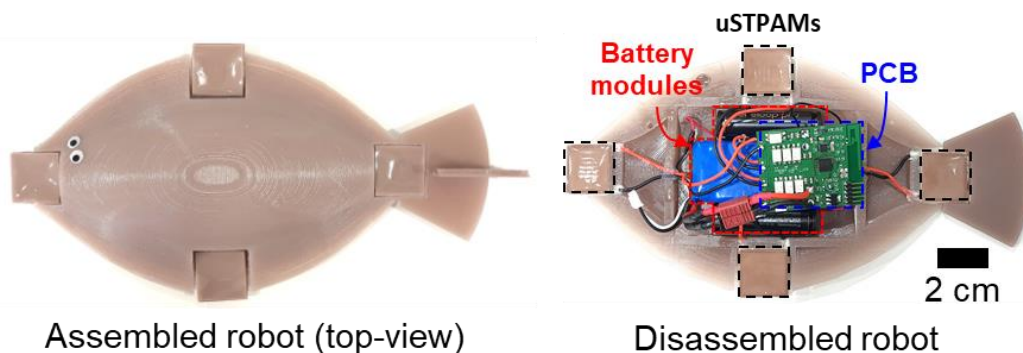


Figure 57 | Flatfishbot. a) Photographs of Assembled/disassembled Flatfishbot. b) Top view of Flatfishbot integrated with its functional components

Lastly, we integrated all the components into the soft outer shell fabricated by thermally cross-linking elastomer and commercial brown-color dye inside the 3D printed polylactic acid (PLA) mold as in **Figure 57**. The outer framework of the soft robotic fish to integrate all the functional components was made by curing Dragon Skin 10 on 3D printed PLA molds at room temperature (because the heat treatment thermally deforms the PLA molds) with a small addition of brown Silc Pig dye into the Ecoflex 00-35 to mimic the actual color of olive flounder.

Demonstration

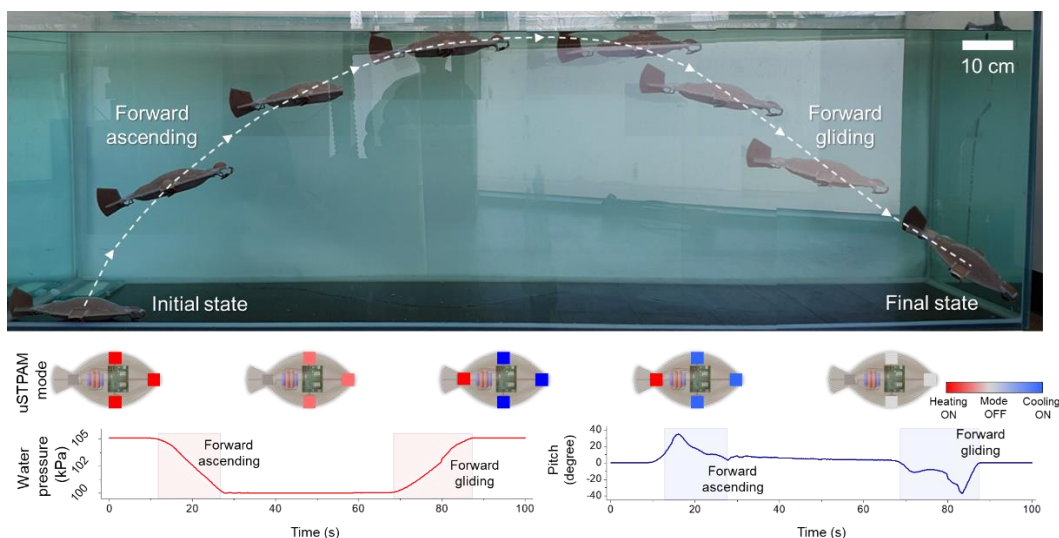


Figure 58 | Snapshots of the moving path that Flatfishbot went through to simulate the forward gliding locomotion of the marine vertebrates and corresponding pressure, gyro data during the locomotion.

With the fully assembled prototype based on the previous design factors, we demonstrated the forward movement of Flatfishbot while wirelessly delivering commands for uSTPAMs and collecting data of Flatfishbot in the fish tank with a dimension of 70 mm (width) x 200 mm (length) x 80 mm (height). **Figure 58** demonstrates that Flatfishbot moves forward by drawing a sinusoidal trajectory as it ascends and glides. Flatfishbot faces upward when the front and side uSTPAM heat the fluid inside the chambers to fully inflate, and Flatfishbot ascends forward as the side uSTPAMs start to inflate. As Flatfishbot hits the water surface, the front and side uSTPAMs quickly switch to the cooling mode to deflate while the rear uSTPAM fully inflates the chamber, which serves to tilt the orientation of Flatfishbot downward. Then, Flatfishbot glides down as the front and side uSTPAMs fully deflate. The entire cycle repeats as the rear uSTPAM deflates. Flatfishbot travels at the average velocity of $10.3 \text{ cm}\cdot\text{s}^{-1}$, equivalent to 0.515 body length per second. Simply using

the gliding locomotion by controlling localized buoyancy, Flatfishbot exhibited comparable or even faster velocity than other underwater soft robots that utilize auxiliary components for generating a thrust force such as servo-motors, pneumatic pumps, dielectric elastomer, and shape memory alloy to mimic the propulsive mechanism of aquatic animal. (See Table 3). Besides, graphs below the series of Flatfishbot snapshots exhibit corresponding sets of real-time data collected by the pressure and gyro sensors, which were in turn used to pilot the locomotion of Flatfishbot. We expect that incorporating thrust components such as a servo-motor that produces a thrust force would boost the performance of the robotic fish by far. Nevertheless, we believe that the addition of such components would dilute the original focus of our work, which is to mimic the efficient locomotion behavior to drive the robotic fish in three-dimensional space in the underwater environment without any conventional unit. We plan to incorporate such components into the current system for future work so that it can hopefully exceed the swimming speed of other underwater robots.

Table 3 | Comparison with previous studies for robotic fishes

Reference	Capable of mimicking the gliding locomotion	Material	Mimicking subject	Swimming mode	Capable of swimming 3D trajectory	Propulsive mechanism	Wireless communication	Tethered	Speed (body length per second)
Flatfishbot (this work)	O	Soft	Marine vertebrates	gliding	Yes	Controlling localized buoyancy	Yes	Untethered	0.515
46	X	Soft	Manta ray	MPA-U	No	Dielectric elastomer actuator	No	Untethered	0.69
47	X	Soft	Typical fish	BCA-O	No	Pneumatic pump	Yes	Untethered	0.026
48	X	Soft/rigid	Typical fish	BCA-O	Yes	Pneumatic pump	Yes	Untethered	0.5
49	X	Soft/rigid	Tuna	BCA-O	No	Motor	No	Tethered	4
34	X	Soft	Typical fish	BCA-O	No	Dielectric elastomer actuator	No	Tethered	0.25
50	X	Soft	Manta ray	MPA-U	No	Shape memory alloy	No	Tethered	0.26
51	X	Soft	Snailfish	MPA-U	No	Dielectric elastomer actuator	No	Untethered	0.45
60	X	Rigid	Typical fish	BCA-O	No	Servo motor	Yes	Untethered	0.63
61	X	Soft/rigid	Manta ray	MPA-U	No	Dielectric elastomer actuator	Yes	Untethered	0.053
62	X	Rigid	Typical fish	BCA-O	No	Dielectric elastomer actuator	No	Tethered	0.228
63	X	Soft/rigid	Typical fish	BCA-O	No	Shape memory alloy	No	Tethered	0.77

64	X	Soft	Leptocephalus (EelLarva)	BCA-U	No	Fluid electrode actuator	No	Tethered	0.009
66	X	Soft	Jellyfish	Propulsion	Yes	Dielectric elastomer actuator	No	Untethered	0.02
67	X	Rigid	Scallop	Propulsion	No	Fluid electrode actuator	No	Tethered	2
68	X	Soft/rigid	Octopus	Crawling	No	Motor-Driven Cables/SMA	No	Tethered	0.05
65	X	Rigid	Snake	BCA-U	No	Servo motor	No	Tethered	0.014
69	X	Rigid	Turtle	Oscillation	No	Shape memory alloy	Yes	Untethered	0.092
70	X	Rigid	Starfish	MPA	No	Shape memory alloy	No	Tethered	0.35
71	X	Rigid	Legs inspired	Oscillation	No	Dielectric elastomer actuator	No	Tethered	0.77

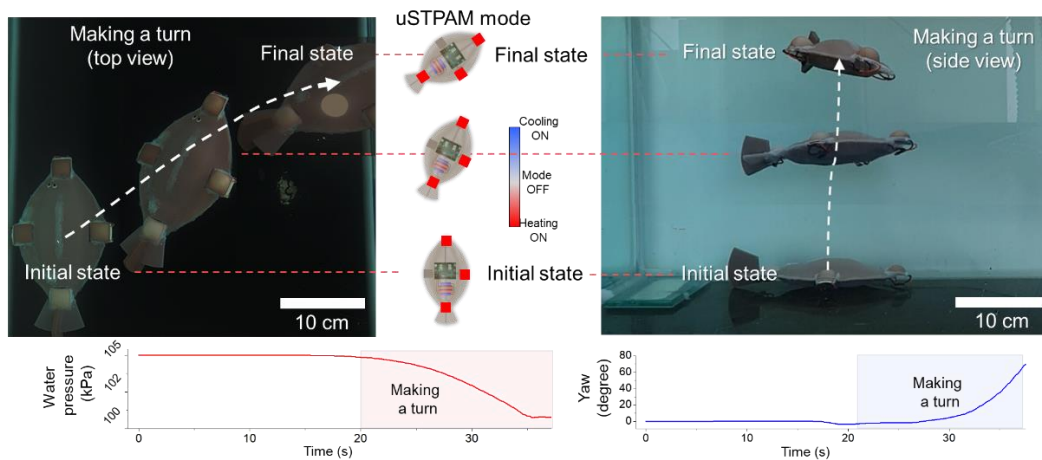


Figure 59 | Flatfishbot demonstration of changing direction to make a turn (top- and side-view) and corresponding sensor data.

Figure 59, on the other hand, demonstrates that the underwater robot can also make a turn to steer the direction of progress, owing to the side uSTPAMs and a rudder structure as they collectively produce the side force, which is translated into torque and makes the underwater robot rotate about the z-axis around its center of mass (COM). As can be seen from the yaw value in **Figure 59**, it rotates by 70° in a clockwise direction until it hits the glass wall of the fish tank. We believe that the soft robotic fish can rotate further and even make a full U-turn with a bigger tank.

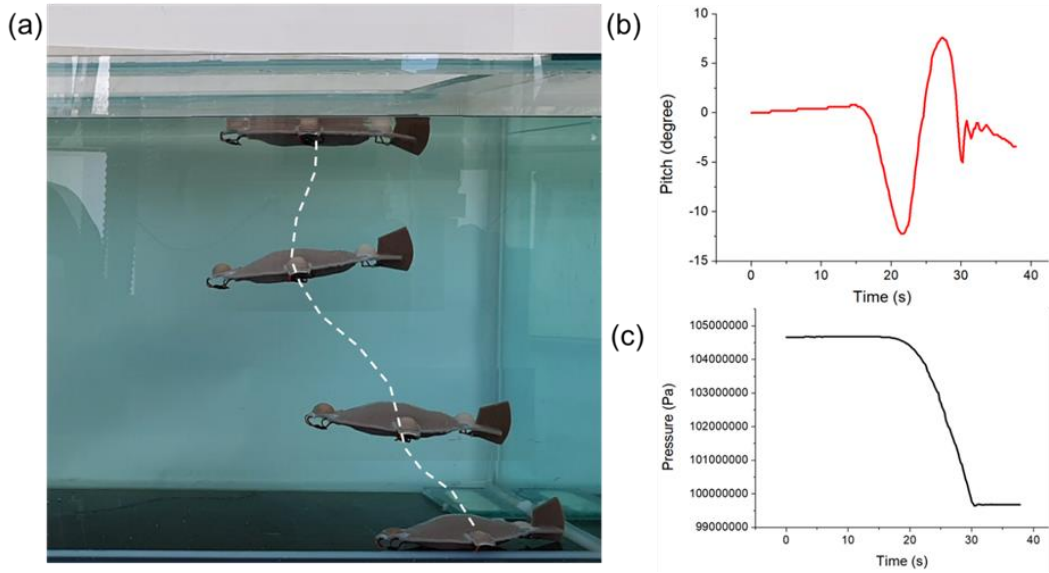


Figure 60 | Vertically rising locomotion of Flatfishbot. (a) Snapshots of Flatfishbot moving up by turning all uSTPAM units. (b) Transient pitch and (b) water pressure values as the soft robotic fish moves up to the water surface

Similarly, turning uSTPAMs on and off all at once make Flatfishbot move only in the vertical direction as in **Figure 60**. Please note that we could control the spatial orientation of the robotic fish when it moved up by activating all uSTPAMs. At first, the pitch values turned slightly negative as it ascended vertically to the water surface because inflating rate differed between the front and rear uSTPAM. Then, we increased the electrical input value of the rear uSTPAM to balance the orientation of Flatfishbot, as shown in the transient pitch graph (**Figure 60b**).

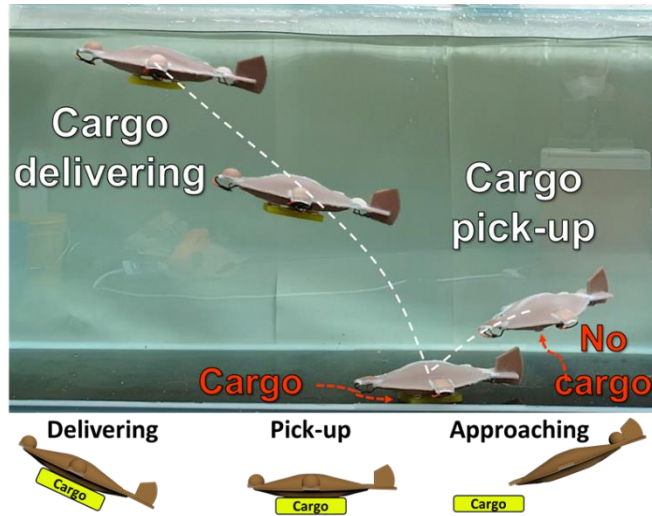


Figure 61 | Flatfishbot is capable of picking up and delivering a cargo as a submersible miniaturized cargo ship.

Capable of moving forward, vertically, and making a turn, the Flatfishbot is expected to travel in all three dimensions inside the water freely. For example, Flatfishbot can also operate as a miniaturized submersible cargo-submarine since it can generate buoyant force that is large enough to load the additional object. **Figure 61** shows a series of scenarios in which (i) Flatfishbot approaches the dyed elastomer block, (ii) makes magnetic contact, and (iii) carries the elastomer block to the destination. We adhered the magnets both on the abdomen of Flatfishbot and the elastomer block so that the elastomer block does not fall off the robotic fish in the course of the journey (the dimension and mass of the elastomer block were 77 mm x 86 mm x 11 mm and 70g, respectively). Flatfishbot does not travel as far as it can move without the cargo because the cargo itself increases the overall weight of robotic fish and affects drag force. Still, the demonstration corroborated the practical usage of Flatfishbot as a miniaturized cargo-submarine.

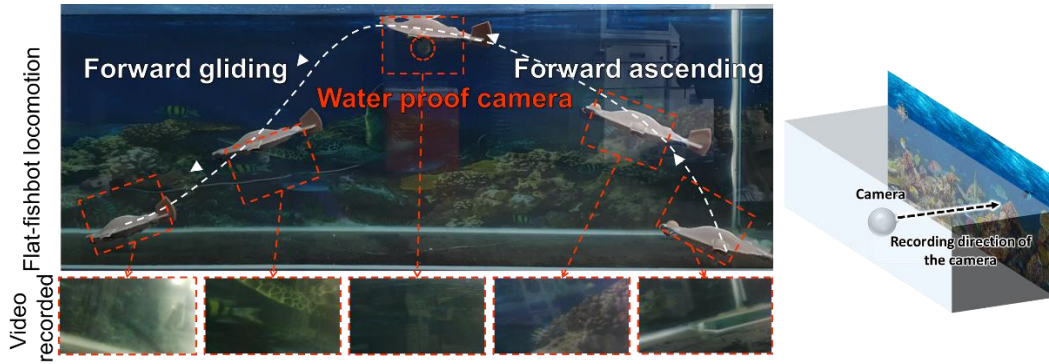


Figure 62 | Photographed moving route of the water-proof camera-attached Flatfishbot and corresponding recorded video snapshots during the locomotion to examine its potential to operate as an underwater inspection robot. The experimental setup and recording direction of the water-proof camera.

Furthermore, to demonstrate that the identical structure can be adapted to an underwater spy drone, we attached the commercial waterproof camera (the total camera mass of 31g) to Flatfishbot with the camera facing toward its right so that it can record the ex-situ video during the course of its journey. This way, Flatfishbot can act as an aquatic exploration or spy drone and thus be deployed to record a video to inspect the underwater environment as **Figure 62**. It is expected that Flatfishbot is especially appropriate for such an application since it does not generate noise, unlike bulky motors or engines that usually would propagate undesirable vibration inside water and agitate marine animals. In this regard, future work will include formulating a collective swarm of multiple Flatfishbots wirelessly connected to exchange information due to a simple and scalable fabrication process to manufacture a single unit of Flatfishbot such that a swarming unit can inspect a much wider space and perhaps open up possibilities for more strategic actions.

However, one of the significant limitations of wireless control originates from its short communication range, as electromagnetic properties of water inhibit its propagation and induce critical attenuation.⁸⁰ Future work will replace the current Bluetooth wireless communications with the acoustic communication platform for a long-range application as the previous literature demonstrated that the acoustic communication is capable of communicating within hundreds of kilometers.⁸¹

Simulation for Flatfishbot's locomotion

In the previous figure in the manuscript (p. 57, **Mechanics for Flatfishbot's locomotion, Figure 54**), we assumed that lift, gravity, and drag all apply force at the same point, center of gravity (COG), in the fish robot for simplification.

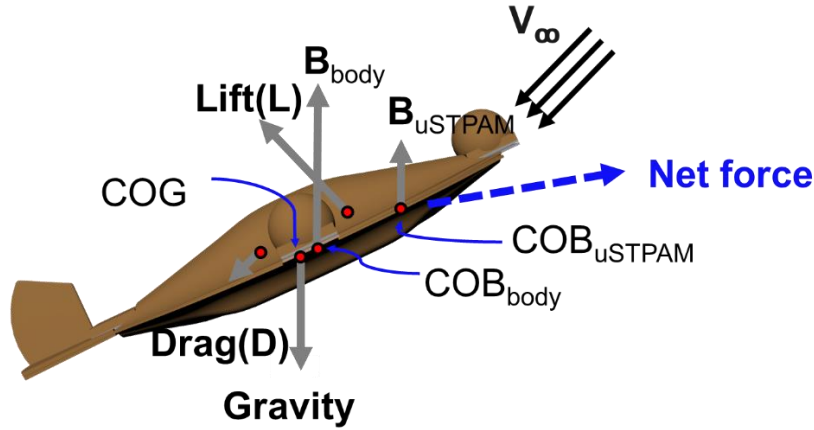


Figure 63 | Modified free-body diagram of Flatfishbot

However, to analyze and compare simulated data and recorded real locomotion data of Flatfishbot, we should consider the COG, center of lift (COL), and center of drag (COD) as in **Figure 63** because it would allow us to calculate the moment of the robotic fish, and this would provide us with additional ordinary differential equations along to solve. Also, it is essential to consider moments in this work because the spatial orientation of the robotic fish plays a primary role in its locomotion as it is used to move forward and steer direction.

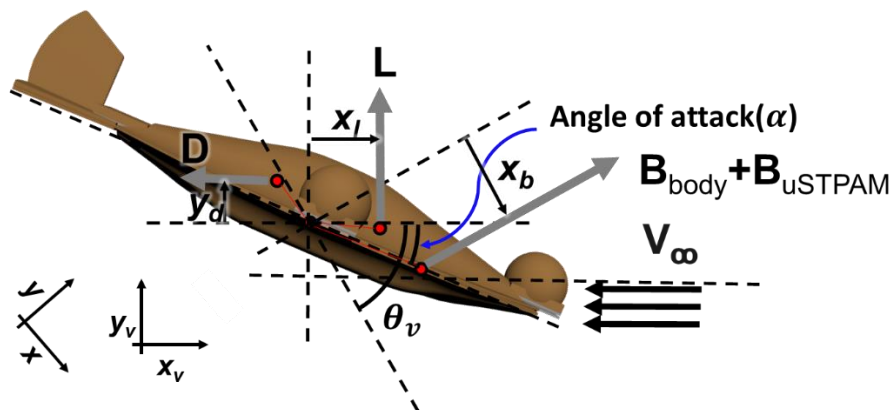


Figure 64 | Free-body diagram for moment calculation of Flatfishbot in the coordinate based on the external flow

Using the detailed free-body diagrams in **Figure 64**, we can derive the following equations,

$$m \frac{d^2 x}{dt^2} = F_x = -L \cdot \sin(\theta_v) - D \cdot \sin(\theta_v)$$

$$m \frac{d^2 y}{dt^2} = F_y = L \cdot \cos(\theta_v) - D \cdot \sin(\theta_v) + B_{body} + B_{uSTPAM} - mg$$

$$M = L \cdot x_l + D \cdot y_d + (B_{uSTPAM} + B_{body}) \cdot x_b \cos(\theta_v + \alpha) = I d(\theta_v + \alpha)/dt$$

x -axis: horizontal axis of the global coordinate

y -axis: vertical axis of the global coordinate

t : time

F_x : the net force applied to the Flatfishbot

L : lift force

D : drag force

x_v, y_v : x, y -axis of the coordinate based on the external flow

θ_v : angle of the external flow

B_{body} : buoyancy of the Flatfishbot body

B_{uSTPAM} : buoyancy generated by uSTPAMs

m : mass of the Flatfishbot

g : gravitational constant

M : net moment applied to the Flatfishbot

x_l : perpendicular distance from COG to COL based on the direction of the lift force

y_d : perpendicular distance from COG to COD based on the direction of the drag force

x_b : perpendicular distance from COG to COB based on the direction of the buoyancy

α : angle of attack

I : rotational inertia of Flatfishbot

and we assumed that $\frac{dM}{dt} = I d^2(\theta_v + \alpha)/dt^2 \approx 0$ with a constant value of $m = 0.478 \text{ kg}$, $B_{body} = 4.74798 \text{ N}$, and $(B_{uSTPAM} + B_{body}) \cdot x_b = 0.00441 \text{ N} \cdot \text{m}$. The values related to buoyancy were determined by considering ascending gliding of Flatfishbot.

Then, we resorted to the simulation software to obtain the values for C_l (lift coefficient) and C_d (drag coefficient) based on the three-dimensional real-body configuration of Flatfishbot as below as **Figure 65** and **Figure 66**.

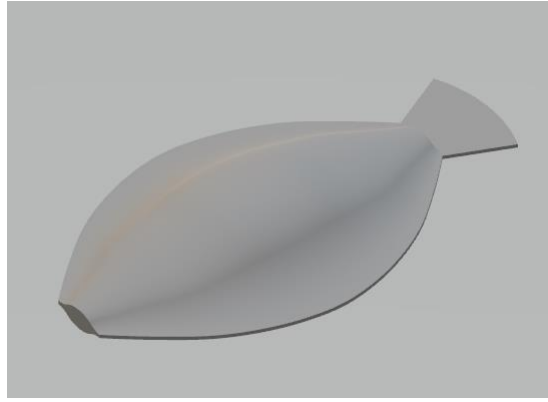


Figure 65 | Flatfishbot's 3D rendered image

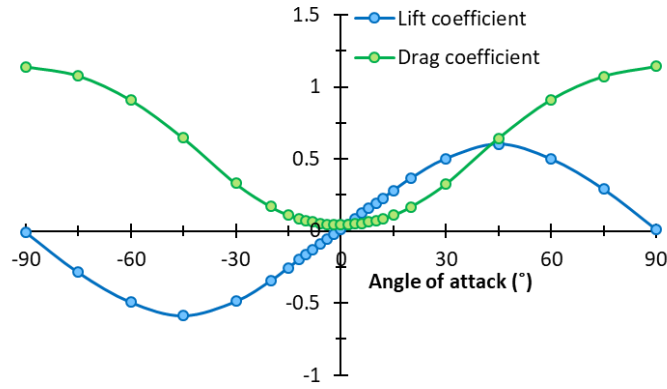


Figure 66 | Flatfishbot's calculated lift and drag coefficient depending on the angle of attack

Since the angle of attack (α) mainly affects C_l and C_d , we assumed C_l and C_d as functions of the angle of attack and came up with the estimated polynomial equations for C_l and C_d as below.

$$C_l \approx C_l(\alpha) = 0.0891\alpha^5 + 0.0037\alpha^4 - 0.6649\alpha^3 - 0.0133\alpha^2 + 1.1029\alpha + 0.014$$

$$C_d \approx C_d(\alpha) = 0.0611\alpha^6 - 0.0001\alpha^5 - 0.47\alpha^4 + 0.0017\alpha^3 + 1.235\alpha^2 - 0.0032\alpha + 0.0363$$

Lift and drag forces can be expressed in a derivative of x and y since it is a function of linear velocity as below.

$$L = \frac{1}{2}C_l\rho v^2A \approx L\left(\frac{dx}{dt}, \frac{dy}{dt}, \alpha\right)$$

$$D = \frac{1}{2}C_d\rho v^2A \approx L\left(\frac{dx}{dt}, \frac{dy}{dt}, \alpha\right)$$

$$\theta_v = \tan^{-1}\left(\frac{dx}{dt} / \frac{dy}{dt}\right)$$

We assumed that $\frac{dM}{dt} \approx 0$ since $\frac{d^2M}{dt^2}$ is considered small, and this allows us to rearrange the equation as below.

$$\begin{aligned} \frac{dM}{dt} = \frac{dL}{dt} \cdot x_l(\alpha) + L \cdot \frac{dx_l}{dt} + \frac{dD}{dt} \cdot y_d + D \cdot \frac{dy_d}{dt} \\ + B_{uSTPAM} \left(\frac{dx_b}{dt} \cos(\theta_v + \alpha) + x_b \frac{d\cos(\theta_v + \alpha)}{dt} \right) \approx 0 \end{aligned}$$

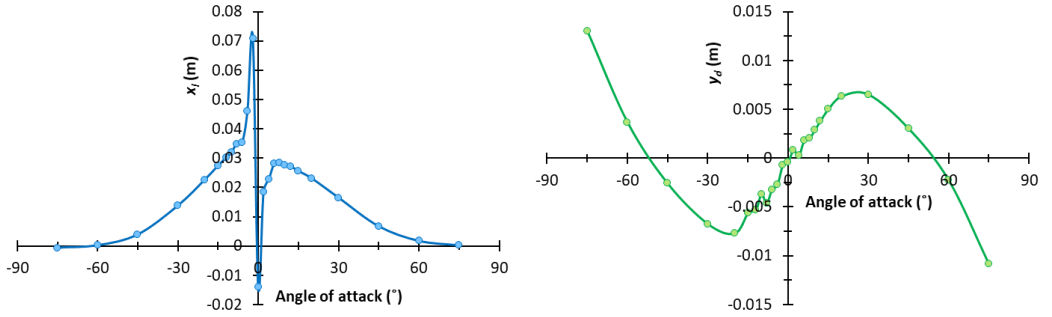


Figure 67 | Numerically calculated perpendicular distances of the lift force and the drag force

Like C_l and C_d , the x_l and y_d also can be derived from numerical simulation and assumed to functions of α as **Figure 67**.

$$\begin{aligned} x_l \approx x_l(\alpha) = (0.006146 \alpha^2 + 0.0001359 \alpha + 5.063 \\ \cdot 10^{-7}) / (\alpha^4 + 0.08358 \alpha^3 + 0.1773 \alpha^2 - 0.0001575 \alpha - 3.659 \\ \cdot 10^{-5}) \end{aligned}$$

$$\begin{aligned} y_d \approx y_d(\alpha) = 0.008389 \alpha^5 - 0.0004385 \alpha^4 - 0.03225 \alpha^3 + 0.001802 \alpha^2 \\ + 0.02165 \alpha - 0.0006979 \end{aligned}$$

So, $\frac{dM}{dt}$ can be expressed as a function of $\frac{dx}{dt}$, $\frac{dy}{dt}$, α , and $\frac{d\alpha}{dt}$. Therefore, rearranging $\frac{dM}{dt} = 0$, $\frac{d\alpha}{dt}$ can be expressed as below.

$$\frac{d\alpha}{dt} = f_1\left(\frac{dx}{dt}, \frac{dy}{dt}, \alpha\right)$$

Now, if we find out the ordinary differential equations for axial forces that are exerted on the robot fish, we can derive the following equations,

$$\frac{d^2x}{dt^2} = \frac{F_x}{m} = (-L \cdot \sin(\theta_v) - D \cdot \sin(\theta_v) + B_{body} + B_{TPA} - mg)/m$$

$$\frac{d^2y}{dt^2} = \frac{F_y}{m} = (L \cdot \cos(\theta_v) - D \cdot \sin(\theta_v) + B_{body} + B_{TPA} - mg)/m$$

Again, since L and D can be expressed as a derivative of x and y as well, we can obtain a couple more differential equations.

$$\frac{F_x}{m} = \frac{d^2x}{dt^2} = f_2\left(\frac{dx}{dt}, \frac{dy}{dt}, \alpha\right)$$

$$\frac{F_y}{m} = \frac{d^2y}{dt^2} = f_3\left(\frac{dx}{dt}, \frac{dy}{dt}, \alpha\right)$$

Let $y_1 = x$, $y_2 = y$, $y_3 = \frac{dx}{dt}$, $y_4 = \frac{dy}{dt}$, $y_5 = \alpha$, then we can substitute these values to the obtained equations and solve the differential equations by the fourth-order Runge Kutta Method.

$$\frac{dy_1}{dt} = y_3,$$

$$\frac{dy_2}{dt} = y_4,$$

$$\frac{dy_3}{dt} = \frac{d^2x}{dt^2} = f_2(y_3, y_4, y_5),$$

$$\frac{dy_4}{dt} = \frac{d^2y}{dt^2} = f_3(y_3, y_4, y_5),$$

$$\frac{dy_5}{dt} = f_1(y_3, y_4, y_5)$$

with the initial values of $y_1(0) = 0$, $y_2(0) = 0$, $y_3(0) = 0$, $y_4(0) = 0$, $y_5(0) = -\pi/6$ assuming a situation beginning to ascend. $y_5(0)$ was determined by considering the experimental value of the angle of attack when the Flatfishbot started to ascend.

Now, by solving the differential equations with MATLAB, we could obtain the theoretical physical values of the robotic fish locomotion during forward ascending that includes x-y 2D trajectory, posture angle, angular velocity, and angle of attack as depicted in **Figure 68**. We plotted the experimental result with the theoretical values for a clearer comparison.

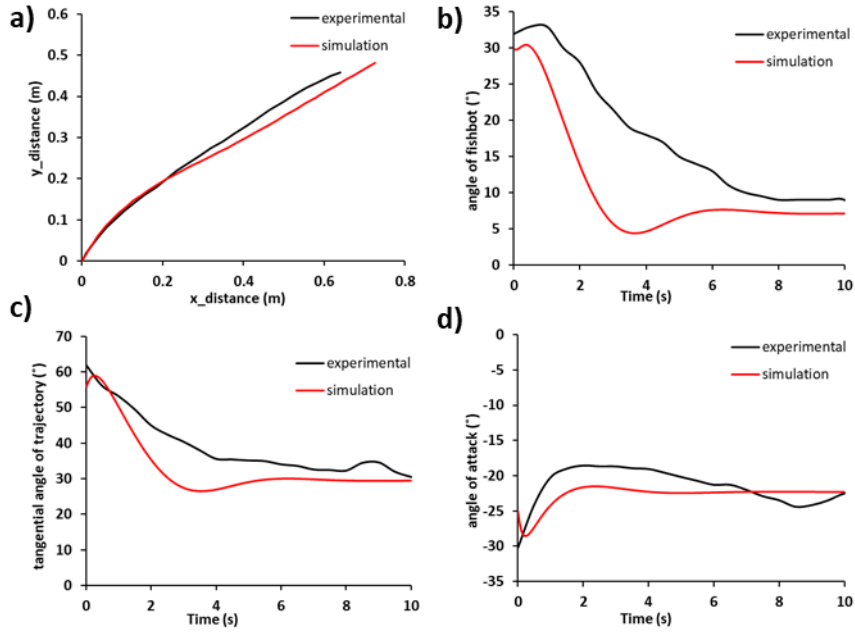


Figure 68 | Comparison between the experimental data and the simulated data of the ascending gliding locomotion of the Flatfishbot. a) x-y 2D trajectory b) posture angle c) angular velocity d) angle of attack

Despite the minor deviations between experiment and simulation outcomes in fish robot locomotion, we can observe the close resemblance of the two graphs in all four graphs in general. We believe that the most probable reason for the difference from the experimental result originates from theoretical C_D and C_L values that most likely changes according to the velocity. However, we computed C_D and C_L based on a constant velocity of $v = 0.04$ m/s, which cannot hold true in a real-life situation. Also, we presume that the limitation of the exact calculation of COD, COL, COG, COB, C_D , and C_L through the simulation is another reason for the difference. Moreover, the 3D robotic fish configuration we used to compute C_D and C_L does not consider inflatable uSTPAMs that reversibly change the volume.

3.4. Method

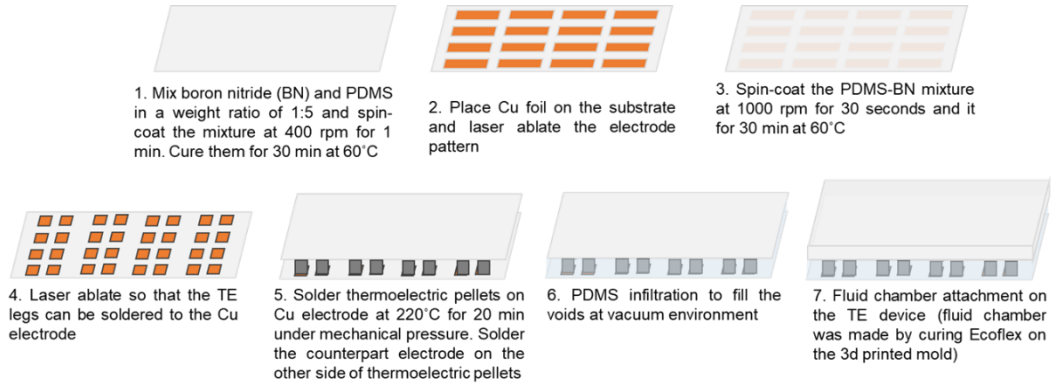


Figure 69 | Schematic representation of the device fabrication process. Note that thermoelectric pellets in the fabrication process as shown above are connected in series within the device and thus operate as a whole.

Material preparation: PDMS (Dow Corning), Ecoflex 00-30, Dragon Skin 10, Sil-poxy silicon adhesive and Silc Pig color dye (Smooth-On), Bi_2Te_3 thermoelectric legs (Wuhan XinRong New Materials Co., Ltd) 25- μm thick Cu foil (Alfa-Aesar). Boron nitride powder (Graphene Supermarket). All materials were used as received without purification. 0.25 μm Ni wire (Sigma Aldrich).

Thermoelectric pneumatic actuator fabrication: Boron nitride powder was incorporated into PDMS in a weight ratio of 1:5 to boost the thermal conductivity of the silicone elastomer, and the mixture was spin-coated at 350 r.p.m, followed by 60°C electric oven curing for 30 min. After curing, a copper foil was placed on the thermally conductive elastomer substrate and then laser-ablated (Nanio Air 355-3-V, Innolas, $\lambda = 355 \text{ nm}$) to form an interconnection electrode, on which the boron nitride/PDMS slurry mixture was successively spin-coated at 1000 rpm and cured at 60°C for 30 min to encapsulate the Cu electrode. Afterward, rectangular holes of thermally conductive elastomer were laser ablated without affecting Cu electrodes and then carefully peeled off to expose the Cu electrode for interconnection. The counterpart encapsulated Cu electrode was fabricated using the same process. Cream solder was screen-printed on the exposed Cu electrode so that alternating p-type and n-type thermoelectric Bi_2Te_3 legs can be mechanically soldered to the Cu electrode at 260°C for 15 min with mechanical pressure. Now, Bi_2Te_3 legs are soldered to the other counterpart Cu electrode so that the thermoelectric legs are connected in series. Then, the thermoelectric device was then placed in a petri-dish filled with slurry PDMS paste with the vacuum environment so that voids among thermoelectric legs are completely infiltrated with PDMS. Finally, the thermoelectric pneumatic actuator was

fabricated after the rectangular Ecoflex 00-30 chamber, which was cured on the 3d printed PLA mold, was attached to the top of the thermoelectric device. The graphical schematic of the fabrication process is provided in **Figure 69** for better understanding.

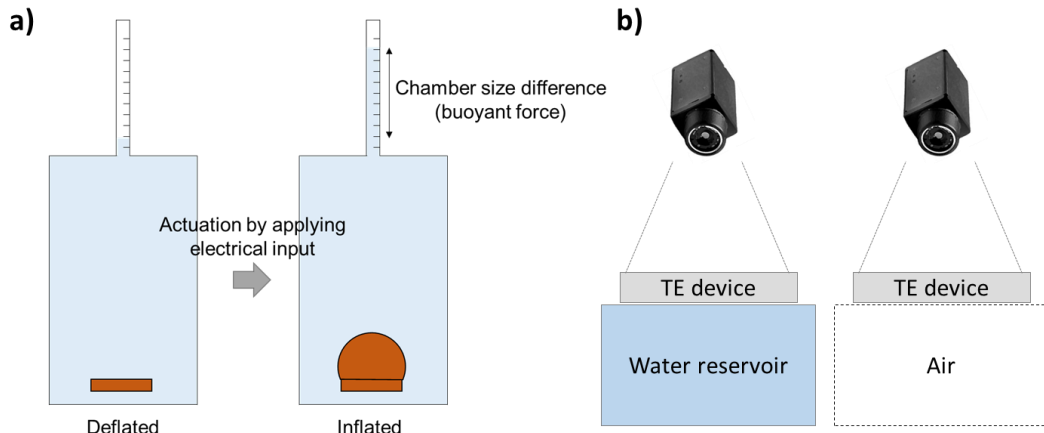


Figure 72 | Experimental setup to measure buoyant force and temperature. a) Inflation of uSTPAM causes the water level to rise, and the water level difference corresponds to the buoyant force. b) An experimental setup of active thermoelectric cooling in contact with water and suspended in the air.

Measurement of buoyant force: Buoyant force in this work was calculated by placing the uSTPAM unit inside water and then measuring the water level difference while applying electrical input to the uSTPAM unit as illustrated in **a**.

Comparison of TE device's performance in the variant environments: Comparing the heating performance between a thermoelectric device and Joule heater in **Figure 50** was by measuring the surface temperature (with the chamber removed) of two thermal devices with IR camera (FLIR A645) while their opposite sides were in contact with water to simulate the underwater environment (The Joule heater was made up of a commercial Ni-wire with 250 μm diameter in a multi-twisted form inside a thin film of PDMS block). Likewise, the thermoelectric cooling performance comparison operating between 1) underwater and 2) in the air was conducted by measuring the surface temperature with the IR camera while the opposite side of the device was either in contact with water or air as illustrated in **Figure 72b**.

Numerical simulation: COMSOL simulation was used to calculate the L/D and angle of attack first to determine the shape and further optimize the design of the robotic after the shape had been decided with the assumption that water flows at the subject at the constant velocity of $0.2 \text{ m}\cdot\text{s}^{-1}$.

Also, C_l , C_d , x_l , and y_d was calculated by COMSOL simulation.

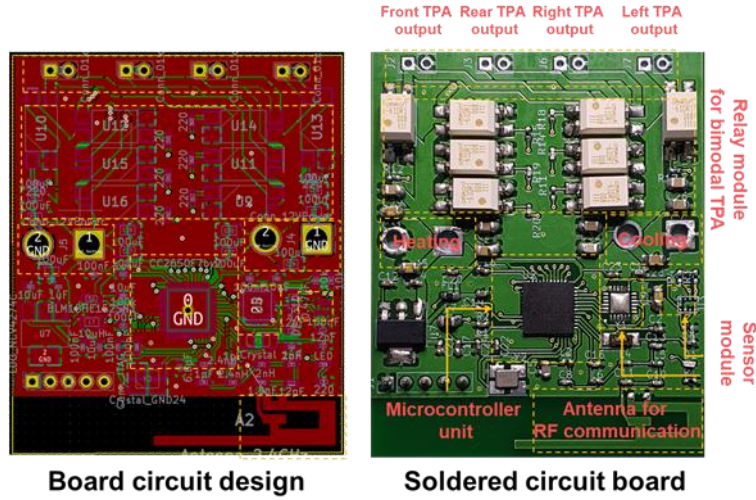


Figure 73 | Board circuit design and the corresponding soldered printed circuit board that consists of functional components for locomotion performance. We used two separate battery modules for constant heating and cooling modes: 7.4 V 2500 mAh LiPo battery for the heating mode (and powering microcontroller via the 3.3 V regulator) and a couple of 1.2 V 2000 mAh NiMH batteries connected in series for the cooling mode.

The wireless control circuit design: About the TPA circuit design, a single 7.4 V battery and two 2.4 V batteries were used to power four units of TPAs and microprocessors. Since TPAs in this study must interchangeably alternate between thermoelectric heating and cooling mode, the single-pole, single-throw (SPST) relays were used to switch between two thermal modes. The 7.4 V battery was responsible for relaying the heating mode and powering the microprocessor at 3.3 V using a regulator. Two 2.4 V batteries connected in series were employed to relay the cooling mode of the device. The RF wireless communication was employed because a longer wavelength ensures communication for a longer distance. All these components were integrated in the PCB board circuit depicted in **Figure 73**.

Chapter 4. Conclusion

In this study, we presented an active cooling method for a phase transition-based soft thermal pneumatic actuator to improve deflation speed. To facilitate active cooling, a soft TE device was employed as the thermal management device. Copper fins and thermally conductive silicone rubber were attached to allow moderate heat exchange between the engineered fluid and the soft TE device. Furthermore, the soft PCM heatsink was applied to the STPAM to dissipate heat while maintaining a soft interface and low temperature. The active cooling function successfully improved both the deflation rate of the single STPAM and the recovery rate of the diverse STPAM assembly actuators. This study exploring these cooling strategies would contribute to the advancement of phase transition-based soft applications that alter rigid peripherals supplying pneumatic sources. Moreover, modular designs of STPAMs, assembled to demonstrate different motions, including bending and rectilinear stretching, imply that STPAMs can be customized in several ways to achieve suitable motion to serve their purposes. Lastly, a soft gripper and untethered autonomous soft robot were demonstrated to validate the practicality of the STPAM. The demonstration of the autonomous untethered robot carrying its power source by itself was made possible through the development of the strong low-voltage-driven STPAM. Furthermore, this paper reports an untethered soft robotic fish that can mimic effective gliding locomotions inspired by marine vertebrates saving aerobic energy based on selective manipulation of localized buoyancy. The bi-modal uSTPAMs reversibly change the fluid phase with a rapid response time to control localized buoyancy, facilitating the robot's gliding locomotion. The integrated wireless module allows bi-directional communication with an operator while receiving real-time physical information from the pressure and gyro-sensors. With an integrated soft structure, the robot could simulate the sinusoidal locomotion of the marine vertebrates and make steer turns. As a result, the Flatfishbot moves faster than most previous fish robots, even without thrust force generation, showing the energy efficiency of the intermittent gliding mechanism. Finally, this work demonstrates the robot's practical usage as a cargo-submarine or underwater inspector to examine the aquatic environment. Especially, since the gliding locomotion is controlled by posture induced by localized buoyancy, it has the advantage that it can be used simultaneously with other propulsion methods of previously studied robotic fishes oscillating and undulating the body and fins.

Besides, the slow response of the phase-transition-based thermo-pneumatic soft actuator still remains to be improved, despite the improvement due to the thermoelectric cooling function, because it employed a much slower operating mechanism (phase-transition) than other types of soft actuators. Approaching an application that is not affected by these shortcomings would be a good solution. Also, the applications presented in this paper may not demand TE device's flexibility and stretchability. However, presented design of TE devices easily can be modified into a flexible form by changing the electrode

design to serpentine pattern. Therefore, this work would contribute not only soft robotics but also next generation electronics widely including wearable electronics.

Meanwhile, the study remains some future works supporting completeness, enhancing performance, and expanding applications. The STPAM employed several components including copper fins, PCM heatsink, and thermal enhancing filler to improve thermal properties and showed its feasibility, but these auxiliary components have not been deeply explored. We only show that employing copper fins assists in better heat transfer, but study insufficiently on how to maximize the assistance of copper fins. A geometry of copper fin and condensation mode regarding the cooling power and surface morphology, and so on can be further studied to improve the inflating efficiency of the STPAM. Moreover, numerous studies related to PCM heatsinks, such as maximizing the latent heat capacity and implementing flexibility and stretchability, have been presented recently. These state-of-the-art PCM heatsink technology can be applied to STPAM. Also, several studies are enhancing the electronics including thermo-electric devices by improving their substrates' thermal conductivity with thermal enhancers such as BN. They aligned thermally conductive fillers and controlled geometry, in addition to simply mixing fillers, to improve thermal conductivity of the substrates. We believe that the thermally conductive substrate of STPAM can be improved with these strategies. Furthermore, the chamber materials should also be improved. The chamber of STPAM is composed of silicone elastomers such as PDMS and eco-flex that is hard to block the gas permeation. The gas permeation induces the loss of the working fluid and hinder the deflation of STPAM through the unintended evaporation of the captured gas in the silicone rubber. STPAM may employ low-gas permeable rubber like SEBS or restrain the gas permeability of the silicone rubber by mixing some additives such as paraffin to prevent the loss of gas and advance its deflation performance. We hope the presented STPAM and its components would be one step closer to be practically applied in related fields including soft robotics and next generation electronics through above works.

Bibliography

1. Fang, G.; Chow Marco, C. K.; Ho Justin, D. L.; He, Z.; Wang, K.; Ng, T. C.; Tsoi James, K. H.; Chan, P.-L.; Chang, H.-C.; Chan Danny, T.-M.; Liu, Y.-h.; Holsinger, F. C.; Chan Jason, Y.-K.; Kwok, K.-W., Soft robotic manipulator for intraoperative MRI-guided transoral laser microsurgery. *Science Robotics* **2021**, *6* (57), eabg5575.
2. Wang, Y.; Xu, Q., Design and testing of a soft parallel robot based on pneumatic artificial muscles for wrist rehabilitation. *Scientific Reports* **2021**, *11* (1), 1273.
3. Chu, C.-Y.; Patterson, R. M., Soft robotic devices for hand rehabilitation and assistance: a narrative review. *Journal of NeuroEngineering and Rehabilitation* **2018**, *15* (1), 9.
4. Peng, Z.; Huang, J., Soft Rehabilitation and Nursing-Care Robots: A Review and Future Outlook. *Applied Sciences* **2019**, *9* (15).
5. Jiang, Y.; Chen, D.; Que, J.; Liu, Z.; Wang, Z.; Xu, Y. In *Soft robotic glove for hand rehabilitation based on a novel fabrication method*, 2017 IEEE International Conference on Robotics and Biomimetics (ROBIO), 5-8 Dec. 2017; 2017; pp 817-822.
6. Navas, E.; Fernández, R.; Sepúlveda, D.; Armada, M.; Gonzalez-de-Santos, P., Soft Grippers for Automatic Crop Harvesting: A Review. *Sensors (Basel)* **2021**, *21* (8), 2689.
7. Wang, Z.; Hirai, S. In *Chamber dimension optimization of a bellow-type soft actuator for food material handling*, 2018 IEEE International Conference on Soft Robotics (RoboSoft), 24-28 April 2018; 2018; pp 382-387.
8. Li, G.; Chen, X.; Zhou, F.; Liang, Y.; Xiao, Y.; Cao, X.; Zhang, Z.; Zhang, M.; Wu, B.; Yin, S.; Xu, Y.; Fan, H.; Chen, Z.; Song, W.; Yang, W.; Pan, B.; Hou, J.; Zou, W.; He, S.; Yang, X.; Mao, G.; Jia, Z.; Zhou, H.; Li, T.; Qu, S.; Xu, Z.; Huang, Z.; Luo, Y.; Xie, T.; Gu, J.; Zhu, S.; Yang, W., Self-powered soft robot in the Mariana Trench. *Nature* **2021**, *591* (7848), 66-71.
9. Katzschmann Robert, K.; DelPreto, J.; MacCurdy, R.; Rus, D., Exploration of underwater life with an acoustically controlled soft robotic fish. *Science Robotics* **2018**, *3* (16), eaar3449.
10. Ng, C. S. X.; Tan, M. W. M.; Xu, C.; Yang, Z.; Lee, P. S.; Lum, G. Z., Locomotion of Miniature Soft Robots. *Advanced Materials* **2021**, *33* (19), 2003558.
11. Cacucciolo, V.; Shintake, J.; Kuwajima, Y.; Maeda, S.; Floreano, D.; Shea, H., Stretchable pumps for soft machines. *Nature* **2019**, *572* (7770), 516-519.
12. An, S.; Kang, D. J.; Yarin, A. L., A blister-like soft nano-textured thermo-pneumatic actuator as an artificial muscle. *Nanoscale* **2018**, *10* (35), 16591-16600.
13. Kang, D. J.; An, S.; Yarin, A. L.; Anand, S., Programmable soft robotics based on nano-textured thermo-responsive actuators. *Nanoscale* **2019**, *11* (4), 2065-2070.
14. Chellattoan, R.; Yudhanto, A.; Lubineau, G., Low-Voltage-Driven Large-Amplitude Soft Actuators Based on Phase Transition. *Soft Robot* **2020**, *7* (6), 688-699.
15. Miriyev, A.; Stack, K.; Lipson, H., Soft material for soft actuators. *Nat Commun* **2017**, *8* (1), 596.
16. Nakahara, K.; Narumi, K.; Niiyama, R.; Kawahara, Y. In *Electric phase-*

change actuator with inkjet printed flexible circuit for printable and integrated robot prototyping, 2017 IEEE International Conference on Robotics and Automation (ICRA), 29 May–3 June 2017; 2017; pp 1856–1863.

17. Meder, F.; Naselli, G. A.; Sadeghi, A.; Mazzolai, B., Remotely Light-Powered Soft Fluidic Actuators Based on Plasmonic-Driven Phase Transitions in Elastic Constraint. *Adv Mater* **2019**, *31* (51), e1905671.

18. Mirvakili Seyed, M.; Sim, D.; Hunter Ian, W.; Langer, R., Actuation of untethered pneumatic artificial muscles and soft robots using magnetically induced liquid-to-gas phase transitions. *Science Robotics* **2020**, *5* (41), eaaz4239.

19. Mishra Anand, K.; Wallin Thomas, J.; Pan, W.; Xu, P.; Wang, K.; Giannelis Emmanuel, P.; Mazzolai, B.; Shepherd Robert, F., Autonomic perspiration in 3D-printed hydrogel actuators. *Science Robotics* **2020**, *5* (38), eaaz3918.

20. Thermoelectric Technical Reference.
<https://thermal.ferrotec.com/technology/thermoelectric-reference-guide/thermalref10/> (accessed 2021-11-21).

21. Nozariasbmarz, A.; Collins, H.; Dsouza, K.; Polash, M. H.; Hosseini, M.; Hyland, M.; Liu, J.; Malhotra, A.; Ortiz, F. M.; Mohaddes, F.; Ramesh, V. P.; Sargolzaeiaval, Y.; Snouwaert, N.; Öztürk, M. C.; Vashae, D., Review of wearable thermoelectric energy harvesting: From body temperature to electronic systems. *Applied Energy* **2020**, *258*, 114069.

22. Izzard, V.; Record, M. C.; Tedenac, J. C., Mechanical alloying of a new promising thermoelectric material, Sb₃Zn₄. *Journal of Alloys and Compounds* **2002**, *345* (1), 257–264.

23. Castro-Gomez, R. C.; Hall, K. R.; Holste, J. C.; Gammon, B. E.; Marsh, K. N., A thermoelectric flow enthalpy-increment calorimeter. *The Journal of Chemical Thermodynamics* **1990**, *22* (3), 269–278.

24. Zhao, D.; Tan, G., A review of thermoelectric cooling: Materials, modeling and applications. *Applied Thermal Engineering* **2014**, *66* (1), 15–24.

25. Lyu, Y.; Siddique, A. R. M.; Majid, S. H.; Biglarbegian, M.; Gadsden, S. A.; Mahmud, S., Electric vehicle battery thermal management system with thermoelectric cooling. *Energy Reports* **2019**, *5*, 822–827.

26. Li, J.; Ma, B.; Wang, R.; Han, L., Study on a cooling system based on thermoelectric cooler for thermal management of high-power LEDs. *Microelectronics Reliability* **2011**, *51* (12), 2210–2215.

27. Lee, D.; Park, H.; Park, G.; Kim, J.; Kim, H.; Cho, H.; Han, S.; Kim, W., Liquid-metal-electrode-based compact, flexible, and high-power thermoelectric device. *Energy* **2019**, *188*, 116019.

28. Jung, K. K.; Jung, Y.; Choi, C. J.; Lee, J. M.; Ko, J. S., Flexible thermoelectric generator with polydimethyl siloxane in thermoelectric material and substrate. *Current Applied Physics* **2016**, *16* (10), 1442–1448.

29. Lee, B.; Cho, H.; Park, K. T.; Kim, J.-S.; Park, M.; Kim, H.; Hong, Y.; Chung, S., High-performance compliant thermoelectric generators with magnetically self-assembled soft heat conductors for self-powered wearable electronics. *Nature Communications* **2020**, *11* (1), 5948.

30. Lee, J.; Sul, H.; Jung, Y.; Kim, H.; Han, S.; Choi, J.; Shin, J.; Kim, D.; Jung, J.; Hong, S.; Ko, S. H., Thermally Controlled, Active Imperceptible Artificial Skin in Visible-to-Infrared Range. *Advanced Functional Materials* **2020**, *30*

(36).

31. Lee, J.; Sul, H.; Lee, W.; Pyun, K. R.; Ha, I.; Kim, D.; Park, H.; Eom, H.; Yoon, Y.; Jung, J.; Lee, D.; Ko, S. H., Stretchable Skin-Like Cooling/Heating Device for Reconstruction of Artificial Thermal Sensation in Virtual Reality. *Advanced Functional Materials* **2020**, *30* (29).
32. Kim, S.-W.; Kim, S. H.; Kim, C. S.; Yi, K.; Kim, J.-S.; Cho, B. J.; Cha, Y., Thermal display glove for interacting with virtual reality. *Scientific Reports* **2020**, *10* (1), 11403.
33. Yuan, C.; Li, J.; Lindsay, L.; Cherns, D.; Pomeroy, J. W.; Liu, S.; Edgar, J. H.; Kuball, M., Modulating the thermal conductivity in hexagonal boron nitride via controlled boron isotope concentration. *Communications Physics* **2019**, *2* (1), 43.
34. Li, G.; Chen, X.; Zhou, F.; Liang, Y.; Xiao, Y.; Cao, X.; Zhang, Z.; Zhang, M.; Wu, B.; Yin, S., Self-powered soft robot in the Mariana Trench. *Nature* **2021**, *591* (7848), 66–71.
35. Huang, X.; Kumar, K.; Jawed, M. K.; Mohammadi Nasab, A.; Ye, Z.; Shan, W.; Majidi, C., Highly Dynamic Shape Memory Alloy Actuator for Fast Moving Soft Robots. *Advanced Materials Technologies* **2019**, *4* (4), 1800540.
36. Li, H.; Yao, J.; Wei, C.; Zhou, P.; Xu, Y.; Zhao, Y., An untethered soft robotic gripper with high payload-to-weight ratio. *Mechanism and Machine Theory* **2021**, *158*, 104226.
37. Li, Y.; Chen, Y.; Ren, T.; Li, Y.; Choi, S. h., Precharged Pneumatic Soft Actuators and Their Applications to Untethered Soft Robots. *Soft Robotics* **2018**, *5* (5), 567–575.
38. Tan, Q.; Chen, Y.; Liu, J.; Zou, K.; Yi, J.; Liu, S.; Wang, Z., Underwater Crawling Robot With Hydraulic Soft Actuators. *Frontiers in Robotics and AI* **2021**, *8*.
39. Usevitch Nathan, S.; Hammond Zachary, M.; Schwager, M.; Okamura Allison, M.; Hawkes Elliot, W.; Follmer, S., An untethered isoperimetric soft robot. *Science Robotics* **2020**, *5* (40), eaaz0492.
40. Gleiss, A. C.; Jorgensen, S. J.; Liebsch, N.; Sala, J. E.; Norman, B.; Hays, G. C.; Quintana, F.; Grundy, E.; Campagna, C.; Trites, A. W., Convergent evolution in locomotory patterns of flying and swimming animals. *Nature communications* **2011**, *2* (1), 1–7.
41. Sato, K.; Mitani, Y.; Cameron, M. F.; Siniff, D. B.; Naito, Y., Factors affecting stroking patterns and body angle in diving Weddell seals under natural conditions. *Journal of experimental Biology* **2003**, *206* (9), 1461–1470.
42. Williams, T. M.; Davis, R.; Fuiman, L.; Francis, J.; Le, B.; Boeuf; Horning, M.; Calambokidis, J.; Croll, D., Sink or swim: strategies for cost-efficient diving by marine mammals. *Science* **2000**, *288* (5463), 133–136.
43. Chu, W.-S.; Lee, K.-T.; Song, S.-H.; Han, M.-W.; Lee, J.-Y.; Kim, H.-S.; Kim, M.-S.; Park, Y.-J.; Cho, K.-J.; Ahn, S.-H., Review of biomimetic underwater robots using smart actuators. *International Journal of Precision Engineering and Manufacturing* **2012**, *13* (7), 1281–1292.
44. Li, T.; Li, G.; Liang, Y.; Cheng, T.; Dai, J.; Yang, X.; Liu, B.; Zeng, Z.; Huang, Z.; Luo, Y., Fast-moving soft electronic fish. *Science advances* **2017**, *3* (4), e1602045.
45. Aubin, C. A.; Choudhury, S.; Jerch, R.; Archer, L. A.; Pikul, J. H.;

- Shepherd, R. F., Electrolytic vascular systems for energy-dense robots. *Nature* **2019**, *571* (7763), 51–57.
46. Katzschmann, R. K.; DelPreto, J.; MacCurdy, R.; Rus, D., Exploration of underwater life with an acoustically controlled soft robotic fish. *Science Robotics* **2018**, *3* (16), eaar3449.
 47. Shintake, J.; Cacucciolo, V.; Shea, H.; Floreano, D., Soft biomimetic fish robot made of dielectric elastomer actuators. *Soft robotics* **2018**, *5* (4), 466–474.
 48. Zhu, J.; White, C.; Wainwright, D. K.; Di Santo, V.; Lauder, G. V.; Bart-Smith, H., Tuna robotics: A high-frequency experimental platform exploring the performance space of swimming fishes. *Science Robotics* **2019**, *4* (34), eaax4615.
 49. Kim, H.-S.; Lee, J.-Y.; Chu, W.-S.; Ahn, S.-H., Design and fabrication of soft morphing ray propulsor: undulator and oscillator. *Soft robotics* **2017**, *4* (1), 49–60.
 50. Shintake, J.; Zappetti, D.; Peter, T.; Ikemoto, Y.; Floreano, D. In *Bio-inspired tensegrity fish robot*, 2020 IEEE International Conference on Robotics and Automation (ICRA), IEEE: 2020; pp 2887–2892.
 51. Park, S.-J.; Gazzola, M.; Park, K. S.; Park, S.; Di Santo, V.; Blevins, E. L.; Lind, J. U.; Campbell, P. H.; Dauth, S.; Capulli, A. K., Phototactic guidance of a tissue-engineered soft-robotic ray. *Science* **2016**, *353* (6295), 158–162.
 52. Marchese, A. D.; Onal, C. D.; Rus, D., Autonomous soft robotic fish capable of escape maneuvers using fluidic elastomer actuators. *Soft robotics* **2014**, *1* (1), 75–87.
 53. Nguyen, T. T.; Lee, B. R.; Vo, T. Q., Dynamic analysis of a robotic fish propelled by flexible folding pectoral fins. *Robotica* **2020**, *38* (4), 699–718.
 54. Smits, A. J., Undulatory and oscillatory swimming. *Journal of Fluid Mechanics* **2019**, *874*.
 55. Chen, B.; Jiang, H., Swimming performance of a tensegrity robotic fish. *Soft robotics* **2019**, *6* (4), 520–531.
 56. Coral, W.; Rossi, C.; Curet, O. M.; Castro, D., Design and assessment of a flexible fish robot actuated by shape memory alloys. *Bioinspiration & biomimetics* **2018**, *13* (5), 056009.
 57. Aureli, M.; Kopman, V.; Porfiri, M., Free-locomotion of underwater vehicles actuated by ionic polymer metal composites. *IEEE/ASME transactions on mechatronics* **2009**, *15* (4), 603–614.
 58. Phamduy, P.; Vazquez, M. A.; Kim, C.; Mwaffo, V.; Rizzo, A.; Porfiri, M., Design and characterization of a miniature free-swimming robotic fish based on multi-material 3D printing. *International Journal of Intelligent Robotics and Applications* **2017**, *1* (2), 209–223.
 59. Kopman, V.; Laut, J.; Acquaviva, F.; Rizzo, A.; Porfiri, M., Dynamic modeling of a robotic fish propelled by a compliant tail. *IEEE Journal of Oceanic Engineering* **2014**, *40* (1), 209–221.
 60. Kopman, V.; Porfiri, M., Design, modeling, and characterization of a miniature robotic fish for research and education in biomimetics and bioinspiration. *IEEE/ASME Transactions on mechatronics* **2012**, *18* (2), 471–483.
 61. Zhou, C.; Low, K., Design and locomotion control of a biomimetic underwater vehicle with fin propulsion. *IEEE/ASME Transactions on Mechatronics* **2011**, *17* (1), 25–35.

62. Zhang, Z. G.; Yamashita, N.; Gondo, M.; Yamamoto, A.; Higuchi, T., Electrostatically actuated robotic fish: Design and control for high-mobility open-loop swimming. *IEEE transactions on Robotics* **2008**, *24* (1), 118–129.
63. Wang, Z.; Hang, G.; Wang, Y.; Li, J.; Du, W., Embedded SMA wire actuated biomimetic fin: a module for biomimetic underwater propulsion. *Smart Materials and Structures* **2008**, *17* (2), 025039.
64. Christianson, C.; Goldberg, N. N.; Deheyn, D. D.; Cai, S.; Tolley, M. T., Translucent soft robots driven by frameless fluid electrode dielectric elastomer actuators. *Science Robotics* **2018**, *3* (17), eaat1893.
65. Kohl, A. M.; Kelasidi, E.; Mohammadi, A.; Maggiore, M.; Pettersen, K. Y., Planar maneuvering control of underwater snake robots using virtual holonomic constraints. *Bioinspiration & biomimetics* **2016**, *11* (6), 065005.
66. Christianson, C.; Bayag, C.; Li, G.; Jadhav, S.; Giri, A.; Agba, C.; Li, T.; Tolley, M. T., Jellyfish-inspired soft robot driven by fluid electrode dielectric organic robotic actuators. *Frontiers in Robotics and AI* **2019**, 126.
67. Robertson, M. A.; Efremov, F.; Paik, J., RoboScallop: a bivalve inspired swimming robot. *IEEE Robotics and Automation Letters* **2019**, *4* (2), 2078–2085.
68. Cianchetti, M.; Calisti, M.; Margheri, L.; Kuba, M.; Laschi, C., Bioinspired locomotion and grasping in water: the soft eight-arm OCTOPUS robot. *Bioinspiration & biomimetics* **2015**, *10* (3), 035003.
69. Song, S.-H.; Kim, M.-S.; Rodrigue, H.; Lee, J.-Y.; Shim, J.-E.; Kim, M.-C.; Chu, W.-S.; Ahn, S.-H., Turtle mimetic soft robot with two swimming gaits. *Bioinspiration & biomimetics* **2016**, *11* (3), 036010.
70. Jin, H.; Dong, E.; Alici, G.; Mao, S.; Min, X.; Liu, C.; Low, K.; Yang, J., A starfish robot based on soft and smart modular structure (SMS) actuated by SMA wires. *Bioinspiration & biomimetics* **2016**, *11* (5), 056012.
71. Wang, S.; Huang, B.; McCoul, D.; Li, M.; Mu, L.; Zhao, J., A soft breaststroke-inspired swimming robot actuated by dielectric elastomers. *Smart Materials and Structures* **2019**, *28* (4), 045006.
72. Fänge, R., Gas exchange in fish swim bladder. *Reviews of Physiology, Biochemistry and Pharmacology, Volume 97* **1983**, 111–158.
73. Shibuya, K.; Kishimoto, Y.; Yoshii, S., Depth Control of Underwater Robot with Metal Bellows Mechanism for Buoyancy Control Device Utilizing Phase Transition. *J. Robotics Mechatronics* **2013**, *25* (5), 795–803.
74. Han, J.; Jiang, W.; Zhang, H.; Lei, B.; Wang, L.; Liu, H., Submersible Soft-Robotic Platform for Noise-Free Hovering Utilizing Liquid-Vapor Phase Transition. *Advanced Intelligent Systems* **2021**, *3* (1), 2000147.
75. Lee, J.; Sul, H.; Lee, W.; Pyun, K. R.; Ha, I.; Kim, D.; Park, H.; Eom, H.; Yoon, Y.; Jung, J., Stretchable skin-like cooling/heating device for reconstruction of artificial thermal sensation in virtual reality. *Advanced Functional Materials* **2020**, *30* (29), 1909171.
76. Miriyev, A.; Stack, K.; Lipson, H., Soft material for soft actuators. *Nature communications* **2017**, *8* (1), 1–8.
77. Buckner, T. L.; Yuen, M. C.; Kim, S. Y.; Kramer-Bottiglio, R., Enhanced Variable Stiffness and Variable Stretchability Enabled by Phase-Changing Particulate Additives. *Advanced Functional Materials* **2019**, *29* (50), 1903368.
78. Zhou, Z.; Li, Q.; Chen, L.; Liu, C.; Fan, S., A large-deformation phase transition electrothermal actuator based on carbon nanotube-elastomer composites.

Journal of Materials Chemistry B **2016**, 4 (7), 1228–1234.

79. Mayer, P.; Ram, R., Optimization of heat sink–limited thermoelectric generators. *Nanoscale and Microscale Thermophysical Engineering* **2006**, 10 (2), 143–155.

80. Qureshi, U. M.; Shaikh, F. K.; Aziz, Z.; Shah, S. M. Z. S.; Sheikh, A. A.; Felemban, E.; Qaisar, S. B., RF path and absorption loss estimation for underwater wireless sensor networks in different water environments. *Sensors* **2016**, 16 (6), 890.

81. Huang, J.-g.; Wang, H.; He, C.-b.; Zhang, Q.-f.; Jing, L.-y., Underwater acoustic communication and the general performance evaluation criteria. *Frontiers of Information Technology & Electronic Engineering* **2018**, 19 (8), 951–971.

Abstract

소프트 공압 액츄에이터는 소프트 로봇 공학의 기술 발전에서 중요한 역할을 하지만 공기 압축기 및 튜브와 같이 복잡하고 부피가 큰 주변 장치의 존재로 인해 전체적으로 완전히 부드러운 소프트 로봇 시스템에 적용하기 어렵다. 따라서 소프트 로봇의 작동 및 적절한 설계를 방해하는 복잡한 주변 장치 없이, 혹은 이를 부드러운 재질로 만들어 소프트 로봇 제어 시스템을 단순화 할 필요가 있다. 이에, 이 연구에서는 소프트 열전 소자를 사용하여 열적으로 제어되는 기체-액체 간 상변화 현상을 기반으로 작동하는 소프트 열 공압 구동 모듈(STPAM)을 개발했다. 열전 소자의 양방향 열 제어 기능을 통해 공압챔버의 팽창 및 수축을 제어할 수 있었고, 이를 더욱이 원활하게 하기 위해 기판 소재인 실리콘 고무의 열 전도도를 향상시키는 연구 또한 진행되었다. 또한 열전 소자의 열 역류를 방지하기 위해 액체-고체 간 상변화 현상을 이용한 상변화물질 기반 히트싱크를 개발하였다. 이를 통해 열전소자의 능동 냉각기능이 안정적으로 구현될 수 있었고, 이는 구동기의 전체 구동 시간중 큰 비중을 차지하는 냉각 수축 과정을 단축하는데 기여하였다. STPAM을 다양한 형태로 조립하여 굽힘, 선형 신축 운동 등 다양한 형태의 움직임을 구현하였고, 이를 기반으로 소프트 그리퍼 및 무선 소프트 로봇을 개발하였다. 나아가, STPAM을 부력제어모듈로 활용하여 수중동물들의 활공을 모사한 Flatfishbot 또한 개발했다. Flatfishbot은 부력 제어를 통해 자세를 조절하고 이를 통해 활공과 회전하는 움직임을 구현하였다. 또한 카메라를 통해 수중 환경을 탐사하거나 화물을 나르는 작업 또한 성공적으로 수행하였다.